THESIS

MICHIGAN STATE UNIVERSITY LIBRARIES
3 1293 00908 1914

This is to certify that the

dissertation entitled
Topological Rigidity and Structural
study of Disordered System

presented by

Yong Cai

has been accepted towards fulfillment
of the requirements for
Ph. D. degree in Physics

M. F. Thorpe
Major professor

Date 25 July 1991

MSU is an Affirmative Action/Equal Opportunity Institution

O-12771

LIBRARY
Michigan State
University

PLACE IN RETURN BOX to remove this checkout from your record.
TO AVOID FINES return on or before date due.

DATE DUE	DATE DUE	DATE DUE

MSU Is An Affirmative Action/Equal Opportunity Institution
c:\circ\datedue.pm3-p.1

TOPOLOGICAL RIGIDITY AND STRUCTURAL STUDY OF DISORDERED SYSTEM

By

Yong Cai

A DISSERTATION

Submitted to

Michigan State University

in partial fulfillment of the requirements

for the degree of

DOCTOR OF PHILOSOPHY

Department of Physics and Astronomy

1991

654-6006

ABSTRACT

TOPOLOGICAL RIGIDITY AND STRUCTURAL STUDY OF DISORDERED SYSTEM

By

Yong Cai

In this thesis we have studied the elastic and structural properties of disordered systems. Our research provides a good understanding of the size mismatch problem frequently encountered in intercalated multilayer systems and semiconductor alloys. By studying the short range and long range properties of these disordered systems in various dimensions, it is possible to draw a clear physical picture by introducing a set of topological rigidity parameters which can be understood from an effective medium point of view.

The observation of soft phonon and elastic properties of network glasses can be understood in term of the rigidity percolation concept. This study adds a new example to the application of rigidity percolation theory. It also provides an explanation for the soft phonon modes observed in covalent glasses.

The size mismatch problem is interesting because of its wide ranging application to semiconducting materials. Using analytic solutions of the simple model and the effective medium treatment of realistic models, we studied the intercalated graphite multilayer systems, $2d$ triangular lattice, $3d$ FCC lattice and $3d$ diamond lattice. Our theoretical results suggest simple structural expressions for average nearest neighbor distances and corresponding distributions in term of dimensionless topological parameters. From the point of view of composition, we studied binary, ternary and

quaternary system. Indeed, it is a theoretical success that we have been able to obtain the analytic solutions for quaternary system which contains all compounds we studied before as special cases. This leads to a general formalism for the length mismatch problem in semiconducting alloy systems.

The investigation of the long range properties of $3d$ disordered systems leads to the concept of "effective temperature for disorder". Huang scattering is studied and we have a better understanding of the effect of static disorder on diffraction patterns.

The mismatch problem in $2d$ is especially interesting because this($2d$) happens to be a marginal dimension. We observed various instabilities in computer simulations. The most interesting one is the "static melting", which is a zero temperature equivalence of thermal melting but driven by disorder. Research in this direction is still in progress.

ACKNOWLEDGEMENTS

With great respect and deep gratitude I acknowledge my adviser, Professor M. F. Thorpe, for his professional guidance and endless encouragement in this work. His scientific research attitude, his physical insight of complicated phenomena, and his constant searching for simple truth has been and will always be the greatest inspiration to me. I thank him for his understanding, supporting and patient advising during the last four years.

I am grateful to Professor S. D. Mahanti, Professor W. Bauer, Professor N. Birge and Professor M. Dubson for their service on my Ph. D. guidance committee, and I would like to express my special thanks to Professor J. Kovacs for his patient assistance and Mrs. Janet King for her help.

I would like to thank Professor S. D. Mahanti, Professor P. Duxbury, Professor D. Tomanek, Professor W. Bauer, and Professor T. Kaplan for their valuable lectures, advice and many helpful conversations. Their help and influence on my graduate study are greatly appreciated.

My thanks also go to my family for their support and encouragement, and my dear friends: W. Q. Zhong, J. D. Chen, N. J. Jiu, N. Mousseau, B. Pi, X. H. Yu, Y. Wang, Q. F. Zhu and others in this department for their many interesting discussions during my studying in MSU and help in preparation of the thesis. I acknowledge Dr. Y. S. Li and Dr. G. Overney for their valuable friendship.

Financial support from Michigan State University, the National Science Foundation and the Center for Fundamental Material Research are gratefully acknowledged.

Contents

1 INTRODUCTION **1**

2 FLOPPY MODES IN NETWORK GLASSES **8**

2.1 INTRODUCTION 8

2.2 CONSTRAINT COUNTING 10

2.3 ELASTIC MODULI 12

2.4 DENSITY OF STATES 18

2.5 DEBYE WALLER FACTOR 24

2.6 CONCLUSIONS 30

3 RIGIDITY OF INTERCALATED LAYERED SOLIDS **34**

3.1 INTRODUCTION 34

3.2 THE MODEL 40

3.3 ANALYTIC SOLUTION 42

3.4 CORRELATED CASE 52

3.5 EFFECTIVE MEDIUM THEORY 55

3.5.1 Random Intercalation 55

3.5.2 Correlated System 58

3.6 PROBABILITY DISTRIBUTION FOR GALLERY HEIGHTS 63

3.6.1 Distribution Function $P_A(d)$ and $P_B(d)$ 65

3.6.2 Low and High Concentrations 68

3.7 CONCLUSIONS 70

4 STRUCTURAL CHARACTERISATION OF SEMICONDUCTOR ALLOYS 73

4.1 INTRODUCTION 73
4.2 VALENCE FORCE MODELS 74
4.3 THEORY 78
  4.3.1 Solution to Pure Length Mismatch 79
  4.3.2 Watson Integrals as Function of Force Ratio 81
  4.3.3 Effective Medium Theory 81
4.4 APPLICATION 84
4.5 CONCLUSIONS 93

5 DIFFRACTION FROM RANDOM ALLOYS 96

5.1 INTRODUCTION 96
5.2 COMPUTER SIMULATIONS 97
  5.2.1 Bragg Scattering 99
  5.2.2 Huang Scattering 101
5.3 THEORY 101
  5.3.1 Bragg Scattering 101
  5.3.2 Huang Scattering 105
5.4 RESULTS 108
  5.4.1 Bragg Scattering 108
  5.4.2 Huang Scattering 111
5.5 DISCUSSION 111
5.6 CONCLUSION 113

6 TWO DIMENSIONAL MIXED CRYSTAL 117

6.1 INTRODUCTION 117
6.2 SHORT RANGE PROPERTIES 121

6.3 DIFFRACTION PATTERN 122
6.4 ANGULAR CORRELATION 130
6.5 FINITE SIZE SCALING 133
6.6 CONCLUSION 134

7 OVERVIEW AND PERSPECTIVE 138
7.1 LENGTH MISMATCH PROBLEM 138
  7.1.1 Quaternary Solution and Sublattice Decoupling 138
  7.1.2 Topological Rigidity Constants 148
7.2 MODEL AND MATHEMATICS 150
7.3 TWO DIMENSIONAL INSTABILITY 155

A The Equation of Motion 160

B Distribution Function of Multilayer System 163

C Symmetric Distribution Case 166

D Average NN-distance in Semiconductor Alloys 168

List of Tables

4.1 force constants 77
4.2 Formula constants 81

List of Figures

2.1 Modulus versus mean coordination 13

2.2 C_{11} with weak force on 16

2.3 C_{12} with weak force on 17

2.4 Density of state 21

2.5 Density of state 22

2.6 $\rho(\omega)/\omega$ 23

2.7 $\rho(\omega) = \alpha\omega^2|_{\omega=0}$ 25

2.8 The -1 moment of DOS 27

2.9 The -2 moment of DOS 29

3.1 Intercalated Graphite 36

3.2 Intercalated Graphite with impurity 37

3.3 Intercalation of two type atoms 38

3.4 Stronger layer with intercalation 39

3.5 Z-curves 47

3.6 Strain energy curves 48

3.7 Width curves 49

3.8 Anticlustering intercalation 50

3.9 Clustering intercaltion 51

3.10 Z-curves 59

3.11 Strain energy 60

3.12 width curves 61

3.13 probability of distribution 64

4.1 Watson integral 82
4.2 "Z" curves for $III-V$ compounds 85
4.3 "Z" curves for $III-V$ compounds 86
4.4 "Z" curves for $II-VI$ compounds 87
4.5 "Z" curves for $II-VI$ compounds 88
4.6 "Z" curves for $In_{1-x}Ga_xAs$ 89
4.7 "Z" curve for $Cd_{1-x}Zn_xTe$ 90
4.8 Length distribution of $Cd_{0.5}Zn_{0.5}Te$. 92

5.1 Triangular lattice 98
5.2 Bragg scattering 100
5.3 Huang scattering 102
5.4 Huang scatter(larger mismatch) 103
5.5 Mean squared displacement 109
5.6 Wilson plot 110

6.1 Triangular lattice 119
6.2 Triangular lattice with mismatch 120
6.3 The density-density correlation function 125
6.4 Diffraction pattern 127
6.5 Triangular lattice with pleating 128
6.6 Pleating transition 129
6.7 Angular correlation function 13

7.1 Quaternary Distribution 14
7.2 $Si_{1-x}Ge_x$ 15
7.3 $Ga_{1-x}In_xAs$ 15
7.4 Next nearest neighbor distance 15

7.5 Melting of 2d LJ system 157
7.6 Topological Defects in 2d 158

Chapter 1

INTRODUCTION

Solid state theory first was a theory for crystals, for the simple reason that one learns walking before running. Systems with periodicity have been well studied, and we have beautiful and powerful mathematical means (Bloch theory, Group theory) in hand. The study on amorphous systems where long-range-order no longer exists became active thereafter. There are strong demands from application because of the various optical and electronic properties of the amorphous materials, and also because of the richness of such materials with their imperfection. Examples of applications include the use of ultratransparent optical fibers in telecommunications, the use of amorphous semiconductors in xerography and solar cells, and the ubiquitous everyday uses of organic glasses as structural materials. Scientifically, it has been a long struggle to understand the real beauty behind the seemingly disordered and constantly changing world. It is necessary to first have a good understanding of crystals. Based on that, perturbation theories of various kind could be performed. Yet new concepts and new methods are needed to deal with disorder comprehensively. Localization and percolation theory are the main ones that have met the new challenges. Some old approaches, such as the chemical bonding viewpoint, remain useful. The most important thing in studying amorphous material is the scientific insight. Our approaches are based on studying simple models which carry the main features of the corresponding physical systems and also have soluble limits. The effort is to sort out the essence of the physical phenomena that have the dominant effect on the observations. In this thesis we will discuss the application of chemical bonding, which is related to short range order, topological rigidity and rigidity percolation.

This dissertation is basically a collection of the works the author has been involved in during the Ph. D. program. Chapter **2** is published in Phys. Rev. B**40**, 10535(1989), it is finished under the guidence of Prof. M. F. Thorpe. The author also makes major contributions both in theory and computation to the works described in Chapter **3** (Phys. Rev. B**42**, 8827(1990)), Chapter **4** and **7** (to be sent to Phys. Rev. B). Prof. M. F. Thorpe worked out most of the theory described in Chapter **5** (Phys. Rev. B**43**, 8282(1991)) and **6** (Phys. Rev. B**43**, 11019(1991)) and the author did the major work in computer simulations and part of the work on the theory.

Because each chapter can be treated as an independent paper, and as a matter of fact many of the papers have been published, there are some notation differences between these chapters. For example, we use "W" to denote the Watson Integrals in Chapter **3**, and in other chapters we use "a^{**}". In some chapters we call the Watson Integrals the "Topological Rigidity Parameters" because of better understanding of its physical meaning. I hope this explanation could ease the inconvenience created to the readers because of these changes in notation. Bibliographies also follow each chapter as in an independent paper.

The next chapter presents the concept of rigidity percolation. The percolation concept is very important in disordered systems. It is a powerful unifying construction and an outstanding vehicle for exhibiting many of the modes of thought characteristic of theoretical approaches to strongly disordered systems: emphasis on statistical distributions, transition between localization and delocalization, critical points, scaling behavior, and dimensionality dependence etc.

Rigidity percolation is about the elastic response of a system. In a lattice network, rigidity percolation always occurs after conductivity percolation. The reason is because conductivity percolation concerns the connectivity while the rigidity percolation concerns the constraints. Constraint on a lattice site implies the existance of connectivity of this site to others. There has been questions whether these two types of percolation belong to the same universal class. They are not necessarily the same because of different symmetry. And there have been theoretical work that prove it by presenting different critical exponents. Beyond the universality problem, rigidity percolation is a useful concept in investigating the mechanical properties of covalent glasses.

In **Chapter 2** we discuss how the concepts from rigidity percolation can be used to understand the low-frequency excitations and elastic properties of network glasses like $Ge_xAs_ySe_{1-x-y}$. When the mean coordination $\langle r \rangle = 2+2x+y$ is low, these materials are soft and their properties are strongly influenced by low-frequency phonons. We use a bond-depleted diamond lattice to mimic the coordination properties of the glass. We show that a model with only covalent forces is unstable for $\langle r \rangle < 2.4$ but can be stabilized by small additional forces. We calculate the elastic constants, the density of states, and the Debye-Waller factor as a function for $\langle r \rangle$. Despite the simplicity of the model, the phase transition at $\langle r \rangle = 2.4$ is consistent with recent experimental results involving ultrasonics, inelastic neutron scattering, and Mõssbauer experiments on Ge_xSe_{1-x} glasses. The floppy modes, observed in inelastic neutron scattering, disappear as $\langle r \rangle$ increases from 2 up to 2.4.

The later chapters mainly deal with the "length mismatch problem." There are many approaches to disordered materials. People have studied the mass and compressibility disorder. The calculation of electronic band structure of semiconducting alloys needs the configuration of the compound system. Theoretical calculations usually adopt the virtual crystal model. In this model the positional disorder is averaged out and the lattice constant is taken to be an averaged constant. One reason comes from the simplicity after such averaging and the other is that the detailed structural information needed is unavailable for technical reasons. The predictions are many times not very good. And the need for structural information is essential for any improvement. Our research focuses on the disorder caused by size difference. The reason lies in the fact that the differential size effect has very dominant effect on the structural properties of a large group of materials, like $II-VI$ and $III-V$ ternary compounds such as $InGaAs$, and quaternary semiconductor alloys such as $InPGaAs$. On the experimental side, EXAFS experiments are now capable of detecting the nearest and next nearest neighbor distances. This parallel development is very encouraging and provide checks to the ideas used in the theory. And the feedback is a better and clearer understanding of the physical phenomena from a microscopic point of view. The models we have used are very simple, which can be seen through all the chapters. But they grasp the main features of the problems. For the size mismatch problem, the simplest model is the lattice network of "bond" disorder. It is not the best to represent an alloy system, but is pretty good in describing the intercalated graphite multilayer system. For binary and ternary compounds, a better model is a lattice network of "site" disorder. We studied both models. The useful concepts are the chemical bonding and atomic radii. Pauling first studied these concepts. The stability of chemical bonding leads to the introduction of the natural length of that bond. It is similar to the natural length of a Hook spring. The additivity of atomic radii to give natural bond length is very useful because our model can be solved exactly under such conditions. In reality, the approximation we made are good for many systems and provide a good starting point for others where the conditions are not satisfied. For example, there are disorder in the local compressibility, and the natural bond lengths may not be additive from the atomic radii. It is even possible that natural length is not a very stable concept when charge transfer is important and varies from one environment to another. From the perturbation analysis we can understand the condition for the validity of Vegard's law and the trend of the deviation. For instance, effective medium theory can be introduced to describe systems when there is also disorder in the force constants.

In **Chapter 3**, we investigated the gallery structure of intercalated multilayer systems $A_{1-x}B_xL$, assuming that the intercalants A and B are randomly distributed in each gallery flanked by host layers L. We allow for the correlation between the intercalants in different galleries denoted as interlayer correlation (ILC). The gallery structure is characterized by an average gallery height, by fluctuations in the gallery height from site to site, and by a complete height distribution function. These quantities have been studied by constructing a harmonic spring model which incorporates the ILC through a one-dimensional Ising spin model. We have obtained an exact solution for this model for arbitrary ILC when the two intercalants have the same compressibility ($k_A = k_B$). In this limit, we show that Vegard's law is obeyed for all values of the transverse rigidity of the host layers and arbitrary ILC. In the general case ($k_A \neq k_B$), we have developed an effective-medium theory whose results are in excellent agreement with computer simulations.

While the above gallery model is very useful in its own right in studying the intercalated graphite multilayer system, it is the first step toward the length mismatch problem we have studied in the alloy systems.

In **Chapter 4** we have made an exhaustive study of all pseudobinary semiconductor alloys $(A_{1-x}B_x)C$. This includes both the $III-V$ and the $II-VI$ alloys. We use a Kirkwood model with parameters derived from the elastic constants of the pure materials. It is shown that the mean lengths are linear in the composition x if the spring constants for the two pure materials AC and BC are the same. This is because the displacement fields due to the various inclusions can be superimposed. Curvature is caused by the many body effects in the concentrated alloy that occur when the force constants for AC and BC differ. We obtain analytic results for the mean lengths for AC and BC bonds and for their widths using effective medium theory, which is in excellent agreement with the results of computer simulations of the same models. The length distribution function for nearest neighbor bonds of a particular type, is shown to be well approximated by a Gaussian.

What we studied In **Chapter 4** are only the short range order properties. It should be pointed out that the mismatch problem can be solved in the quaternary model when the structural information are concerned. We discuss this further in the last chapter.

Chapters 5 and 6 deal with not only the short range properties but also with the long range properties in a length mismatched lattice network. The studies are performed for 3d systems and 2d systems. In **Chapter 5**, we calculate the diffraction from random alloys, consisting of bonds of different natural lengths. The resulting structure is a distorted crystal with strong correlations between displacements at different sites. The diffraction pattern is dominated by a set of Bragg peaks whose intensity is modulated by a Debye-Waller factor. At the base of each of these Bragg peaks, we find divergent Huang scattering due to the second order correlations between displacements. Higher order correlations produce a negligible non-divergent background. Results are obtained in closed form and compared with computer simulations.

In **Chapter 6** we show that the long range positional order in a two dimensional crystal $A_{1-x}B_x$ is destroyed by size-mismatch disorder as well as by thermal disorder. The size-mismatch disorder is characterized by an effective *temperature* $k_BT_D = Kx(1-x)(L_B^0 - L_A^0)^2$ associated with the strain energy, where K is a force constant, $L_B^0 - L_A^0$ is the length mismatch and x is the concentration. We study a model which has a fixed triangular net topology. By comparing with computer simulations, we show that a linearized small displacement theory is adequate for small size-mismatches. The long range orientational order remains. The positional correlation function decays algebraically, which leads to power law peaks that replace the Bragg peaks in the diffraction pattern. We argue that this model should provide a reasonable qualitative description of real two dimensional mixed crystals, in the limit of small size-mismatch.

When we relax the topological constraint by replacing the harmonic spring potential by, for example, a Lennard-Jones potential, the study on the 2d alloy system leads us to the instability problem, which we referred to as 2d length-mismatch-driven-melting. We call it melting in the sense that the shear modulus drops dramatically when mismatch reaches certain value and the system becomes very soft. We come back to this discussion in the last chapter, too.

We summarize our main theoretical results in the last chapter from a mathematical point of view and discuss the models we used. We discuss the role played by topological rigidity parameters that have frequently appared in the above chapters. After giving a summary of the "length mismatch problem", we discuss the 2d instability which is very interesting and not completely solved yet.

Chapter 2

FLOPPY MODES IN NETWORK GLASSES

This chapter is published in Physical Review B. Reference: Y. Cai and M. F. Thorpe, Phys. Rev. B**40**, 10535(1989).

2.1 INTRODUCTION

Many network glasses are well described by the Continuous Random Network (CRN) model first discussed by Zachariasen[1] more than 50 years ago. Examples are Si and Ge that like to make 4 bonds in a tetrahedral arrangement; As that makes 3 bonds; and S, Se and O that make 2 bonds. A CRN can be described by a chemical formula like $Ge_xAs_ySe_{1-x-y}$ $(0 < x, y < 1)$. If the total number of atoms is N and there are n_r atoms with coordination r ($r = 2$, 3 or 4) then

$$N = \sum_r n_r, \tag{2.1}$$

and we can define the mean coordination $\langle r \rangle$ by

$$\langle r \rangle = \sum_r r n_r / \sum_r n_r = 2 + 2x + y \tag{2.2}$$

We note that $\langle r\rangle(2 < \langle r\rangle < 4)$ gives a partial, but very important, description of the network. We will also see that the elastic properties depend sensitively on $\langle r\rangle$.

We regard a perfect CRN with no dangling bonds as being analogous to the perfect crystal. In practice one can approach a perfect CRN by careful preparation techniques in which the number of dangling bonds is kept to a minimum. In some circumstances the CRN model is inappropriate and the network has effectively lower dimensionality and may be better thought of as a spaghetti of twisted ribbons.[2] The ideas that we are discussing in this chapter also apply to such networks if suitable adjustments in the theory are made.

The standard procedure for constructing a CRN is to hand build a model using hundreds to a few thousand appropriate chemical units.[3] More recently, such networks have also been made by restructuring diamond cubic networks.[4],[5] This has led to satisfactory networks for Si and for SiO . Molecular dynamics techniques have also been used to construct such networks, starting from a random configuration of ions interacting with prescribed potentials.[6] Both these computer based techniques are superior to hand building because they are unprejudiced by the builder and have periodic boundary conditions. For a given size of model, periodic boundary conditions are preferable as they maintain the coordination. While this is of some minor help in calculating static quantities, like the radial distribution function, it is of much greater importance for dynamic quantities, like the density of states, that we will be mainly concerned with in this chapter. Unfortunately to date, neither of the computer generated techniques mentioned above has been used to build non-stoichiometric networks, although molecular dynamics could probably be adapted to do so. Hand building a series of networks for the studies in this chapter would be prohibitively time consuming and would yield structures with free boundaries.

Our belief and experience is that the coordination of the constituent ions is the main determining feature of these networks for vibrational properties.[7],[8] We have therefor used a simple bond depleted diamond cubic crystal lattice. This model was first introduced by He and Thorpe[8] in a calculation of the elastic moduli as a function of $\langle r \rangle$. Bonds are removed randomly to produce 3 and 2 fold coordinated sites. If the removal of a bond would result in a dangling bond, that move is not allowed. He and Thorpe showed that the values of x,y in Eq.(2.2) were important only through $\langle r \rangle$ by also removing bonds in a correlated way. That is if all the sites were 3 coordinated (representing As), the elastic properties were essentially the same as those for a $50 : 50$ mixture of 2 and 4 coordinated sites. This assumes of course that the forces between the atoms are independent of the chemical species. We will comment later on this more.

The layout of this chapter is as follows. In the next section we review the constraint counting arguments that lead to a transition at $\langle r \rangle = 2.4$. In Sec. **2.3**, we compute the elastic moduli with the covalent forces only, and with the covalent plus weak forces. In Sec.**2.4**, we calculate the density of states using the equation of motion method. The low frequency floppy modes are seen to agree well with recent experimental measurements in Ge_xSe_{1-x}. In Sec.**2.5**, we use the results from the density of states to calculate the Debye Waller factor that has recently been measured in a Mössbauer experiment. In all cases, quantities are calculated as functions of $\langle r \rangle$ and comparisons are made with experimental measurements on Ge_xSe_{1-x}. The equation of motion technique is described in **Appendix A** in two different versions; the conventional one involving "plucking" and a variation involving a "kick start" that is necessary to get good results at very low frequencies.

2.2 CONSTRAINT COUNTING

In covalent networks like $Ge_xAs_ySe_{1-x-y}$, the bond lengths and angles are well defined and small displacements from a (supposed) equilibrium structure can be described by the potential[8]

$$V = \frac{\alpha}{2} \sum_{\langle ij \rangle} [(\mathbf{u}_i - \mathbf{u}_j) \cdot \hat{\mathbf{r}}_{ij}]^2 + \frac{\beta}{2} \sum_{ijk} l_{ij} l_{jk} (\Delta\theta_{ijk})^2. \tag{2.3}$$

We will refer to this as the covalent potential as it has bond stretching and bond bending terms. Here $\mathbf{u}_i$ is the displacement of the atom i and $\hat{\mathbf{r}}_{ij}$ is a unit vector connecting nearest neighbor sites i, j; l_{ij} is the length of the bond ij and θ_{ijk} is the angle between the bonds ij and jk. The bond stretching force constant α and the bond bending force constant β, are the largest forces in covalent glasses. Other forces are smaller as would be expected from the nature of the covalent bond. The potential in Eq. (2.3) has been written as harmonic but this is not important in what follows in this section as we shall be making small virtual displacements. The detailed form of the potential will be important when we come to calculate spectral responses later.

We will regard the solution of the eigenmodes of the potential in Eq.(2.3) as a problem in classical mechanics .[9] The dynamical matrix has a dimensionality $3N$ which corresponds to the $3N$ degrees of freedom. In a stable rigid network we would expect all the squared eigenfrequencies $\omega^2 > 0$ with 6 modes at zero frequency. These 6 modes are just the 3 rigid translations and the 3 rigid rotations and have no weight in the thermodynamic limit. However we will find that in some covalent networks, described by the potential in Eq. (2.3), there are a significant number of additional zero frequency modes which correspond to internal deformations of the network. The number of such modes can be determined by counting the constraints in the system. There is one constraint associated with each bond which we can assign as $r/2$ constraints associated with each r coordinated atom. In addition there are constraints associated with the angular forces in Eq. (2.3). For a 2 coordinated atom there is one angular constraint, for a 3 coordinated atom there are three angular constraints and for an r coordinated atom there are a total of $2r - 3$ angular constraints.[7] The total number of constraints is equal to the number of finite frequency modes which are therefore

$$\sum_r n_r[r/2 + (2r - 3)] \tag{2.4}$$

The fraction f of zero frequency modes is given by

$$f = \{3N - \sum_r n_r[r/2 + (2r - 3)]\}/3N \tag{2.5}$$

which can be rewritten as

$$f = 2 - \frac{5}{6}\langle r\rangle \tag{2.6}$$

where $\langle r\rangle$ is defined in Eq. (2.2). When $\langle r\rangle = 2$(e.g. Se chains), then $f = 1/3$; that is one third of all the modes are at zero frequency. As atoms with higher coordination than 2 are added to the network, f drops and goes to zero at $\langle r\rangle = 2.4$ and the network becomes rigid.

2.3 ELASTIC MODULI

In order to simulate a CRN, bonds were removed at random from a series of diamond lattices in such a way that sites with 2, 3 and 4 fold coordination were produced. The networks had periodic boundary conditions and the supercell contained 216 atoms. This was the largest network that could easily be handled when the weak forces are included. We found that the results were not very size dependent by looking at a few networks with 512 atoms. If removing a bond would result in a dangling bond that removal was not allowed. Using this technique, networks with $\langle r\rangle$ as low as 2.082 can be produced. The covalent potential in Eq. (2.3) is rewritten to apply more conveniently to this situation as,

$$V = \frac{\alpha}{2}\sum_{\langle ij\rangle} P_{ij}(\mathbf{u}_{ij}\cdot\hat{\mathbf{r}}_{ij})^2 + \frac{\beta}{2}\sum_{\langle ijk\rangle} l^2 P_{ij}P_{jk}(\mathbf{u}_{ij}\cdot\hat{\mathbf{r}}_{ik} + \mathbf{u}_{ik}\cdot\hat{\mathbf{r}}_{ij})^2, \tag{2.7}$$

where the probability that the bond ij is present or missing is included by letting P_{ij} be either one or zero. Here all the bond lengths l are the same and $\mathbf{u}_{ij} = \mathbf{u}_i - \mathbf{u}_j$. The angular force involving β is not quite the same in Eq. (2.7) as in Eq. (2.3) but we have found the potential (2.7) a little easier to use in numerical calculations. It can be seen from the insert in Fig.(2.1) that all the elastic constants C_{11},C_{12} and C_{44} go to zero around $\langle r\rangle = 2.4$.

In order to stabilize the lattice and move the floppy modes away from zero frequency,

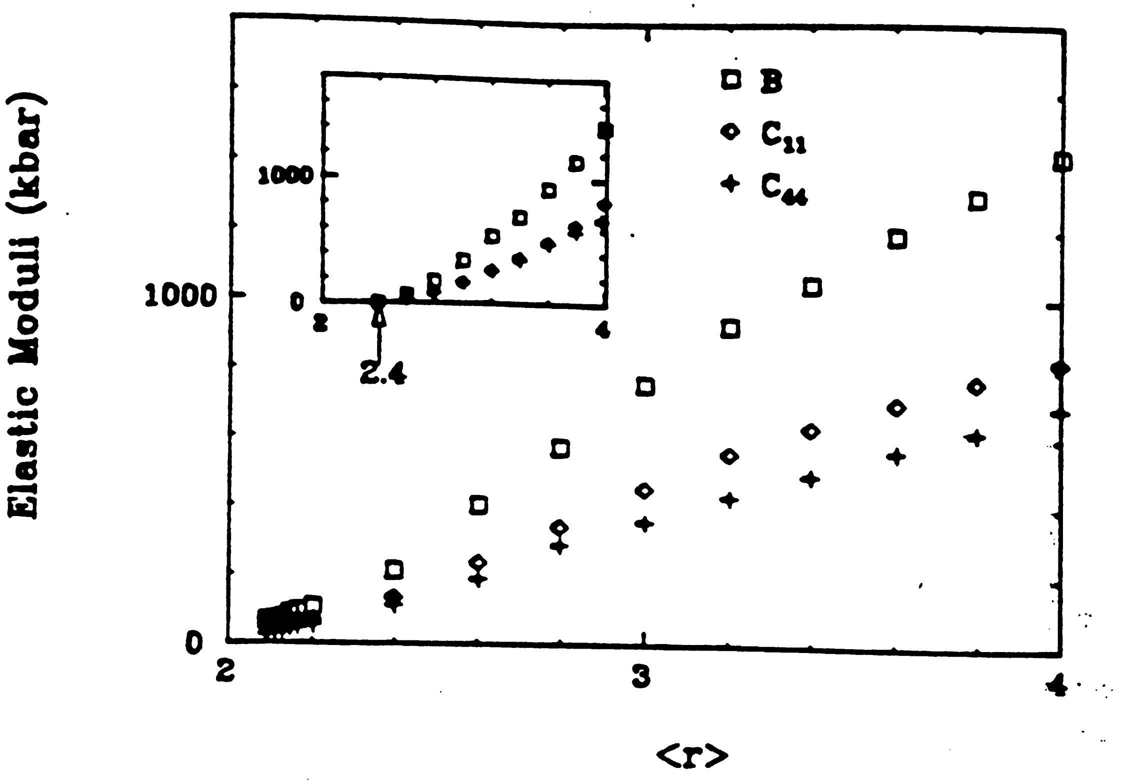

Figure 2.1: The elastic moduli C_{11},C_{12} and B with $\beta/\alpha = 0.3$ as a function of the mean coordination $\langle r\rangle$. The insert is without the weak forces and the main graph has the weak forces included.

we add a weak stabilizing potential V_s to the potential V given in Eq. (2.7),

$$V = \frac{\gamma}{2}\sum_{ijkl} P_{ij}P_{jk}P_{kl}(\Delta\phi_{ij,kl})^2 + \frac{\alpha'}{2}\sum_{ij}(1 - P_{ij})(\mathbf{u}_{ij}\cdot\hat{\mathbf{r}}_{ij})^2. \tag{2.8}$$

The first term in Eq. (2.8), proportional to γ, is the dihedral angle force involving the dihedral angle $\phi_{ij,kl}$ which by itself is sufficient to stabilize all zero frequency modes. However we found it convenient to add a small "interchain" term proportional to α' . This was so that we could position the two major frequency bands in roughly the correct places to agree with the experimentally determined density of states. This led to $\alpha : \beta : \gamma : \alpha' = 1 : 0.3 : 0.1 : 0.03$ and the overall magnitude of the force constants was chosen to get the maximum frequency correct. As we will see later, the maximum phonon frequency ω_{max} is rather insensitive to composition and we will take $\omega_{max} = 40$ meV $= 320$ cm^{-1} . This frequency is independent of γ and α' and given by $\omega_{max}^2 = 8(\alpha+\beta)/3M$ so that $\alpha = 1.28 \times 10^5$ dynes/cm and $\beta = 0.38 \times 10^5$ dynes/cm, where we have taken $M = 72.6$ amu as is appropriate to Ge; the masses of As and Se are not significantly different as they are next to Ge in the periodic table. For simplicity we therefor put all the masses equal. While these masses are irrelevant for the elastic constants, they do influence other quantities that we calculate. Using the ratios given above, the two weak force constants are $\gamma = 0.128 \times 10^5$ dynes/cm and $\alpha' = 0.038 \times 10^5$ dynes/cm. We stress again that we are not seeking detailed agreement with experiment, but are trying to get a reasonably accurate overview. These parameters are now taken as fixed for the rest of this chapter. No separate attempt was made to fit the elastic constants. The elastic moduli for the perfect diamond cubic crystal in the absence of the weak forces are given by

$$\begin{aligned} C_{11} &= (\alpha + 3\beta)/4a \\ \\ C_{44} &= (\alpha\beta)/[(\alpha+\beta)a] \\ B &= (C_{11} + 2C_{12})/3 = (3\alpha+\beta)/12a, \end{aligned}$$

where $l = a/\sqrt{3}$ is the nearest neighbor distance, which for Ge is 2.45Å. Using the values of α and β given above, we find that $C_{11} = 1433$ kbars, $C_{44} = 696$ kbars and $B = 830$ kbars. These are in close enough agreement to the experimental values $C_{11} = 1289$ kbars, $C_{44} = 671$ kbars and $B = 752$ kbars for our purposes.

From Fig.(2.1), we see that the weak forces stabilize the lattice as expected and lead to elastic moduli that are non-zero for all $\langle r \rangle$. The most dramatic effects are seen at low mean coordination where the singularity at $\langle r \rangle = 2.4$ is completely washed out. Note that we have used $\beta/\alpha = 0.3$ rather than 0.2 as in He and Thorpe.[8] One would have hoped, with the addition of the weak forces, that some traces of the singular behavior around $\langle r \rangle = 2.4$ might have been retained, but this is not the case. Of course, if we made the weak forces even smaller, then the singularity would start to become apparent. However the weak forces are as nature has given and cannot be altered. This situation is analogous to any other phase transition in a small field that couples to the order parameter; an example being the magnetization of a ferromagnet in a small external magnetic field.

For $\langle r \rangle > 2.4$, the network is mechanically stable and the elastic properties are largely determined by the covalent forces α, β. Other forces are small and can be neglected. For $\langle r \rangle < 2.4$, the network is mechanically unstable and we must include other weaker forces to stabilize the structure. In Figs. (2.2) and (2.3), we show a comparison between these results and the experimental results of Yun et al.[11] taken using ultrasonic data for the system Ge_xSe_{1-x}. Similar results have been obtained by a number of other authors,[12] and initial discrepancies with the data of Halfpap and Lindsay[13] have been resolved as being due to oxygen contamination. Also included in these plots are the results for a-Ge.It is not possible to make samples over the range $2.6 < \langle r \rangle < 4$, as phase separation occurs. These results do show the softening of both the longitudinal and transverse elastic constants of Se over Ge by more than an order of magnitude. Also the experimental results agree with the theory in not showing a singularity around 2.4. However the experimental variation of both C_L and C_T over the range $2 < \langle r \rangle < 2.6$ is significantly less in the experiment[11] than in the

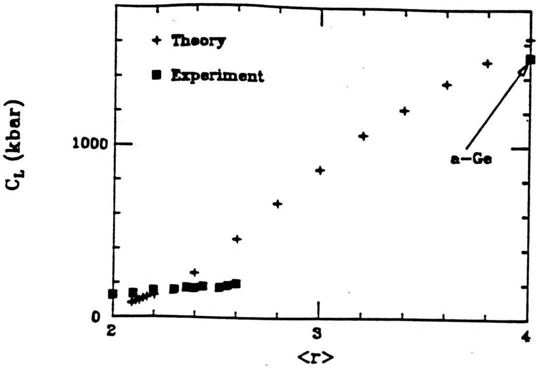

Figure 2.2: The longitudinal elastic modulus C obtained by averaging the results with the weak forces included, from Fig.2.1, is compared with experiment.

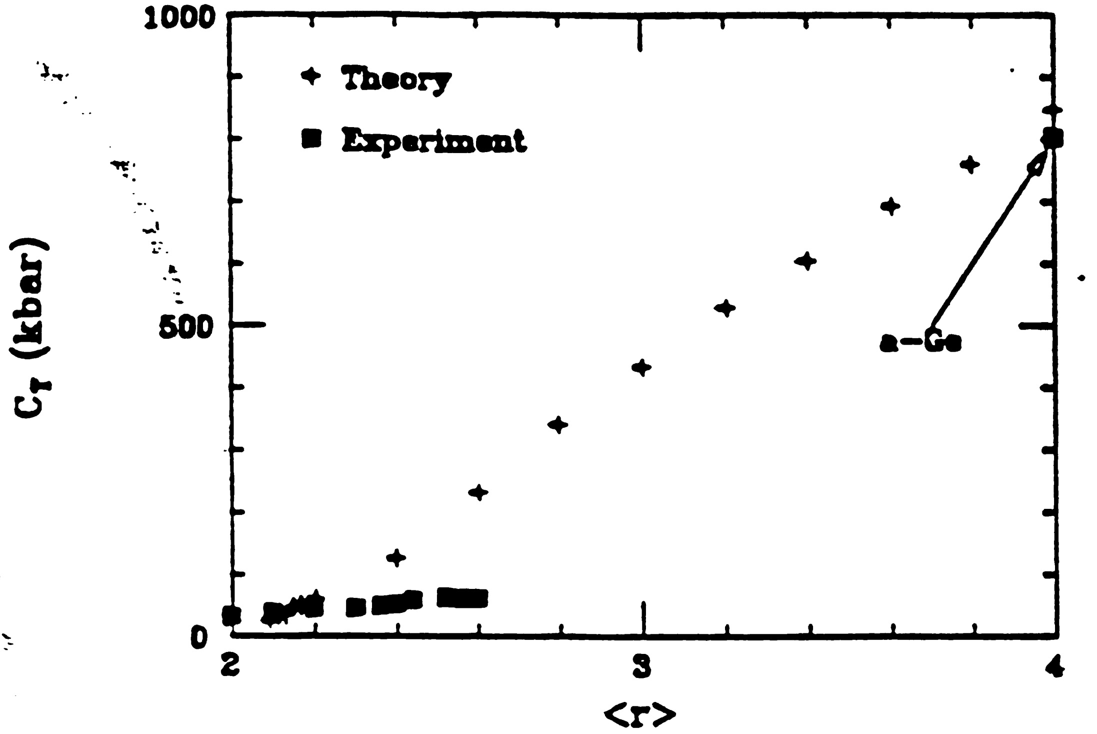

Figure 2.3: The transverse elastic modulus C obtained by averaging the results with the weak forces included, from Fig.2.1, is compared with experiment.

theory. We do not have any good explanation for this except that our model is very simple. It is hard to pinpoint the exact cause.

The model always maintains its cubic symmetry, on average, as the depletion takes place, whereas the real systems are isotropic. We have therefore done a very simple average over the principle directions to obtain the longitudinal C_L and transverse C_T elastic moduli from the theory.[8] We set

$$C_L = (6C_L^{100} + 8C_L^{111} + 12C_L^{110})/26 \tag{2.9}$$

and

$$C_T = (6C_T^{100} + 8C_T^{111} + 6C_{T1}^{110} + 6C_{T2}^{110})/26 \tag{2.10}$$

where C_{T1} and C_{T2} are the two different transverse moduli in the $\{110\}$ direction. Expressing these quantities in terms of the cubic elastic moduli C_{ij} as given in Kittel,[14] and using the relation for the bulk modulus $3B = 2C_{11} + C_{12}$, we find the longitudinal elastic constant,

$$C_L = (27C_{11} + 51B + 68C_{44})/78 \tag{2.11}$$

and the transverse elastic constant

$$C_T = (51C_{11} - 51B + 88C_{44})/156 \tag{2.12}$$

The results are not very sensitive to the precise way in which this averaging has been done. For an isotropic system, in which $C_{11} - C_{12} = 2C_{44}$, Eqs. (2.11) and (2.12) reduce to the result $C_L = C_{11}$ and $C_T = C_{44}$ as expected.

2.4 DENSITY OF STATES

More complete information about these systems is contained in the phonon density of states as a function of frequency. Such experiments have recently been completed for Ge_xSe_{1-x} glasses. Previously a density of states for a-Se had been obtained by Gompf,[15] which showed a sharp low frequency peak at around $\omega/\omega_{max} = 0.1$ that contains about 1/3 of the total weight. Here ω_{max} is the top of the phonon band which is quite insensitive to x, as we have remarked previously. Similar densities of states are obtained for the crystalline forms of Se where these low frequency modes can be associated with the torsional vibrations of the chains.[15] In the amorphous material we prefer to think of these modes as the zero frequency modes that are shifted to higher frequencies when additional terms are added to the potential given in Eq. (2.7). We shall refer to these as floppy modes. Inelastic neutron scattering measurements of the density of states in Ge_xSe_{1-x} glasses follow this low frequency peak as a function of composition. The frequency of the peak position does not shift much with x, but the weight in this peak rapidly decreases as x increases so the the anomalous modes have vanished by about $x = 0.2$ which corresponds to $\langle r \rangle = 2.4$. This is the behavior we would expect. The zero frequency modes produced by the potential (2.7) are moved from zero frequency to a low frequency by the additional weak terms like (2.8). However the weight in these floppy modes is still given approximately by Eq. (2.6) and decreases from 1/3 for Se to 0 for $Ge_{0.2}Se_{0.8}$. In order to better understand these experimental results, we have also employed the bond depleted diamond lattice discussed in the previous section.

Using the equation of motion technique,[16] as described in **Appendix A**, for an $8 \times 125 = 1000$ atom sample with periodic boundary conditions, we have calculated the density of states for various values of $\langle r \rangle$. The α component of the displacement for the ith atom $u_{i\alpha}(t)$ is computed using the equation of motion that results from the potential (2.7) or (2.8). The density of states $\rho(\omega)$ can be written as a cosine transform,[16]

$$\rho(\omega) = \frac{2}{\pi} \int_0^T dt \cos(\omega t) e^{-3(t/T)^2} \sum_{i,\alpha} A_{i\alpha} u_{i\alpha}(t), \tag{2.13}$$

where choosing the truncation time T determines the frequency resolution of the result. The exponential factor in (2.13) helps with convergence. Here the appropriate starting conditions for the density of states are,

$$u_{i\alpha} = A_{i\alpha} = \sqrt{2} \cos \theta_{i\alpha}, \tag{2.14}$$

where $\theta_{i\alpha}$ is a random angle uniformly distributed in the range $0 < \theta_{i\alpha} < 2\pi$. We also set the velocities $\dot{u}_{i\alpha}(0) = 0$. We refer to this as "plucking". Results are shown in Fig.(2.4) for various values of $\langle r\rangle$. At small values of $\langle r\rangle$ the zero frequency modes are broadened by the resolution function. It can even be seen that there are still a few states with zero frequency beyond $\langle r\rangle = 2.4$. This is because there is a very small, but finite, probability of finding undercoordinated regions even when $\langle r\rangle > 2.4$. This is a Lifshitz-type[17] argument. It can be seen in Fig.(2.4) that the floppy modes are moved into the low frequency peak and the weight is shuffled about within the rest of the spectrum. The maximum frequency does not change significantly as $\langle r\rangle$ is varied or when the weak forces in V are included.

In Fig.(2.5), we recalculate the spectra of Fig. (2.4), but using the "kick start" method described in **Appendix A**, that leads directly and naturally to the density of states divided by the frequency which accentuates the low frequency part of the spectrum. The quantity $\rho(\omega)/\omega$ can be written as a sine transform,

$$\rho(\omega)/\omega = \frac{2}{\pi}\int_0^T dt \sin(\omega t) e^{-3(t/T)^2} \sum_{i,\alpha} A_{i\alpha} u_{i\alpha}. \tag{2.15}$$

The theory is compared to experiment in Fig.(2.5). The experimental results were obtained using inelastic neutron scattering at a large wavevector transfer.[18] The floppy modes can be clearly seen in both the theory and the experiment although they are rather more pronounced in the theory. These experiments are quite difficult to do at low frequencies. As the mean coordination $\langle r\rangle$ is increased, the floppy modes are quenched out and vanish around $\langle r\rangle = 2.4$. Because of the rounding of the transition and the background phonons underneath the floppy modes, it is hard to be much more quantitative than this. Nevertheless the agreement between the experiment and our simple theory is impressive and convinces us that we have captured the essence of the behavior.

In Fig.(2.6), we replot the data of Fig.(2.5), but divide by an additional factor of the frequency. This is to accentuate the elastic behavior as well as the floppy modes. Both the experimental and theoretical spectra should head towards a constant at very

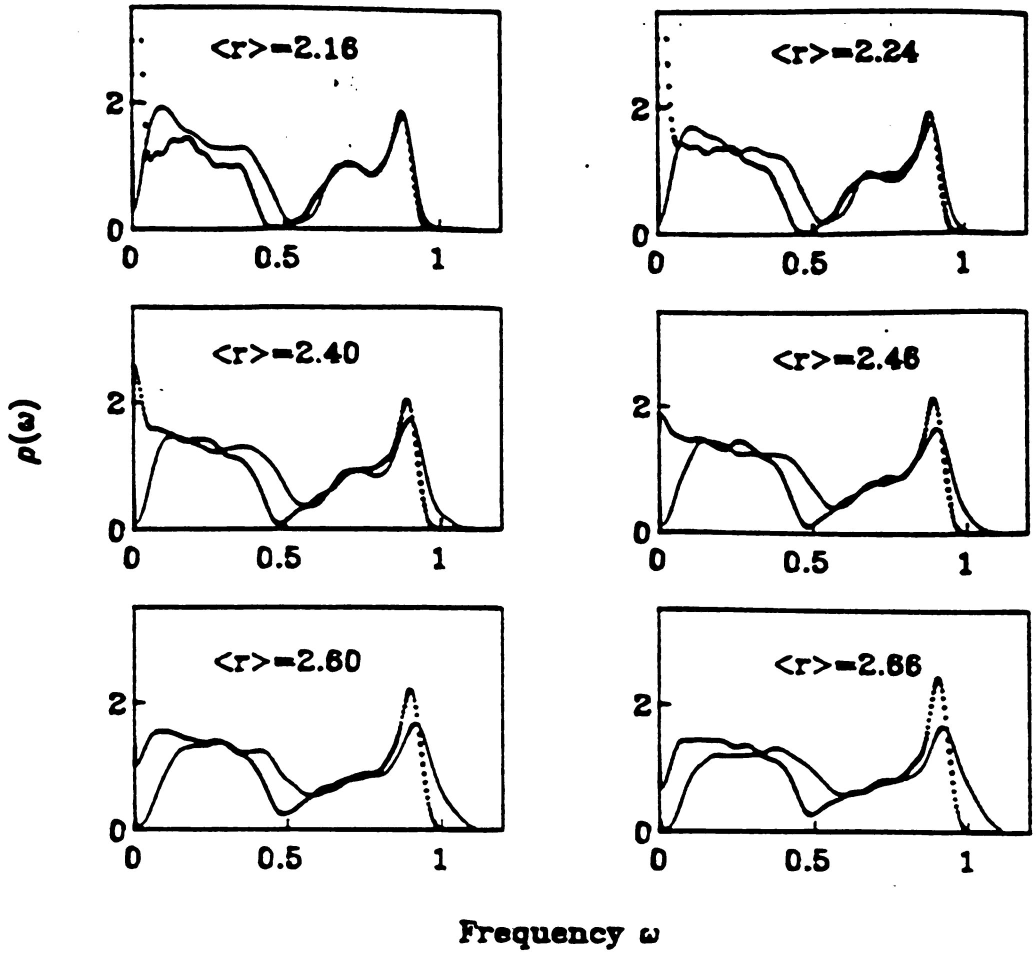

Figure 2.4: The density of states $\rho(\omega)$ for various values of the mean coordination $\langle r \rangle$. The dotted curve is without the weak forces, and the solid curve is with the weak forces included. The full width of the frequency resolution function is $\Delta\omega = \omega_{max}/20$. The frequency is in units where $\omega_{max} = 1$.

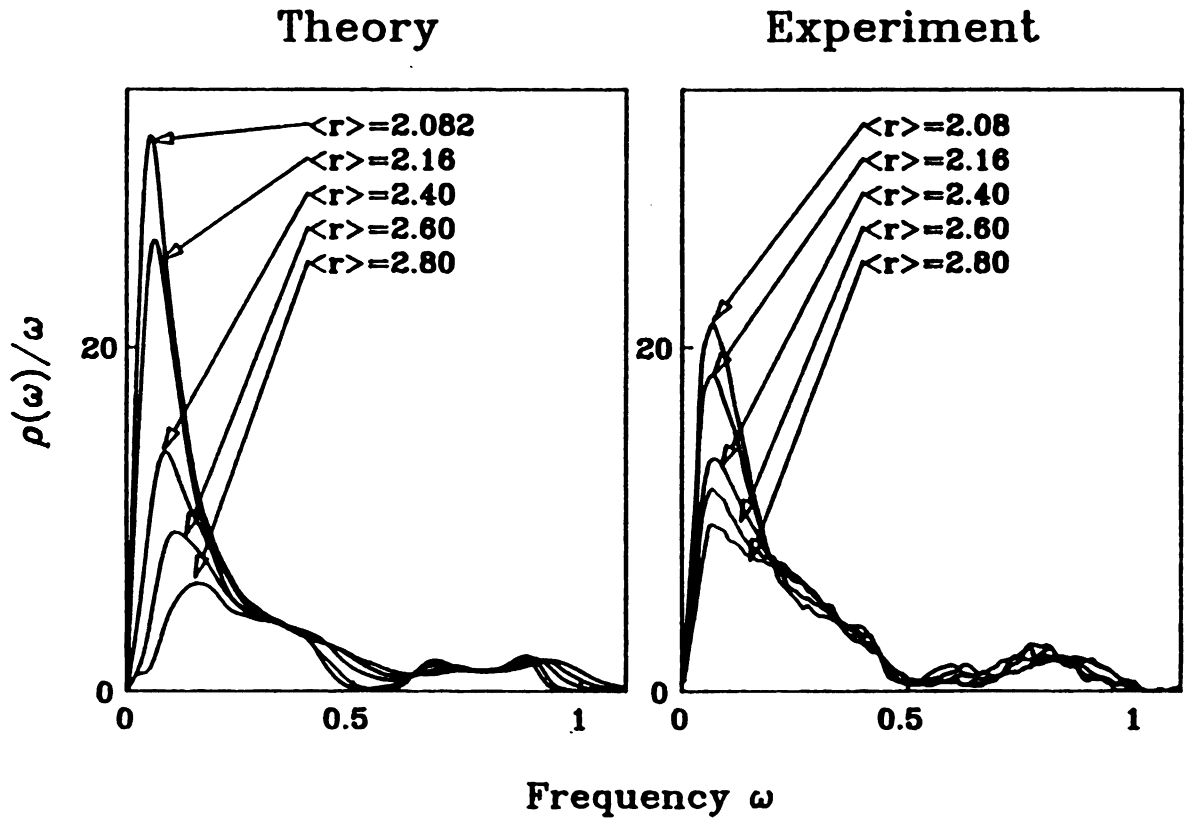

Figure 2.5: The density of states divided by the frequency, $\rho(\omega)/\omega$, for various values of the mean coordination $\langle r \rangle$. The left hand set of graphs are theoretical and the right hand set of graphs are from inelastic neutron scattering experiments.(Ref. [18]) The full width of the frequency resolution function for the theory is $\Delta\omega = \omega_{max}/20$. The frequency is in units where $\omega_{max} = 1$. ω_{max} is the maximum ω before the weak forces are turned on.

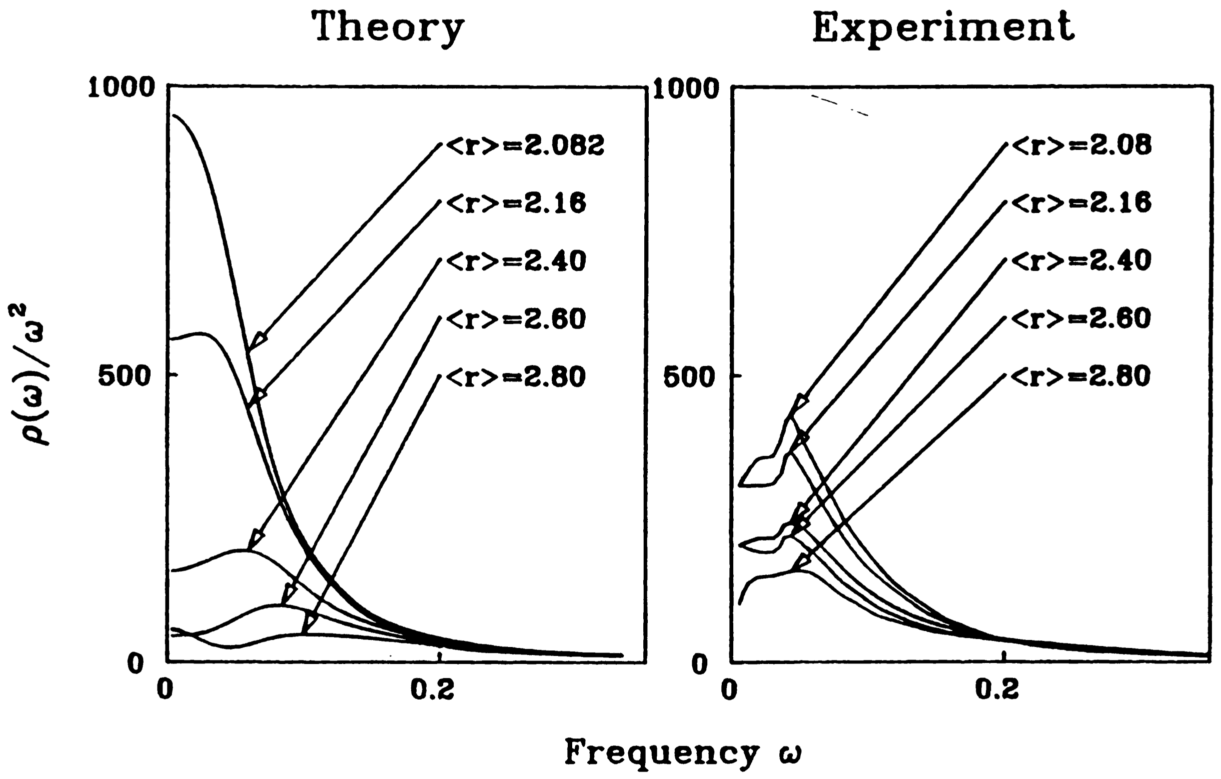

Figure 2.6: The density of states divided by the frequency squared for various values of the mean coordination $\langle r \rangle$. The data is derived from Fig.2.5. The left hand set of graphs are theoretical and the right hand set of graphs are from inelastic neutron scattering experiments. The full width of the frequency resolution function for the theory is $\Delta\omega = \omega_{max}/20$. The frequency is in units where $\omega_{max} = 1$. ω_{max} is the maximum of ω before the weak forces are turned on.

low frequencies, although there are difficulties in both the theory and experiment in getting accurate results in this part of the spectrum. The theoretical limit can be found from the elastic constants via the integral,

$$\rho(\omega)/\omega^2 \rightarrow \frac{V}{8\pi^2}\sum_{i=1}^{3}\int_0^{\pi}\int_0^{2\pi} C_i^{-3}(\theta,\phi)\sin\theta d\theta d\phi, \tag{2.16}$$

where the three velocities of sound $C_i(\theta,\phi)$ in the direction (θ,ϕ) are found by diagonalizing the appropriate 3×3 matrix. We have evaluated this integral numerically and the results are shown in Fig. (2.7). A similar analysis has been performed by Yun et al,[11] using their measured values of C_L and C_T and their results are also indicated in Fig. (2.7). These provide a consistency check within both the experiments and the theoretical model. We have had some difficulty getting good agreement between the two theoretical approaches at low frequencies, despite strenuous efforts. Probably larger models would be needed to take care of this point satisfactorily. However the theoretical elastic constants are much larger than the experimental ones at small $\langle r\rangle$. The agreement between the experiments and our simple model shows most of the qualitative understanding of the floppy modes is contained within the general arguments involving constraint counting etc. given in this chapter. We have taken care in plotting the results this way as it is important to have the low frequency behavior as accurately as possible in order to calculate the Debye Waller factors.

2.5 DEBYE WALLER FACTOR

The Debye-Waller factor, $\exp[-\langle(\mathbf{k}\cdot\mathbf{u})^2\rangle]$, modifies the intensity in many scattering type experiments. Here $\mathbf{k}$ is the momentum transferred to the sample. A measurement of this quantity allows the mean square displacement to be extracted. The mean square displacement in a particular direction for a single frequency is given by $\langle x^2\rangle$, where

$$\langle x^2\rangle = \frac{h}{M\omega}(\bar{n}+\frac{1}{2}), \tag{2.17}$$

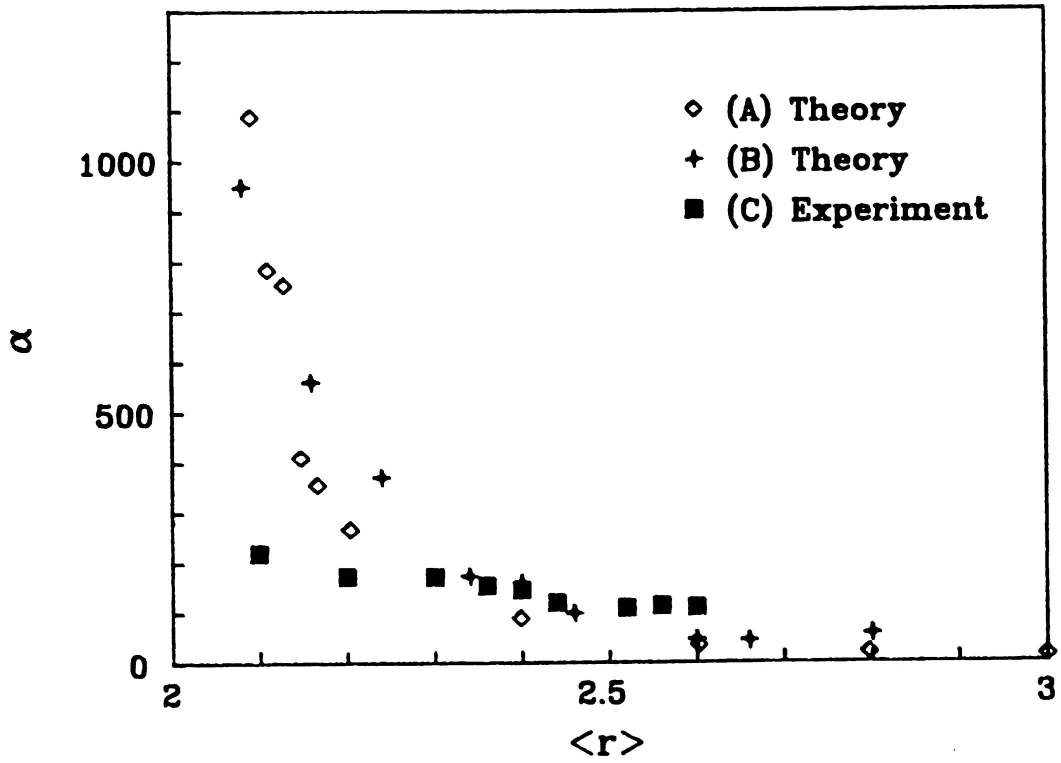

Figure 2.7: The coefficient a defined by $\rho(\omega) = \alpha\omega^2$ at low frequencies. The results are (A) theory using the elastic moduli determined statically (B) theory using the equation of motion method and (C) the elastic moduli from experiment. The units are the same as those used in Figs. 2.4-2.6 with $\omega_{max} = 1$.

and $\bar{n}$ is the Planck function.[19] At low temperatures, this becomes

$$\langle x^2 \rangle = \frac{h}{2M\omega}, \tag{2.18}$$

and at the high temperatures classical limit,

$$\langle x^2 \rangle = \frac{k_B T}{M\omega^2}, \tag{2.19}$$

where k_B is Boltzmann's constant. For the many harmonic oscillators in the systems under study here, we must average over all the eigenmodes of the system. We define the moments

$$\langle \omega^n \rangle = \int_0^\infty \rho(\omega)\omega^n d\omega / \int_0^\infty \rho(\omega) d\omega. \tag{2.20}$$

At low temperatures, we may extract the $n = -1$ moment and at high temperatures we may extract the $n = -2$ moment. At both these two extremes the Debye-Waller factor is very sensitive to the low frequency part of the spectrum. Indeed this is true at all temperatures.

It is very dangerous to use the computations reported in Fig. (2.4) to calculate these moments as the density of states in Fig.(2.4), with the weak forces included, have a small finite value at $\omega = 0$ due to the resolution function and the cosine factor in Eq. (2.13). We have computed the area under the curves in Figs.(2.5) and (2.6) directly. However, it is better to compute this quantity directly using Eq. (A.15) in **Appendix A**. This is equivalent to integrating over Eq. (A.15). The result can be obtained more directly using the single integral form in Eq. (A.15), and we have checked that a direct integration of the area under Fig.(2.5) leads to the same result. The results for the $r = -1$ moments are shown in Fig.(2.8) for various values of $\langle r \rangle$. It can be seen that the vibrational amplitudes increase as $\langle r \rangle$ decreases, and appears to show a small discontinuity of slope around $\langle r \rangle = 2.4$. We should emphasize that these results are calculated with the weak forces included. A similar procedure can be applied directly to the experimental results shown in Fig.(2.5), to yield the $r = -1$ moment and these results are shown in Fig. (2.8) also. Both these results

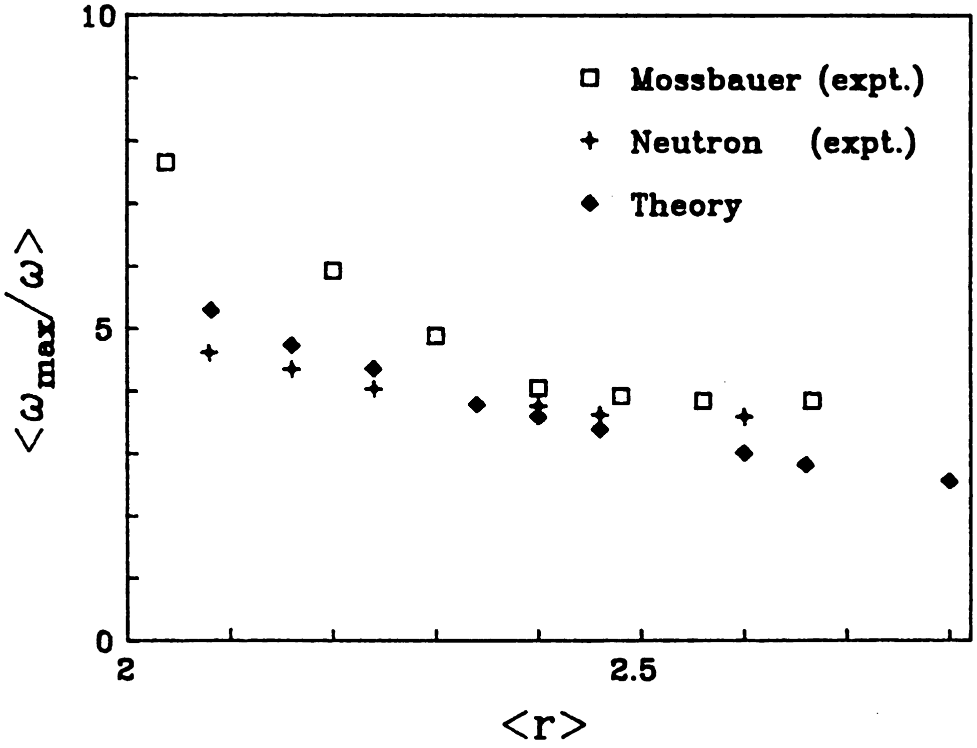

Figure 2.8: The $r = -1$ moment $\langle \omega_{max}/\omega \rangle$ for various values of the mean coordination $\langle r \rangle$. The figure shows a comparison of results obtained from Mössbauer and inelastic neutron scattering experiments with our theoretical results.

are compared with a direct measurement of this moment from the low temperature Mössbauer data.[20]

We can obtain the $r = -2$ moment by directly integrating the area under the graphs in Fig. (2.6). It is possible to write this moment as a single integral similar to Eq. (A.15). However, this is a more difficult quantity to calculate than the $r = -1$ moment as the single integral form is only conditionally convergent at large t, and we found it unreliable to work with. We have therefore integrated directly the areas under the curves in Fig. (2.6). This yielded fairly reliable results, but the results for $r = -2$, shown in Fig. (2.9) for various values of $\langle r \rangle$, are somewhat less accurate than those for $r = -1$ in Fig. (2.8). This same quantity was also obtained from the neutron data[18] shown in Fig. (2.6). These results are compared to the results from the Mössbauer experiments[20] at high temperatures. The vibrational amplitudes increase as $\langle r \rangle$ decreases, and possibly show a small discontinuity of slope around $\langle r \rangle = 2.4$. There is really no discontinuity in a thermodynamic sense in the results for the $r = -1$ and $r = -2$ moments as the transition is washed out by the weak forces. However the results of Figs. (2.8) and (2.9) do show more sharply defined changes around $\langle r \rangle = 2.4$ than the density of states themselves.

These results show that most of the contribution to the $r = -1$ moment comes from the floppy modes in the low frequency peak making the low temperature measurement of the Debye-Waller factor a sensitive probe of the floppy modes. The $r = -2$ moment probes even lower frequencies and is sensitive to both the floppy modes and the acoustic modes as can be seen from Fig. (2.6).

The preliminary analysis of Mössbauer results[20] seem to show behavior in qualitative agreement with these results in Figs. (2.8) and (2.9) and will be reported on in more detail in other publications.[21] These experiments measure the Debye Waller factors on trace amounts of Mössbauer active Sn atoms that are believed to be tetrahedrally bonded into the network. Note that the masses and force constants of the Sn are expected to be sufficiently similar to Ge and Se that $\langle x^2 \rangle$ would not be

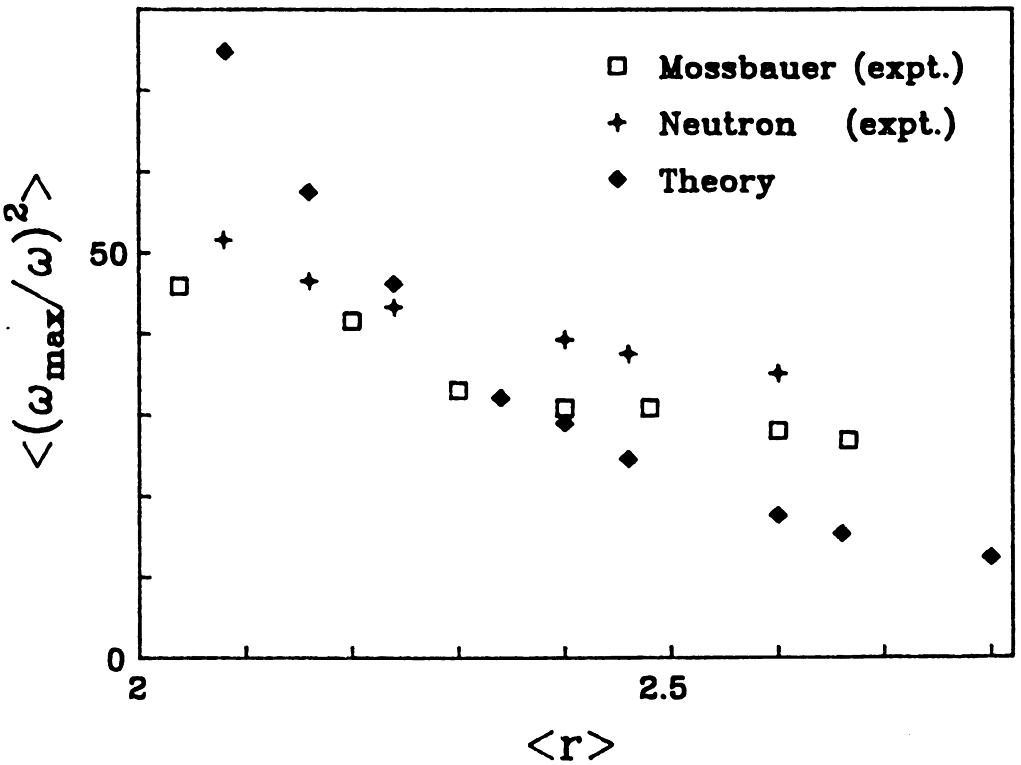

Figure 2.9: The $r = -2$ moment $\langle \omega_{max}^2/\omega^2 \rangle$ for various values of the mean coordination $\langle r \rangle$. The figure shows a comparison of results obtained from Mössbauer and inelastic neutron scattering experiments with our theoretical results.

expected to vary significantly from site to site. Our calculations involve an average over all sites. It may be that regions of the sample that are denser in floppy modes have larger $\langle x^2 \rangle$, but that remains to be seen. A more accurate analysis would also have to take into account the heavier Sn mass.

2.6 CONCLUSIONS

In this chapter, we have shown that network glasses like Ge_xSe_{1-x} undergo a washed out phase transition around a mean coordination of $\langle r \rangle = 2.4$. The elastic moduli show no anomalous behavior around this point. The low frequency "floppy" modes are quenched rapidly and disappear around this point. This behavior is reflected in the mean square displacements as measured in Mössbauer experiments. The mean square displacements increase as $\langle r \rangle$ is lowered and the rate of increase is larger for $\langle r \rangle < 2.4$. The results of experiment and a very simple theory are shown to be in reasonable agreement, although there are quantitative differences.

Bibliography

[1] W. H. Zachariasen, J. Am. Chem. Soc. 54, 3841 (1932).

[2] J. C. Phillips, Phys. Stat. Sol.(b) 101, 473 (1980); J. C. Phillips, J. Non-Cryst. Solids 34, 153 (1979); 43, 37 (1981).

[3] See for example, J. A. Erwin, A. C. Wright, J. Wong and R. N. Sinclair, J. Non Cryst. Solids 51, 57 (1982) and references therein.

[4] F. Wooten, K. Winer and D. Weaire, Phys. Rev. Lett. 54, 1392 (1985) and Wooten

[5] S. W. DeLeeuw, H. He and M. F. Thorpe, Sol. St. Comm. 56, 343 (1985); H. He, Ph. D. thesis, Michigan State University (1985).

[6] P. Vashista, R. J. Kalia, G. A. Antonio and I. Ebbsj;, Phys. Rev. Lett. 62, 1651 (1989)

[7] M. F. Thorpe, J. Non-Cryst. Solids 57, 355 (1983).

[8] H. He and M. F. Thorpe, Phys. Rev. Lett. 54, 2107 (1985).

[9] See for example H. Goldstein, Classical Mechanics, 1950 (Addison-Wesley, Cambridge).

[10] P. N. Keating, Phys. Rev. 145, 637 (1966)

[11] S. S. Yun, H. Li, R. L. Cappellctti, P. Boolchand, and R. N. Enzweiler, Phys. Rev. B39, 8702 (1989)

[12] U. Tille, G. H. Frishat and K. J. Leers, in the Procedings of the fourth International Conference on the Physics of Non-Crystalline Solids, Clausthal, West Germany (Aedermannsdorf, Switzerland: Trans. Tech. SA 1977) page 631; R. Ota, T. Yamate, N. Soga and M. Kunugi, J. Non Cryst. Solids 29, 67 (1978); J. Y. Duquesne and G. Bellessa, J. de Phys. Paris C10, Supp 2, 46, 445 (1985): ibid, 46, 449 (1985): J. Non Cryst. Solids 81, 319 (1986); K. Tanaka, Sol. St. Comm. 60, 295 (1986)

[13] B. L. Halfpap and S. M. Lindsay, Phys. Rev. Lett. 57, 847 (1986)

[14] C. Kittel, Introduction to Solid State Physics, 1971 (J. Wiley and Sons, New York) page 133

[15] F. Gompf, J. Phys. Chem. Sol., 42, 539 (1981)

[16] See for example, M. F. Thorpe and S. W. DeLeeuw, Phys. Rev. B33, 8490 (1986) and references contained therein.

[17] I. M. Lifshitz, Advances in Physics 13, 483 (1964)

[18] W. A. Kamitakahara, R. L. Cappelletti, P. Boolchand and F. Gompf, Bull. Am. Phys. Soc. 32, 812 (1987); W. A. Kamitakahara et al ., Procedings of the International Conference on Neutron Scattering, Grenoble, 1988 [Physica B (to be published)]; W. A. Kamitakahara, P. Boolchand and R. L. Cappelletti (unpublished).

[19] See for example, N. W. Ashcroft and N. D. Mermin, Solid State Physics, 1976 (Saunders College, Philadelphia).

[20] P. Boolchand and R. N. Enzweiler, Bull. Am. Phys. Soc. 32, 812 (1987); P. Boolchand (unpublished)

[21] P. Boolchand and M. F. Thorpe, to be published.

[22] M. F. Thorpe and Y. Cai in Disordered Systems and New Materials, Ed. by M. Borissov, N. Kirov and A. Vavrek (World Scientific, Singapore, 1989) p. 81

Chapter 3

RIGIDITY OF INTERCALATED LAYERED SOLIDS

This chapter is pulished in Physical Review B. Reference: Y. Cai, J. S. Chung, M. F. Thorpe and S. D. Mahanti, Phys. Rev. B**42**, 8827(1990)

3.1 INTRODUCTION

All crystalline solid solutions show a composition dependence of the average unit cell volume $\langle V \rangle$ which increases with the concentration of the largest constituent.[1] Intercalated multilayer systems such as $A_{1-x}B_xL$ are an important class of such systems. The linear variation of $\langle V \rangle$ with x is the well known Vegard's law,[2] although solid solutions often exhibit a complex nonlinear (superlinear, sublinear, sigmoidal) behavior. The value of $\langle V \rangle$ depends, at the microscopic level, on competition between the local and global energies associated with forming the solid solution. These energies depend upon the relative sizes and compressibilities of the intercalated atomic species and on the overall rigidity of the system.

There is a large variety of ternary layered intercalated compounds of the form $A_{1-x}B_xL$ [A (B) denote small (large) intercalants and L denotes layer] which can be treated theoretically in a relatively simple way, because the major expansion takes place in the direction perpendicular the layers, denoted as the c-axis. [3]-[8] However correlations between the positions of the intercalants in the multilayer case play an important role in determining the gallery structure. These correlations arise from the interactions between the intercalants mediated by the host layers.[9] For example, similar-sized intercalants prefer to stay together in the same layer to minimize the layer distortion energy. In contrast, similar-sized intercalants in adjacent galleries, tend to repel one another.[9] To a large extent, how important a role this correlation plays in the multilayer system, depends on the method of sample preparation. Rapid quenching leads to a more random distribution of intercalants, whereas annealing allows for interlayer correlations (ILC) between the intercalants to develop which may ultimately lead to segregation and/or phase separation. Even in the rapidly quenched samples a finite degree of short range correlation may be present.

In the past, several attempts[4],[9]-[11] have been made to study the nonlinear x-dependence of the c-axis expansion for a bilayer (two layers 'sandwiching' a single layer of intercalants). In this case, the most recent study,[12] referred to henceforth as **I**, rectified shortcomings in previous work by considering both the transverse rigidity of the layers, the differential size, and the compressibilities of the intercalants. The multilayer system we will discuss in this paper is a generalization of such a bilayer system and is more appropriate for a real materials. It contains all the ingredients of the previously studied bilayer model in **I** and in addition takes into account the effect of interlayer correlations between the intercalants in different layers. It is assumed that correlations between intercalants in the same layer are much less important. Such a multilayer system, with a single kind of intercalant is shown in Fig.(3.1), where the circles could represent K atoms intercalated between the C atoms in graphite. If a few larger, say Cs, atoms are present, then the layers begin to *buckle* as shown in Fig. (3.2). This buckling of the C layers increases with the concentration, and is a maximum for the 50-50 random alloy, as shown in Fig. (3.3). A similar configuration

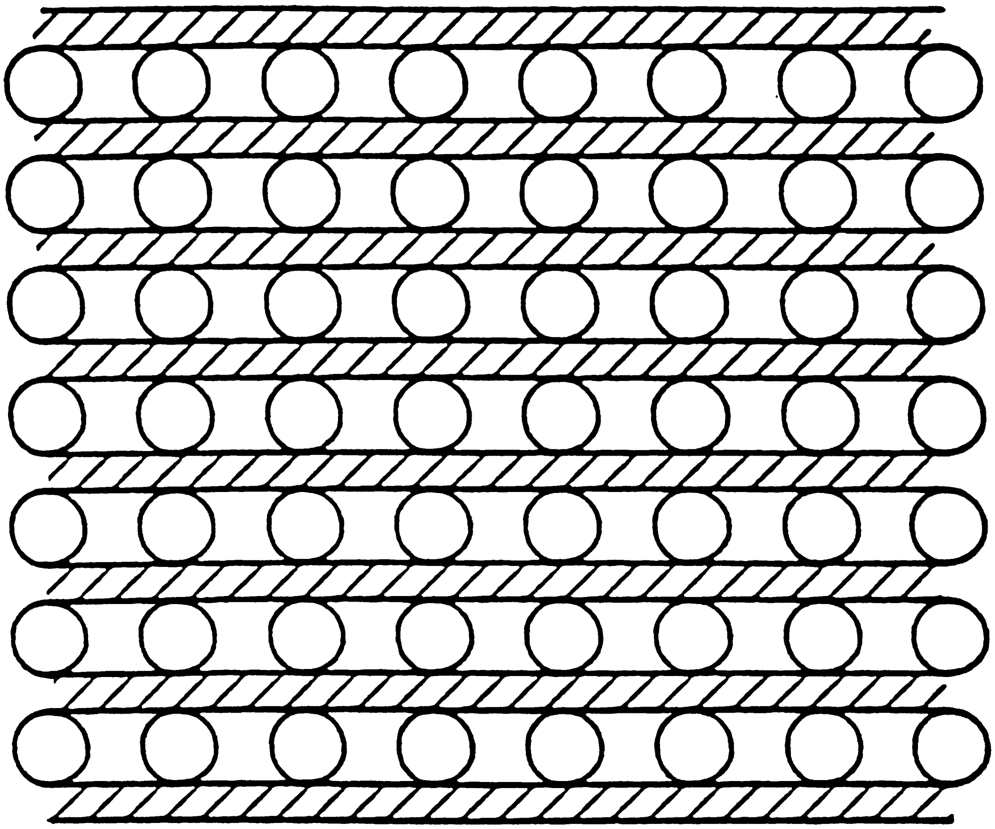

Figure 3.1: The circles represent a single species of atom, intercalated between host layers of graphite.

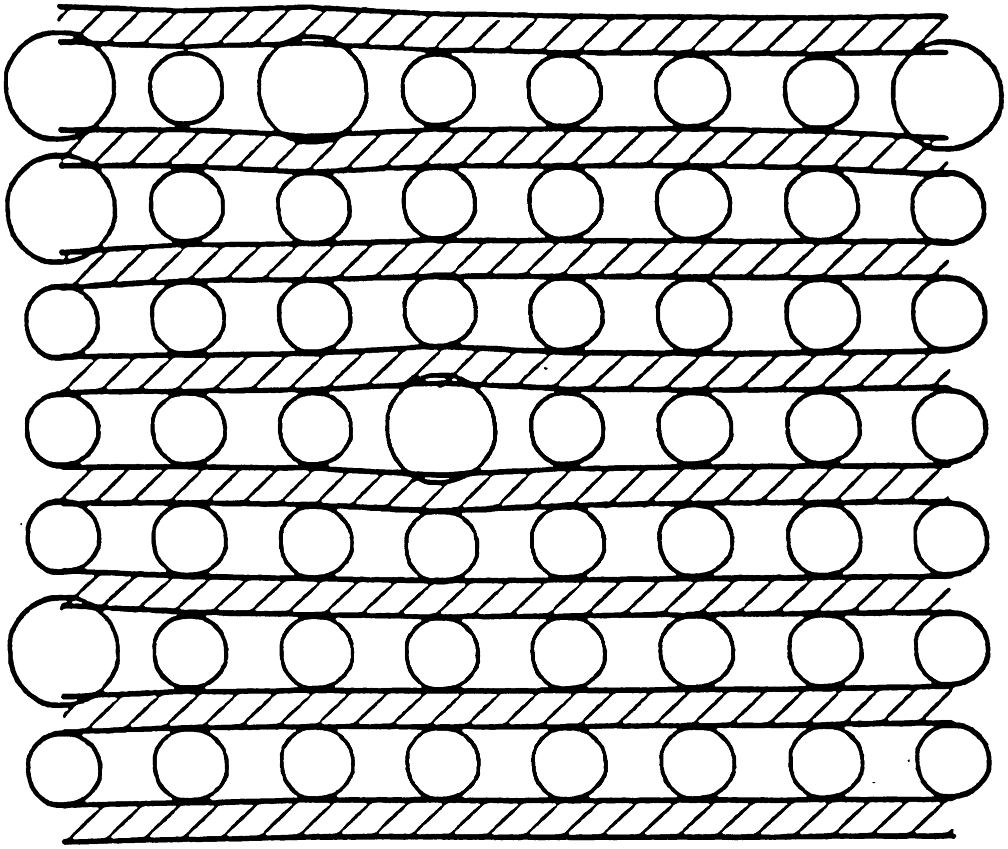

Figure 3.2: A few larger atoms are present in addition to the small atoms shown in Fig.(3.1). This drawing is produced from an actual computation for a 2d multilayer system as described in the text. Here $k = k_A = k_B = k_T$.

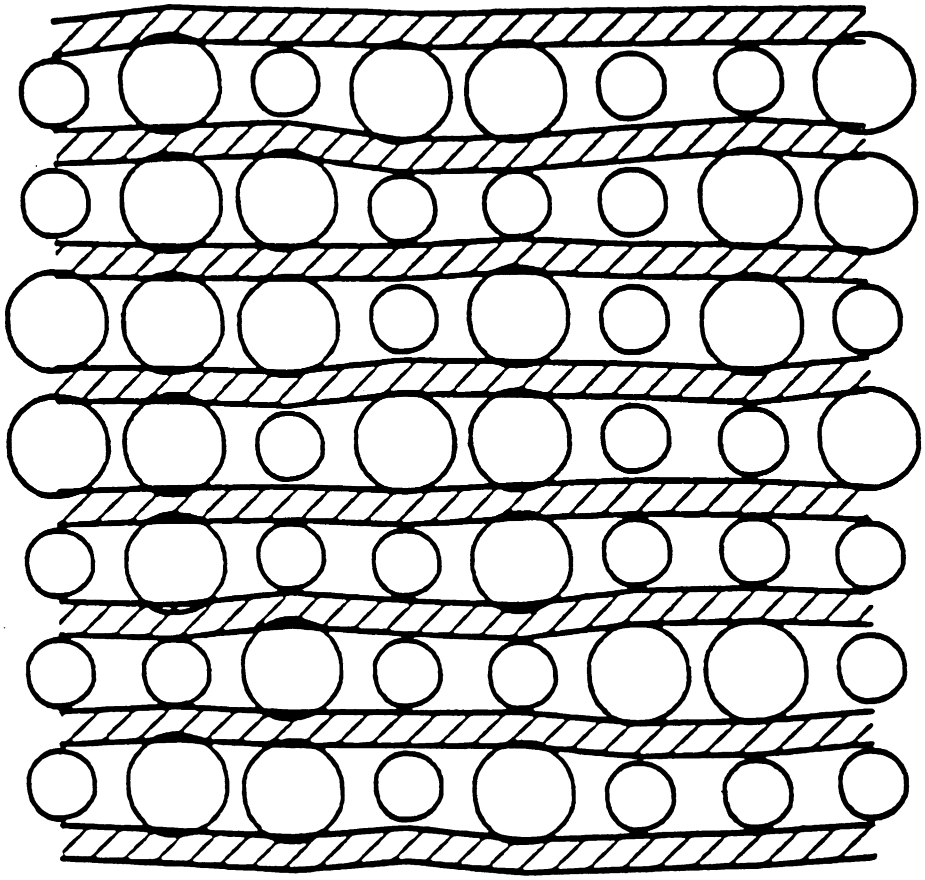

Figure 3.3: Equal number of large and small atoms are intercalated between the layers. The buckling of the layers is a maximum in this case. This drawing is produced from an actual computation for a $2d$ multilayer system as described in the text. Here $k = k_A = k_B = k_T$.

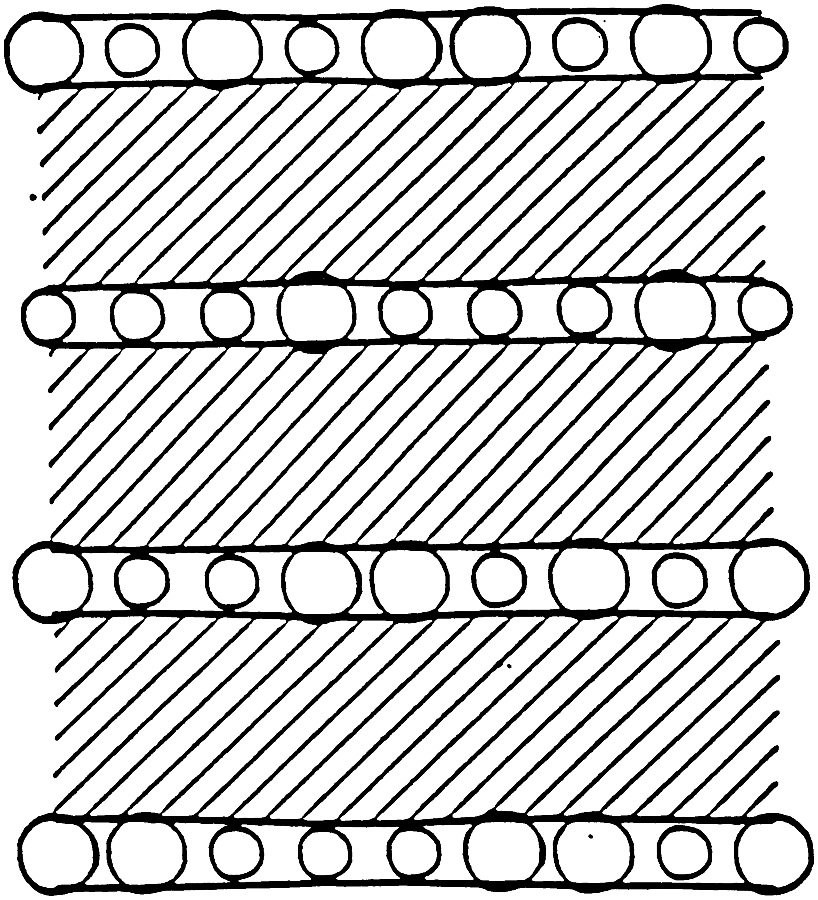

Figure 3.4: The same as Fig.(3.3), but with thicker layers, appropriate to silicates, rather than the graphite layers shown in Fig.(3.1)-(3.3). This drawing is produced from an actual computation for a $2d$ multilayer system as described in the text. Here $k = k_A = k_B = k_T$.

is shown in Fig.(3.4), but with thicker layers more appropriate to silicates (clays). Figs.(3.2)-(3.4) are drawn from the results of actual simulations and are not just sketches. A detailed discussion of the nature of this buckling and how it depends upon various physical parameters such as the compressibilities of the intercalants and the rigidity of the host galleries is given later in the chapter. Mori et.al[13] were first to point out the existence of static displacement and charge density modulation of the adjacent graphite layers when the disordered unregistered potassium layers order at low temperatures in stage-II potassium-graphite.

The arrangement of the chapter is as follows. In **sec. 3.2**, we introduce the harmonic spring model describing these systems. In **sec. 3.3**, we present the results of an exact calculation for the case $k_A = k_B$, where k_A and k_B are the local compressibilities of the intercalants. In **sec. 3.4**, we extend these results to take into account correlations perpendicular to the layers. In **sec. 3.5**, we develop an effective medium theory for the more general situation when $k_A \neq k_B$. In **sec. 3.6**, we discuss the complete probability distributions for the various gallery heights (or equivalently the interlayer distances) and the effect of ILC on these distribution functions. Comparison with computer simulation results are presented where appropriate throughout this chapter. Various exact mathematical aspects of the complete distribution functions are discussed in the appendices.

3.2 THE MODEL

Consider a layered ternary system with composition $A_{1-x}B_xL$ where L represents the host layer such as graphite, dichalcogenide or vermiculite.[10] A and B are two different types of intercalants which are assumed to occupy a set of well defined lattice sites. This assumption is reasonable for most of these intercalation compounds because of the strong interaction between the alloy (intercalants) and the substrate (host layers). For example it is known that in ternary alkali intercalation compounds

$M_{1-x}M'_xC_8$ (M, M' = K, Rb, Cs), the alkali atoms are located in registry over carbon hexagons forming a (2×2) $R0^o$ in-plane structure.[7] For a fixed (i.e. quenched) distribution of intercalants, the total energy of the system which controls the structural distortions, can be approximated by a sum of two major contributions; one associated with the interaction between the intercalants and the host and the other between host atoms themselves.

$$E = \frac{1}{2}\sum_{\mathbf{i}} k_{\mathbf{i}} \left(z_{\mathbf{i}} - z_{\mathbf{i}-\nu} - h^0_{\mathbf{i}-\nu}\right)^2 + \frac{1}{2}k_T \sum_{\langle \mathbf{i},\delta\rangle} (z_{\mathbf{i}} - z_{\mathbf{i}+\delta})^2 \tag{3.1}$$

The first term is the host-intercalant interaction approximated by a harmonic spring of strength $k_i (= k_A$ or $k_B)$ and equilibrium height $h^0_i (= h^0_A$ or $h^0_B)$. The second term is the interaction between host atoms. We only include the transverse part k_T of the layer rigidity which is sufficient for the present purpose (in general one has to also include the flexural rigidity[12],[14] and other terms). Our notation follows **I**. A diagram of the spring system associated with Eq. (3.1) is given in **I** for the bilayer case. The generalization to the multilayer case is obvious.

In Eq. (3.1), $\mathbf{i}$ is a vector labelling the position of the ith spring and $z_{\mathbf{i}}$ is the z-component of the coordinate of the ith vertex. Here a vertex refers to a point on the host layer which is directly above the ith intercalant and $h_{\mathbf{i}} = z_{\mathbf{i}} - z_{\mathbf{i}-\nu}$ is the local gallery height at the site of the ith intercalant. Only the z-component is needed because the motion of the atoms is constrained to be perpendicular to the planes in this model. The unit vector ν is along the c-axis and δ is a vector in the plane perpendicular to the c-axis connecting adjacent lattice points.

We define the average gallery heights $\langle h\rangle$, $\langle h_A\rangle$, and $\langle h_B\rangle$ as

$$\langle h\rangle = \frac{1}{N}\sum_{\mathbf{i}} h_{\mathbf{i}} \, . \tag{3.2}$$

Here N is the number of galleries. Site specific averages $\langle h_A\rangle$ and $\langle h_B\rangle$ are given by similar equations except that $\mathbf{i}$ only runs over sites occupied by either A or B. Notice that the total height of the sample is proportional to $\langle h\rangle$ as is the area or volume

$\langle V\rangle$ of the sample, as there are no length changes parallel to the planes. Thus all definitions of length, both microscopic and macroscopic, are equivalent.

One can define a dimensionless height $d_{\rm i}$ through the relation:

$$h_{\rm i} = h_A^0 + d_{\rm i}(h_B^0 - h_A^0)\,, \tag{3.3}$$

where $d_{\rm i} = 0$ or 1, for A or B respectively when there is no distortion. The average gallery height $\langle d\rangle$ is given by:

$$\langle d\rangle = \frac{1}{N}\sum_{\rm i} d_{\rm i}\,, \tag{3.4}$$

with similar definitions for $\langle d_A\rangle$ and $\langle d_B\rangle$. Note that by definition:

$$\langle d\rangle = (1-x)\langle d_A\rangle + x\langle d_B\rangle. \tag{3.5}$$

3.3 ANALYTIC SOLUTION

When the local compressibilities are equal, we have $k_A = k_B = k$, and the energy in Eq. (3.1) becomes

$$E = \frac{1}{2}k\sum_{\rm i}\left(z_{\rm i} - z_{{\rm i}-\nu} - h^0_{{\rm i}-\nu}\right)^2 + \frac{1}{2}k_T\sum_{\langle {\rm i},\delta\rangle}\left(z_{\rm i} - z_{{\rm i}+\delta}\right)^2 \tag{3.6}$$

Unlike the treatment for the bilayer system in **I**, it has not been possible to express the energy functional (6) as proportional to $(h_A^0 - h_B^0)^2$ at the outset, although this result is obtained later on. It is quite difficult to deal with the above form for E, because the coordinate z is cumulative. We therefore introduce another variable $u_{\rm i}$ which is defined as:

$$u_{\rm i} = z_{\rm i} - h^*\,({\rm i}\cdot\nu)\,, \tag{3.7}$$

where the parameter h^* is an average length for each spring and is determined later by minimizing the distortion energy; $u_{\rm i}$ can be interpreted as the displacement of the *i*th vertex from the average regular lattice. In terms of this new variable, the energy is given by

$$E \;=\; \frac{1}{2}k\sum_{\rm i}\left(u_{\rm i} - u_{{\rm i}-\nu} + h^* - h^0_{{\rm i}-\nu}\right)^2 + \frac{1}{2}k_T\sum_{\langle {\rm i},\delta\rangle}\left(u_{\rm i} - u_{{\rm i}+\delta}\right)^2.$$

$$= \quad E_k + E_{k_T} \, . \tag{3.8}$$

where E_k and E_{k_T} represent the first and second terms above.

For a fixed h^*, the equilibrium conditions are $\partial E/\partial z_{\mathrm{i}} = 0$ or $\partial E/\partial u_{\mathrm{i}} = 0$, which lead to:

$$k\left(2u_{\mathrm{i}} - u_{\mathrm{i}-\nu} - u_{\mathrm{i}+\nu}\right) + k_T \sum_{\delta} \left(u_{\mathrm{i}} - u_{\mathrm{i}+\delta}\right) = k\left(h^0_{\mathrm{i}-\nu} - h^0_{\mathrm{i}}\right) \tag{3.9}$$

Eq. (3.9) can be rewritten in matrix form as:

$$\mathbf{M}\mathbf{U} = \mathbf{\Phi}, \tag{3.10}$$

where **U** is the displacement vector of the system and the matrix **M** is formed from the coefficients. The random vector $\mathbf{\Phi}$ contains all the disorder. Since **M** is a nonrandom matrix, we can solve the problem analytically. (Note that this is possible only for $k_A = k_B$.) A similar form was given in **I** [see Eq. (16)].

Denoting $\mathbf{M}^{-1}$ as the inverse of **M**, we obtain:

$$u_{\mathrm{i}} = k \sum_{\mathrm{j}} (\mathbf{M}^{-1})_{\mathrm{ij}} \left(h^0_{\mathrm{j}-\nu} - h^0_{\mathrm{j}}\right) \, . \tag{3.11}$$

In the expression for the energy E in Eq. (3.8), only the first term contains h^*. Substituting for u_{i} from Eq. (3.11) into E_k, we obtain

$$\begin{aligned} E_k \quad = \quad & \frac{k}{2} \sum_{\mathrm{i}} \{(h^*)^2 - 2h^* h^0_{\mathrm{i}-\nu} + (h^0_{\mathrm{i}-\nu})^2 \\ & +2 \sum_{\mathrm{j}} \left[(\mathbf{M}^{-1})_{\mathrm{ij}} - (\mathbf{M}^{-1})_{\mathrm{i}-\nu\mathrm{j}}\right] (h^0_{\mathrm{j}-\nu} - h^0_{\mathrm{j}})(h^* - h^0_{\mathrm{i}-\nu}) \\ & +k^2 \sum_{\mathrm{jl}} \left[(\mathbf{M}^{-1})_{\mathrm{ij}} - (\mathbf{M}^{-1})_{\mathrm{i}-\nu\mathrm{j}}\right] \left[(\mathbf{M}^{-1})_{\mathrm{il}} - (\mathbf{M}^{-1})_{\mathrm{i}-\nu\mathrm{l}}\right] (h^0_{\mathrm{j}-\nu} - h^0_{\mathrm{j}})(h^0_{\mathrm{l}-\nu} - h^0_{\mathrm{l}})\} \, . \end{aligned} \tag{3.12}$$

We introduce a new variable σ_{i} replacing h^0_{i} such that

$$h^0_{\mathrm{i}} = a\sigma_{\mathrm{i}} + b = \begin{cases} h^0_A, & \text{if } \sigma_{\mathrm{i}} = 1 \\ h^0_B, & \text{if } \sigma_{\mathrm{i}} = -1. \end{cases} \tag{3.13}$$

It is very convenient to use this language, borrowed from magnetism [15] to describe the locations of the intercalants. The two parameters a and b are:

$$a = \frac{(h_A^0 - h_B^0)}{2} \,, \tag{3.14}$$

and

$$b = \frac{(h_A^0 + h_B^0)}{2} \,. \tag{3.15}$$

Replacing h_{i}^0 in terms of σ_{i} in the expression for E_k and performing the ensemble average, we find

$$\begin{aligned} E_k \; = \tfrac{1}{2}\textstyle\sum_{\mathrm{i}}\{ \quad & (h^*)^2 - 2h^*\langle h\rangle + \langle h^2\rangle \\ & -2k\sum_{\mathrm{j}} \left[(\mathbf{M}^{-1})_{\mathrm{ij}} - (\mathbf{M}^{-1})_{\mathrm{i}-\nu\mathrm{j}}\right] \cdot a^2(\langle\sigma_{\mathrm{j}-\nu}\sigma_{\mathrm{i}-\nu}\rangle - \langle\sigma_{\mathrm{j}}\sigma_{\mathrm{i}-\nu}\rangle) \\ & +k^2\sum_{\mathrm{jl}} \left[(\mathbf{M}^{-1})_{\mathrm{ij}} - (\mathbf{M}^{-1})_{\mathrm{i}-\nu\mathrm{j}}\right] \left[(\mathbf{M}^{-1})_{\mathrm{il}} - (\mathbf{M}^{-1})_{\mathrm{i}-\nu\mathrm{l}}\right] \\ & \cdot a^2(\langle\sigma_{\mathrm{j}-\nu}\sigma_{\mathrm{l}-\nu}\rangle + \langle\sigma_{\mathrm{j}}\sigma_{\mathrm{l}}\rangle - \langle\sigma_{\mathrm{j}-\nu}\sigma_{\mathrm{l}}\rangle - \langle\sigma_{\mathrm{j}}\sigma_{\mathrm{l}-\nu}\rangle)\} \; . \end{aligned} \tag{3.16}$$

Minimization of the energy with respect to h^*, i.e.

$$\frac{\partial E}{\partial h^*} = \frac{\partial E_k}{\partial h^*} = 0 \tag{3.17}$$

gives Vegard's law:

$$h^* = \langle h_{\mathrm{i}}^0\rangle = h_A^0(1-x) + h_B^0 x = a(1-2x) + b \,, \tag{3.18}$$

where we have made use of the relation $\langle\sigma_{\mathrm{i}}\rangle = 1 - 2x$.

The expression for the energy contains various two spin correlation functions. For the case of a random distribution of intercalants, the two spins are uncorrelated (corresponding to two intercalants either in the same gallery, or in adjacent galleries being uncorrelated) and we have

$$\langle\sigma_{\mathrm{i}}\sigma_{\mathrm{j}}\rangle = (1-2x)^2 + 4x(1-x)\delta_{\mathrm{ij}} \,. \tag{3.19}$$

After some mathematical manipulation, we obtain simple expressions for the dimensionless energy per site $\varepsilon = E/(4Na^2k)$, and also for the dimensionless lengths $\langle d_A \rangle$, $\langle d_B \rangle$ and the fluctuations:

$$\varepsilon = \frac{1}{2}x(1-x)(1-W(k)) \ , \tag{3.20}$$

$$\langle d_A \rangle = x\,(1-W(k)) \ , \tag{3.21}$$

$$\langle d_B \rangle = 1-(1-x)(1-W(k)) \ , \tag{3.22}$$

$$\begin{aligned} \langle d_A^2 \rangle - \langle d_A \rangle^2 \quad &= x(1-x)\left(W_1(k) - W(k)^2\right) \\ &= \langle d_B^2 \rangle - \langle d_B \rangle^2 \ . \end{aligned} \tag{3.23}$$

These equations are identical to those for the bilayer case with functions $W(k)$ and $W_1(k)$ being similar to quantities used in **I**, but now appropriately modified for the multilayer case. As in **I**, we refer to all quantities like $W(k)$ and $W_1(k)$, as generalised Watson integrals.[12] These Watson integrals reflect the influence of the lattice structure on the various quantities calculated. They are given respectively by

$$\begin{aligned} W(k) = \quad & 2(\mathrm{M}^{-1})_{\mathrm{ii}} - (\mathrm{M}^{-1})_{\mathrm{i}+\nu\,\mathrm{i}} - (\mathrm{M}^{-1})_{\mathrm{i}-\nu\,\mathrm{i}} \\ = \quad & \frac{1}{N}\sum_{\mathbf{q}} \frac{2k[1-\cos(\mathbf{q}\cdot\nu)]}{\lambda_{\mathbf{q}}} \ , \end{aligned} \tag{3.24}$$

and

$$\begin{aligned} W_1(k) = \quad & \sum_{\mathrm{j}}[2(\mathrm{M}^{-1})_{\mathrm{ij}} - (\mathrm{M}^{-1})_{\mathrm{i}+\nu\,\mathrm{j}} - (\mathrm{M}^{-1})_{\mathrm{i}-\nu\,\mathrm{j}}]^2 \\ = \quad & \frac{1}{N}\sum_{\mathbf{q}} \frac{4k^2[1-\cos(\mathbf{q}\cdot\nu)]^2}{\lambda_{\mathbf{q}}^2} \ , \end{aligned} \tag{3.25}$$

where the dispersion relation for the pure system is given by

$$\lambda_{\mathbf{q}} = 2k[1-\cos(\mathbf{q}\cdot\nu)] + k_T z(1-\gamma_{\mathbf{q}}) \tag{3.26}$$

and

$$\gamma_{\mathbf{q}} = \frac{1}{z}\sum_{\delta} e^{i\mathbf{q}\cdot\delta}. \tag{3.27}$$

In Eq. (3.27), z is the coordination number in the plane. Note that we have made use of the expanded form of $(\mathbf{M}^{-1})_{\mathbf{ij}}$:

$$(\mathbf{M}^{-1})_{\mathbf{ij}} = \frac{1}{N}\sum_{\mathbf{q}} \frac{e^{-i\mathbf{q}\cdot\mathbf{r}_{\mathbf{ij}}}}{\lambda_{\mathbf{q}}} \tag{3.28}$$

From Eqs. (3.5), (3.21) and (3.22), we find that the average normalized interlayer spacing $\langle d\rangle = x$ and therefore we see that Vegard's law is obeyed. It is remarkable that Vegard's law is independent of the number of layers and the only way one can see the effect of multilayers is in the site-selective gallery heights $\langle d_A\rangle$ and $\langle d_B\rangle$ and gallery height fluctuations through the generalized Watson integrals. In the bilayer case the factor $[1 - \cos(\mathbf{q}\cdot\nu)]$ in Eqs. (3.24) - (3.26) is replaced by one and the q_z summation also gives unity. We have found that for a given strength of layer rigidity (k_T), W(k) for the multilayer is smaller than for the bilayer indicating increased stiffness. The exact results given in Eqs. (3.20)-(3.23) are shown in Fig. (3.5)-(3.7) in the center panels marked R (for Random). A discussion of these results is given in the next section in conjunction with the results for the correlated case. The diagrams for Figs. (3.2)-(3.4) (and also for Figs. (3.8) and (3.9), were constructed from computer simulations and show a small piece of a much larger sample. The intercalant atoms are centered midway between the lattice positions $\mathbf{i}$ and $\mathbf{i}+\nu$. The thickness of the host layers, shown as pairs of parallel lines, is chosen to roughly correspond to graphite in Figs. (3.1)-(3.3) (and Figs. (3.8) and (3.9)), while the thicker layers in Fig. (3.4) correspond to the silicate layers in clays. The intercalant atoms have fixed radii, one for the A species and another for the B species. The variation in gallery heights in exaggerated somewhat in these figures for easier visualization. This is not a serious deficiency as the heights all scale with $(h_B^0 - h_A^0)$.

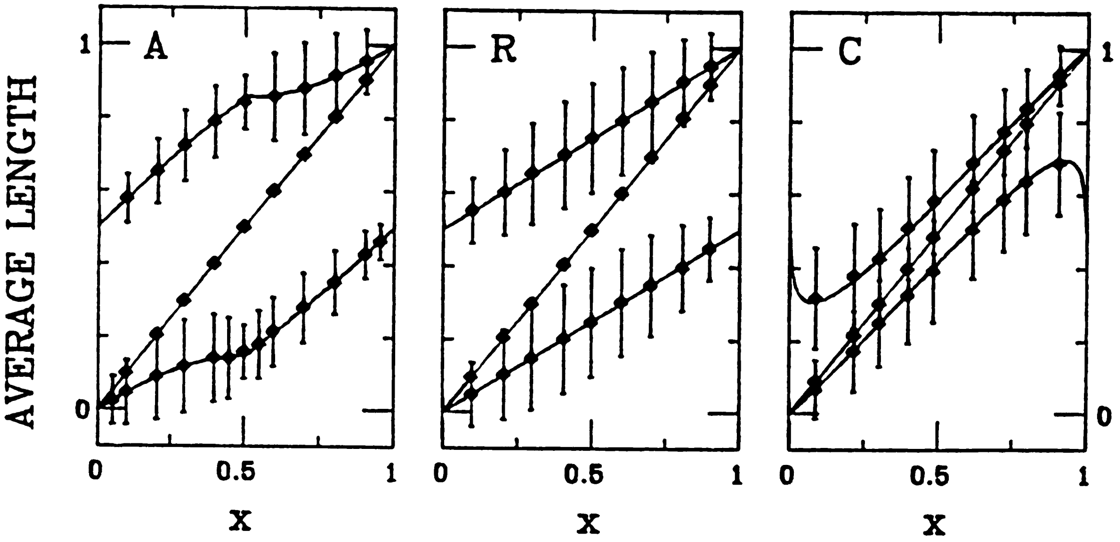

Figure 3.5: Showing the average heights of the A, B galleries $\langle d_A \rangle$, $\langle d_B \rangle$ and the overall average height $\langle d \rangle$, in dimensionless units. The symbols are from computer simulations in a $2d$ multilayer system and the solid lines are exact results. The vertical lines represent the full width at half the height for the partial length distribution functions, and are *not* error bars.The symbols A, R, and C stand for Anticlustering, Random and Clustering respectively. Here $k = k_A = k_B = k_T$.

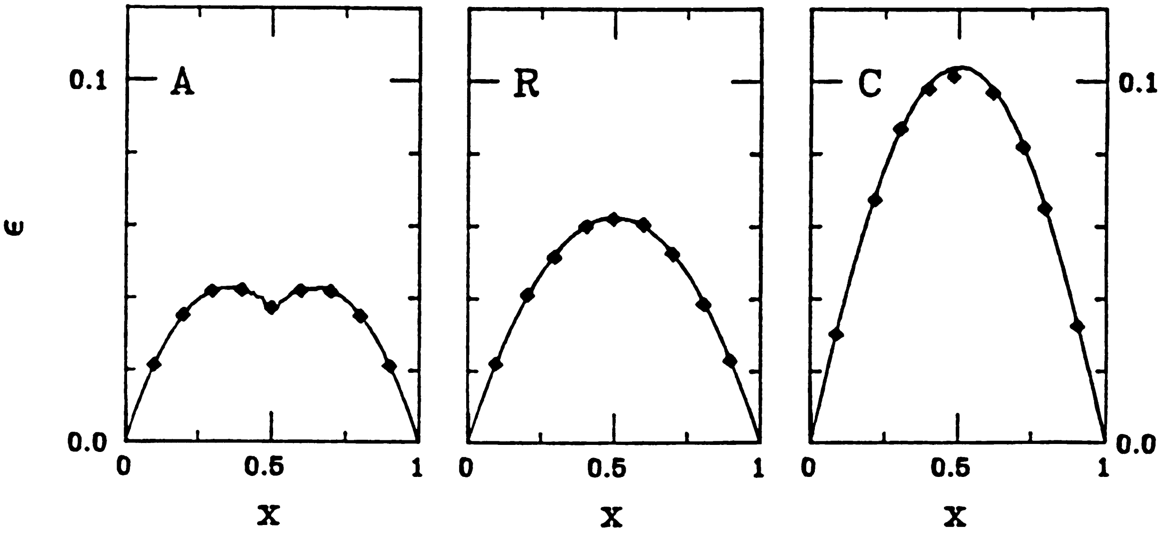

Figure 3.6: The strain energy ϵ, is shown for the $2d$ multilayer case. The symbols are from computer simulations and the solid lines are exact results. The symbols A, R, C stand for Anticlustering, Random and Clustering respectively. Here $k = k_A = k_B = k_T$.

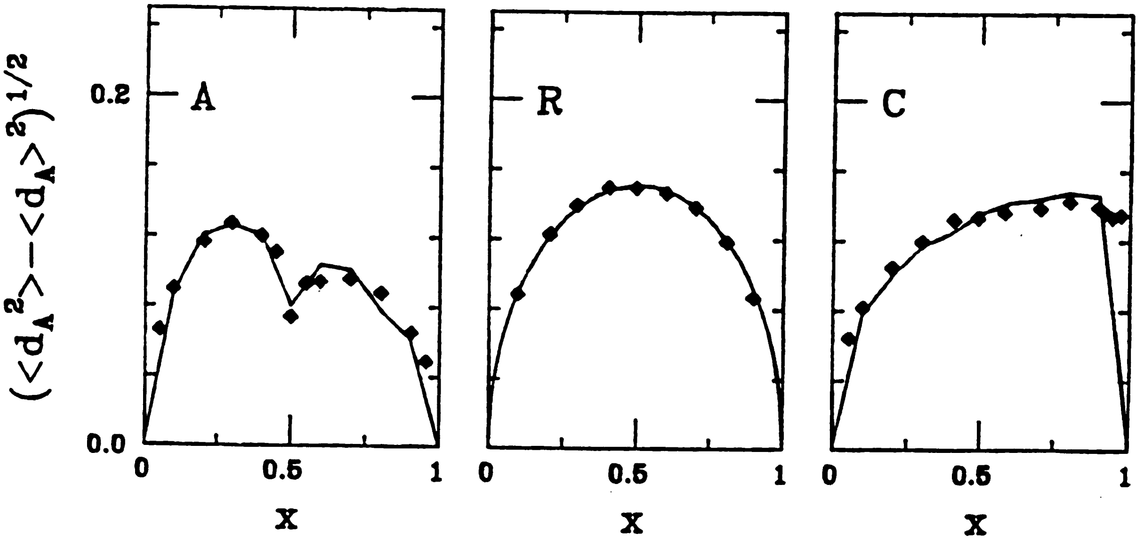

Figure 3.7: The width, $\sqrt{\langle d_A^2\rangle - \langle d_A\rangle^2}$, of the distribution function for the A gallery height for the $2d$ multilayer case. The symbols are from computer simulations and the solid lines are exact results. The symbols A, R, C stand for Anticlustering, Random and Clustering respectively. Here $k = k_A = k_B = k_T$.

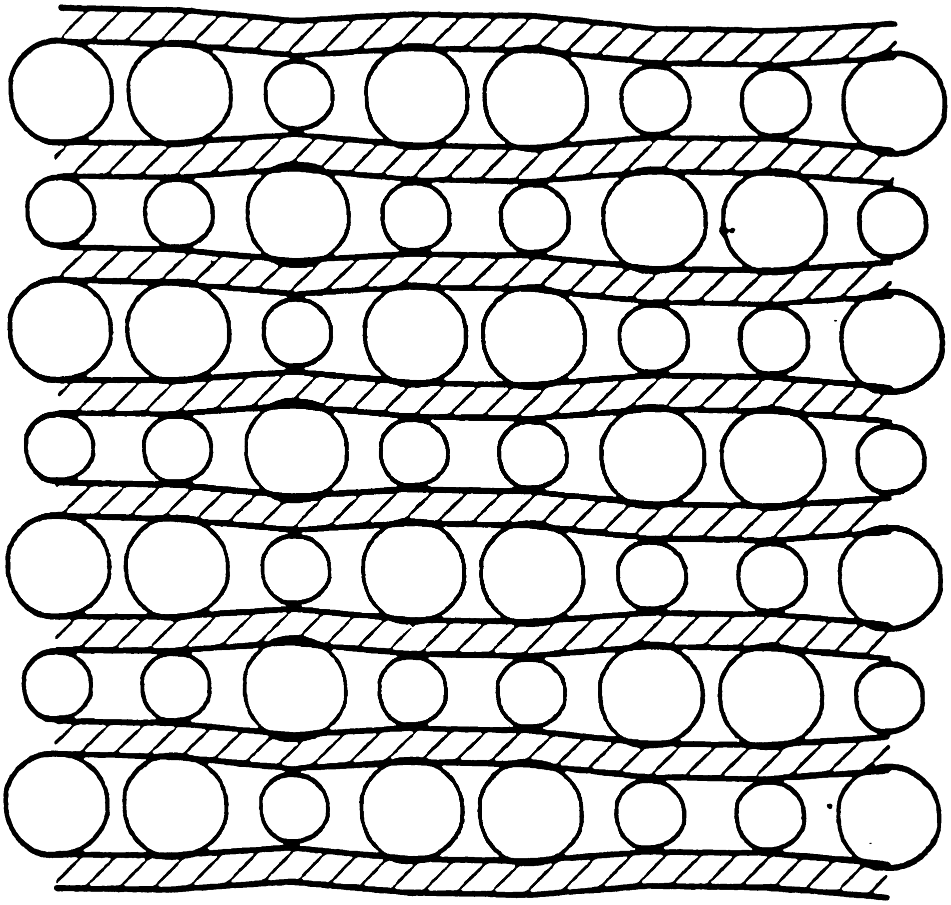

Figure 3.8: Equal number of large and small atoms are intercalated between the layers with Anticlustering perpendicular to the layers. The drawing is produced from a actual computation for a $2d$ multilayer system as described in the text. Here $k = k_A = k_B = k_T$.

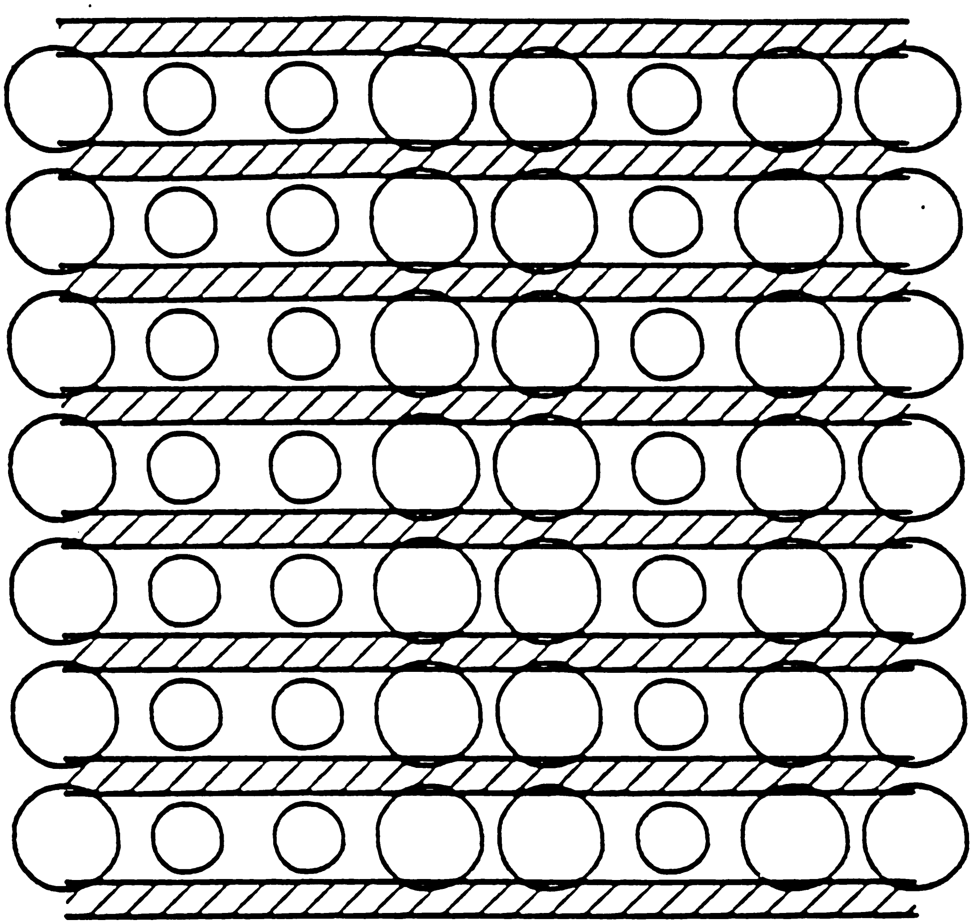

Figure 3.9: Equal number of large and small atoms are intercalated between the layers with Clustering perpendicular to the layers. The drawing is produced from a actual computation for a $2d$ multilayer system as described in the text. Here $k = k_A = k_B = k_T$.

3.4 CORRELATED CASE

When there is finite correlation between intercalants occupying different galleries we have to know precisely how these are correlated before we can obtain the intergallery structure by minimizing the energy for a given configuration of the intercalants. For the sake of illustration we show in Fig.(3.8) a situation where the larger intercalants in adjacent galleries tend to avoid each other in order to reduce the build up of local strain energy. In our formulation of the problem the correlation between the intercalants appears through the Ising model spin-spin correlation functions which must be known in order to describe the positions of the intercalants in the galleries.. For simplicity we use a $1d$ Ising model [15] to allow for correlation along the $z-$axis only, i.e., include only *interlayer* correlation and neglect *intralayer* correlation. It is believed that this corresponds to the actual situation in many cases. This is fortunate as this case can be handled in a rather straightforward way.

The interlayer correlation function can be obtained from a $1d$ Ising spin model [15] with the Hamiltonian given by

$$\mathcal{H} = -J\sum_i \sigma_i\sigma_{i+1} - h\sum_i \sigma_i \, . \tag{3.29}$$

where the magnetic field h controls the value of $\langle\sigma_i\rangle$. Using the standard transfer matrix method,[15] we have

$$\langle\sigma_i\sigma_j\rangle - \langle\sigma_i\rangle\langle\sigma_j\rangle = 4x(1-x)\Lambda^{|i-j|} \, , \tag{3.30}$$

where $\langle\sigma_i\rangle = 1-2x$ and is independent of i. In Eq. (3.30), we have used

$$\Lambda = \frac{\sqrt{4x(1-x)+(1-2x)^2P^2}-P}{\sqrt{4x(1-x)+(1-2x)^2P^2}+P} \, , \tag{3.31}$$

where

$$P = e^{-2J/k_BT} \tag{3.32}$$

and J is the nearest neighbor interaction, k_B the Boltzmann constant, and T the temperature. The degree of interlayer correlation is controlled by the parameter

P. When $J = 0$, i.e. in the random distribution limit, $P = 1$ and $\Lambda = 0$. For ferromagnetic interactions $J > 0$ and $P < 1$, which implies that two similar ions (large-large and small-small) prefer to stay together. Usually in intercalated systems, similar ions in adjacent layers would be expected to repel each other, because of steric effects, which implies an antiferromagnetic interaction, i.e. $J < 0$ and $P > 1$. Note that in the extreme clustering (ferromagnetic) limit, $P \rightarrow 0$ and $\Lambda \rightarrow 1$, while in the extreme anticlustering (antiferromagnetic) limit, $P \rightarrow \infty$ and $\Lambda \rightarrow -x/(1-x)$.

For the fluctuations in the heights for the galleries containing the A and B intercalants, one needs three-spin correlation functions, which can also be calculated using transfer matrix techniques.[15] The result is

$$\langle\sigma_i\sigma_j\sigma_k\rangle - \langle\sigma_i\rangle\langle\sigma_j\rangle\langle\sigma_k\rangle$$

$$= 4x(1-x)(1-2x)\left(\Lambda^{|i-j|} + \Lambda^{|j-k|} + \Lambda^{|k-i|} - 2\Lambda^{\frac{1}{2}(|i-j|+|j-k|+|k-i|)}\right) . \quad (3.33)$$

which can be rewritten compactly as

$$\langle\sigma_i\sigma_j\sigma_k\rangle = \langle\sigma\rangle\left(\langle\sigma_i\sigma_j\rangle + \langle\sigma_j\sigma_k\rangle - \langle\sigma_k\sigma_i\rangle\right) , \quad (3.34)$$

for $i \leq j \leq k$. These results, Eqs. (3.30) and (3.33), can be utilized in a multidimensional network with correlations only in one dimension as follows; the two and three spin correlation functions are given by Eqs. (3.30) and (3.33) if all spins are in the same column, and are zero otherwise.

In the correlated case we also have arrived at the same simple forms for $\langle d_A\rangle$, $\langle d_B\rangle$, and ε, as in Eqs. (3.20)-(3.22), except that the Watson integral $W(k)$ is replaced by $W_C(k)$ where

$$W_C(k) = \frac{1}{N}\sum_{\mathbf{q}} \frac{2k[1-\cos(\mathbf{q}\cdot\nu)]}{\lambda_{\mathbf{q}}} F_C(\Lambda, \mathbf{q}) \quad (3.35)$$

and

$$F_C(\Lambda, \mathbf{q}) = \frac{1-\Lambda^2}{1+\Lambda^2-2\Lambda\cos(\mathbf{q}\cdot\nu)} \quad (3.36)$$

There are two points worth mentioning here. First, just as we obtained Vegard's law behavior in the random case, we continue to get a linear relationship between $\langle d \rangle$ and x even when there is finite ILC. **This shows that the Vegard's law is independent of the strength of the ILC as long as $k_A = k_B$.** This is not surprising as Vegard's law is obeyed in the most extreme case of ILC, i.e. complete phase separation. Second, the simple forms of the strain energy and other physical quantities imply that the effects of correlation can be incorporated into the generalized Watson integral. This is significant because it provides a way to construct an Effective Medium Theory (EMT) in the presence of the ILC. This point will be clarified after we discuss the important role played by the Watson integrals in EMT in **sec. 3.5**.

The fluctuations in the A and B heights are more difficult to obtain because 3-spin correlation functions are involved. This requires the introduction of another integral besides modifying W_1 (see Eq. (3.25)) to W_{C1}. For example,

$$\langle d_A^2 \rangle - \langle d_A \rangle^2 = x(1-x)\left(W_{C1} - W_{C2}\right) + x^2 \left(W_{C2} - W_C^2\right) , \qquad (3.37)$$

where

$$W_{C1}(k) = \frac{1}{N} \sum_{\mathbf{q}} \frac{4k^2[1-\cos(\mathbf{q}\cdot\nu)]^2}{\lambda_{\mathbf{q}}^2} F_C(\Lambda, \mathbf{q}) \qquad (3.38)$$

and we need in addition

$$\begin{aligned} W_{C2}(k) &= \frac{1}{N^3} \sum_{\mathbf{q},\mathbf{q}'} \frac{k^2[2-2\cos(\mathbf{q}\cdot\nu)][2-2\cos(\mathbf{q}'\cdot\nu)]}{\lambda_{\mathbf{q}}\lambda_{\mathbf{q}'}} \sum_{\mathbf{i},\mathbf{j},\mathbf{l}} e^{i\mathbf{q}\cdot\mathbf{r}_{\mathbf{ij}}} e^{i\mathbf{q}'\cdot\mathbf{r}_{\mathbf{il}}} \Lambda^{\frac{|\mathbf{i}-\mathbf{j}|}{2}} \Lambda^{\frac{|\mathbf{i}-\mathbf{l}|}{2}} \Lambda^{\frac{|\mathbf{l}-\mathbf{j}|}{2}} \\ &= \frac{1}{N^2} \sum_{\mathbf{q},\mathbf{q}'} \frac{k^2[2-2\cos(\mathbf{q}\cdot\nu)][2-2\cos(\mathbf{q}'\cdot\nu)]}{\lambda_{\mathbf{q}}\lambda_{\mathbf{q}'}} F_{C2}(\mathbf{q},\mathbf{q}',\Lambda) . \qquad (3.39) \end{aligned}$$

where

$$F_{C2}(\mathbf{q},\mathbf{q}',\Lambda) = \frac{uv+\Lambda}{uv-\Lambda} + \Lambda\left(\frac{1+uv}{1-uv} + \frac{uv+\Lambda}{uv-\Lambda}\right) \cdot \left(\frac{1}{u-\Lambda} + \frac{1}{v-\Lambda}\right) \qquad (3.40)$$

in which $u = e^{i\mathbf{q}\cdot\nu}$ and $v = e^{i\mathbf{q}'\cdot\nu}$. In the random distribution limit $\Lambda = 0$, and all these results reduce to those of **sec. 3.3**.

We have carried out a series of computer simulation for $2d$ multilayer systems where $z = 2$. The results are shown in Figs. (3.5)-(3.7). Fig. (3.5) shows the dimensionless heights $\langle d\rangle$, $\langle d_A\rangle$, and $\langle d_B\rangle$ versus the composition x, for different amounts of correlation, ranging from clustering through random to anticlustering. In Figs. (3.5)-(3.7), the symbols A,R and C, stand for Anticlustering (or antiferromagnetic), Random and Clustering (or ferromagnetic) respectively . The corresponding parameters P [see Eq. (3.32)] are $P = 500$, $P = 1$ and $P = 0.1$ respectively. In contrast to the average interlayer separation the $\langle d\rangle$, $\langle d_A\rangle$ and $\langle d_B\rangle$ show nonlinear x-dependence particularly for the clustering situation when the concentration of one of the intercalants is very small. Our theoretical study of the multilayer system clearly points out the need for probing the x-dependence of site-selective local gallery heights in layered intercalation compounds, which could be done using EXAFS.[16] Fig. (3.6) shows the strain or deformation energy as function of composition x. This energy is greatest for the case of clustering as the packing is most difficult to achieve in that case because the height mismatch between adjacent columns would tend to accumulate . This would lead to a very great strain energy and so in response to this situation, the layers become quite flat as shown in Fig. (3.9). Indeed as P becomes infinite, the layers are absolutely flat and all the strain energy is in the first term, involving E_k in Eq. (3.8). In the other limit of anticlustering, the strain energy is reduced as the packing becomes more *comfortable* as shown in Fig. (3.8). Here the strain energy is shared between the two terms in Eq. (3.8). Note that the strain energy is particularly favorable when x = 1/2, which is the case illustrated in Fig. (3.8), when there is a narrowing cusp in the energy as seen in Fig. (3.6). The width of the distribution also shows a cusp in this case as shown in Fig. (3.7).

3.5 EFFECTIVE MEDIUM THEORY

3.5.1 Random Intercalation

When the two intercalants have different compressibilities $k_A = k_B$, we cannot obtain an exact solution. In this case one has to develop approximate methods such as

effective medium theory. The effective medium theory for the random multilayer case is a straightforward generalization of **I** which follows the basic ideas of Feng, Thorpe and Garboczi.[17] The effective medium has uniform spring constants k, k_T and spring length h_e. The effect of the environment on a single intercalant is contained within an effective spring constant k_e. When a force F is applied locally to expand the gallery height, the resulting displacement u_0 equals the force divided by the effective spring constant $k_e \equiv k/W(k)$.

$$u_0 = \frac{F}{k_e} = W(k)\frac{F}{k} \, . \tag{3.41}$$

The function $W(k)$ is the same Watson integral we have discussed in the previous section and in **I**. It has a clear physical meaning here, i.e. the rest of the lattice is characterized by another spring with compressibility $k'_e = k_e - k$ and natural length h_e, and the effect of this environment is contained in the Watson integral.

Let's get back to the construction of the EMT. Replace one of the springs $\{k, h_e\}$ in the effective medium by $\{k^0_\alpha, h^0_\alpha\}$ ($\alpha = A$ or B). The deformation energy then takes the form

$$\varepsilon = \frac{1}{2}k_\alpha(h - h^0_\alpha)^2 + \frac{1}{2}k'_e(h - h_e)^2 \, , \tag{3.42}$$

where the first term is from the deformation of the α-spring when its length is changed from h^0_α to h, and the second term is from the the effective medium representing the rest of the material. By minimizing ε we obtain the local equilibrium length $h = h_\alpha$, where

$$h_\alpha = \frac{(k'_e h_e + k_\alpha h^0_\alpha)}{(k'_e + k_\alpha)} \, . \tag{3.43}$$

Substituting this back in Eq. (3.42) gives the energy for a single α-impurity in the effective medium,

$$\varepsilon_\alpha = \frac{(h_e - h^0_\alpha)^2 k'_e k_\alpha}{2(k'_e + k_\alpha)} . \tag{3.44}$$

There are two different types of impurity springs and the total deformation energy is the sum of two types of deformation energy weighted with probabilities p_α. Here

$p_A = 1 - x$ and $p_B = x$. Therefore, we have

$$\varepsilon = \frac{1}{2}\sum_{\alpha} p_\alpha \frac{(h_e - h_\alpha^0)^2 k_e' k_\alpha}{(k_e' + k_\alpha)} . \tag{3.45}$$

Minimizing ε with respect to h_e determines h_e, i.e.

$$h_e = \frac{\sum_\alpha p_\alpha h_\alpha^0 k_\alpha/(k_e' + k_\alpha)}{\sum_\alpha p_\alpha k_\alpha/(k_e' + k_\alpha)} . \tag{3.46}$$

We need another equation to obtain the two unknown quantities, k and h_e and use the following argument. Apply a force F at the single impurity site. This produces a displacement $F/(k_e' + k_\alpha)$ which when averaged over all sites is set equal to F/k_e to give the self consistency condition,

$$\sum_{\alpha} \frac{p_\alpha}{k_e' + k_\alpha} = \frac{1}{k_e} . \tag{3.47}$$

Eqs. (3.43) and (3.47) solve the problem. The results are:

$$\langle d \rangle = x + x(1-x)F_d \tag{3.48}$$

$$\langle d_A \rangle = \frac{x k_e k_e' k_B}{k(k_e' + k_A)(k_e' + k_B)} \tag{3.49}$$

$$\langle d_B \rangle = 1 - \frac{(1-x) k_e k_e' k_A}{k(k_e' + k_A)(k_e' + k_B)} \tag{3.50}$$

$$\varepsilon = \frac{1}{2}\sqrt{k_A k_B}\, x(1-x)(h_B^0 - h_A^0)^2 F_\varepsilon , \tag{3.51}$$

where

$$F_d = \frac{k_e k_e'(k_B - k_A)}{k(k_e' + k_A)(k_e' + k_B)} \tag{3.52}$$

and

$$F_\varepsilon = \frac{F_d\sqrt{k_A k_B}}{k_B - k_A} . \tag{3.53}$$

The fluctuations of h_A and h_B can be found by applying the Feynman-Hellman theorem.[12],[18] The results have the same form as those obtained in **I**:

$$\langle (d_A - \langle d_A \rangle)^2 \rangle = \frac{x(1-x)\{[k_A k_B k_e^2]/[k(k_e' + k_A)^2(k_e' + k_B)]\}^2}{W^2/(W_1 - W^2) + [(k - k_A)(k - k_B)]/[(k_e' + k_A)(k_e' + k_B)]} \tag{3.54}$$

$$\langle (d-\langle d\rangle)^2\rangle = \frac{x(1-x)\{[k_A k_B k_e]/[k(k'_e+k_A)(k'_e+k_B)]\}^2 W_1/(W_1-W^2)}{W^2/(W_1-W^2)+[(k-k_A)(k-k_B)]/[(k'_e+k_A)(k'_e+k_B)]} \quad (3.55$$

The EMT is extremely good in describing the random case. Comparison wit computer simulations are shown in Figs. (3.10) - (3.12). The EMT results are show as dashed lines, to contrast with the exact results shown in Figs. (3.5) - (3.7) wher the exact results were shown as solid lines. We see that the average height $\langle d\rangle$ n longer obeys Vegard's law, but is superlinear when $k_B > k_A$. When $k_B < k_A$, th average height $\langle d\rangle$ is sublinear. A sigmoidal shape is never found in this model. Th very stable configuration in the anticlustering case is also obtained when $k_A \neq k_B$ an $x = 1/2$. The EMT contains a cusp in the solution at this point, as does the exac solution obtained when $k_A = k_B$. We have not calculated the widths in Fig. (3.12 for the correlated cases as this would involve very messy summations over the three spin correlation functions. It should be emphasized that the EMT is not exact an although the overall agreement with simulation is excellent, there may be situation where this is not so.

3.5.2 Correlated System

In the random case, the Watson integral is naturally introduced into the EMT t account for the effect of the environment.[17] As we have discussed before, the eas results in the limiting case $k_A = k_B$ show that we can incorporate the ILC into th effective rigidity of the multilayer system by using a suitably modified Watson integra Whenever the problem is analytically soluble, i.e. when the matrix M is non-random we have arrived at expressions for the energy and various average heights. The fac that all the background effects, including correlations, are contained in the Watso integral suggests that $W_C(k)$ is an intrinsic function of the lattice network and it ca be used to describe physical quantities which are related to the first moments of th height distributions, such as the energy and the average height, because these depen

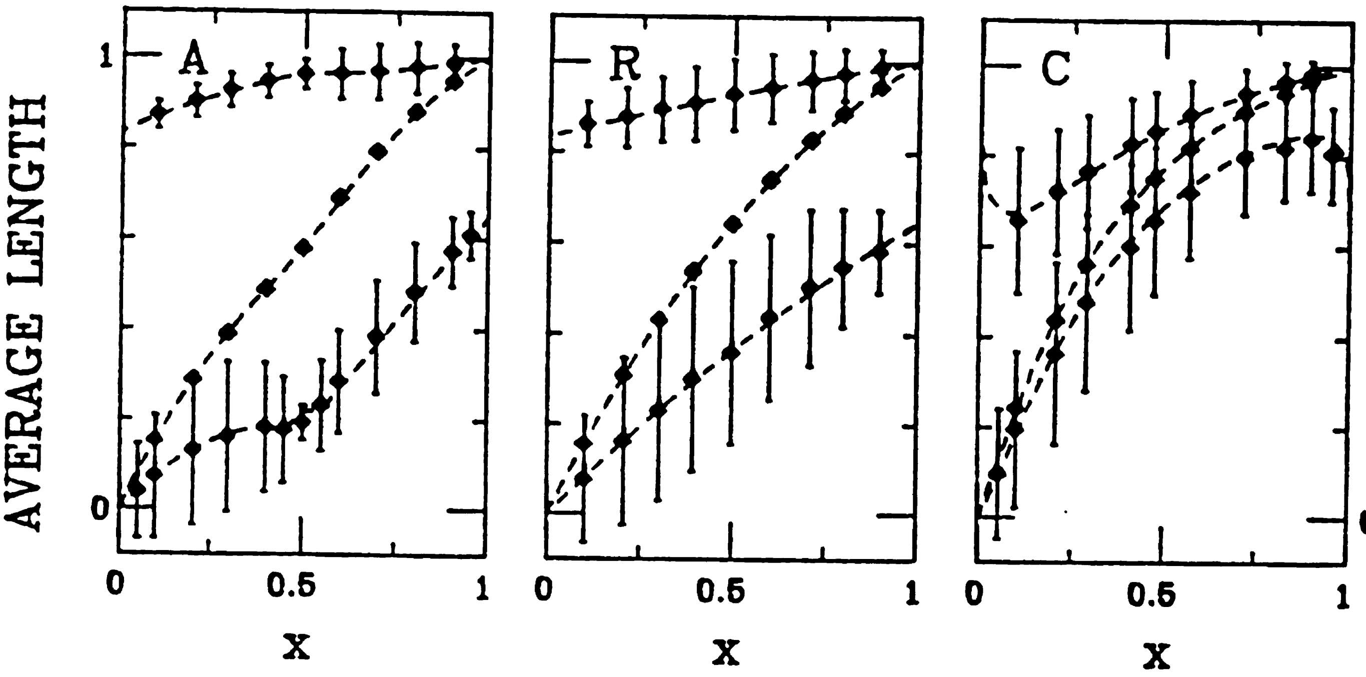

Figure 3.10: Showing the average heights of the A, B galleries $\langle d_A \rangle$, $\langle d_B \rangle$ and th
overall average height $\langle d \rangle$ in dimensionless units. The symbols are from comput
simulations in a $2d$ multilayer system and the dashed lines are from EMT. The vertic
lines represent the full width at half the height for the partial length distributi
functions, and are *not* error bars. The symbols A, R, and C stand for Anticlusterin
Random and Clustering respectively. Here $k_T = k_A$ and $k_B = 5k_A$.

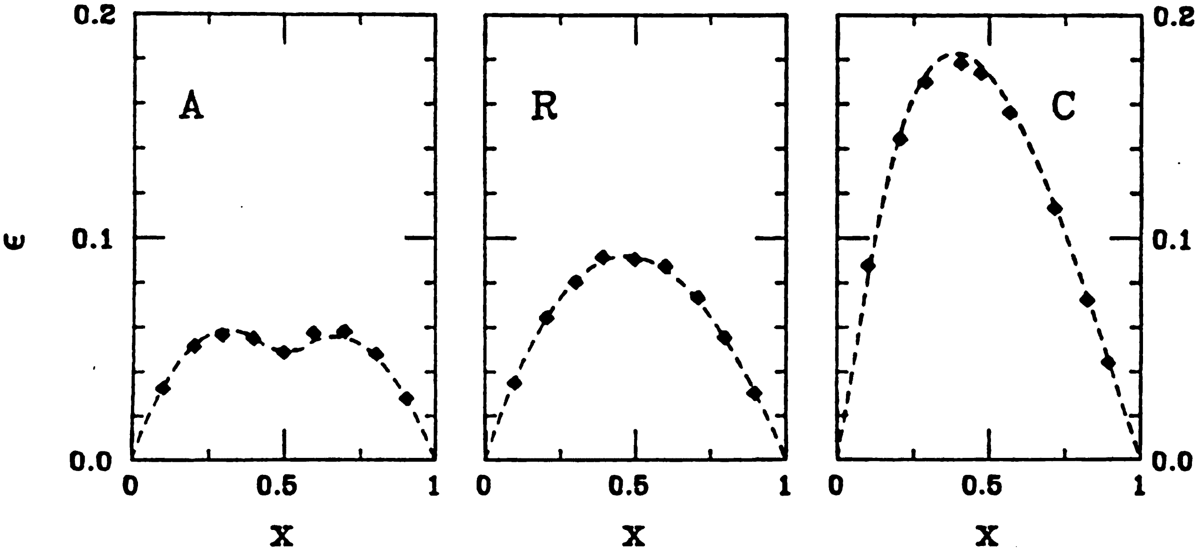

Figure 3.11: The strain energy ϵ, is shown for the $2d$ multilayer case. The symbols are from computer simulations and the dashed lines are from EMT. The symbols A, R, C stand for Anticlustering, Random and Clustering respectively. Here $k_T = k_A$ and $k_B = 5k_A$.

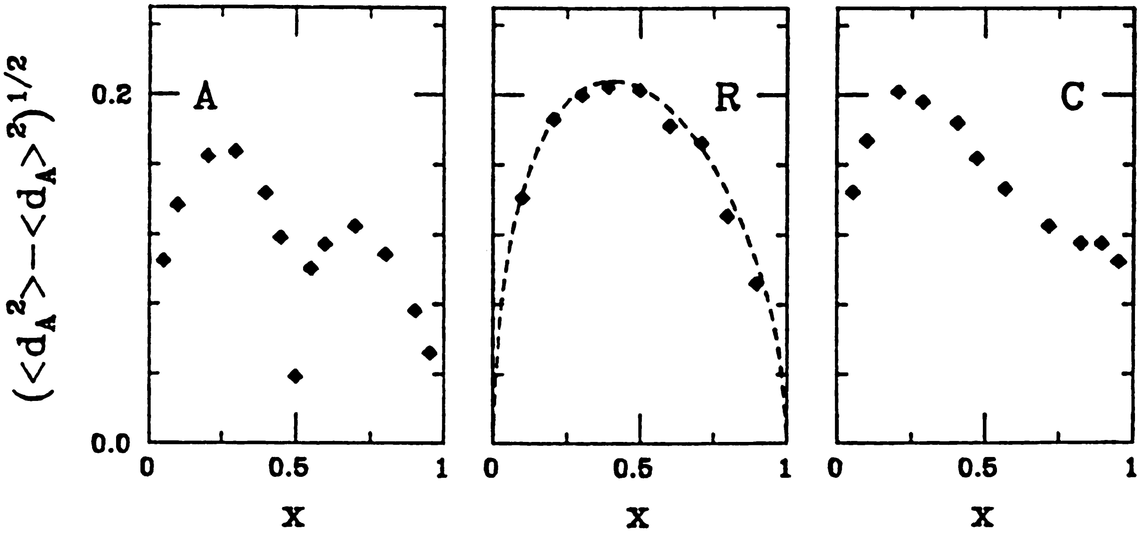

Figure 3.12: The width, $\sqrt{\langle d_A^2\rangle - \langle d_A\rangle^2}$, of the distribution function for the A gallery height for the $2d$ multilayer case. The symbols are from computer simulations and the dashed lines are from EMT. The symbols A, R, C stand for Anticlustering, Random and Clustering respectively. $k_T = k_A$ and $k_B = 5k_A$.

only on two-spin correlations. It then becomes straightforward to construct an EMT for the correlated system and arguments used for the random case above can be extended. We replace $W(k)$ everywhere by $W_C(k)$, which is assumed to characterize the effective medium when correlation is present. The new EMT is found to be surprisingly good when we compare its results with computer simulation as shown in Figs. (3.10) -(3.12). with $P \neq 1$. Indeed the comparisons with simulations when correlations are present, are about as good as for the random case. Note again that we have not carried through the complicated summations over three spin correlation functions that would be necessary to generate results for the correlated cases in Fig. (3.12). In the random case, where $\Lambda = 0$, we have the limits,

$$\begin{aligned} W_C(k) &= W(k) \\ \\ W_{C1}(k) &= W_1(k) \\ &= -k^2 \frac{\partial (W(k)/k)}{\partial k} \\ \\ W_{C2}(k) &= W(k)^2 \, . \end{aligned} \tag{3.56}$$

In both the random case and the correlated cases, there is no linear relation between $\langle d \rangle$ and x in general as demonstrated in Fig. (3.10)..

The *EMT* for a correlated system can be derived also like that for a random one. The interpretation of Eq. (3.41) must be modified. Instead of applying a pair of forces $\pm F$ to the ends of a single bond, it is necessary to apply these forces to **every** A gallary. To avoid a net pressure on the body, forces $\mp Fx/(1-x)$ must also be applied to the ends of all the B galleries. That is, identical forces are applied to the complete set of the A bonds and another set to the B bonds. A generalised force constant $W_c(k)$ is obtained by this procedure, where the conjugate generalised displacement is the mean extension of the A type intercalants. If the bonds are uncorrelated, the effects of the other bonds of the same type being stretched cancels out, leading to Eq. (3.41). If the bonds are correlated, this is no longer the case and $W(k)$ must

be replaced by $W_c(k)$. Note that when a single gallery is stretched with forces F at either end, the effective spring constant is the same as for a perfect lattice order of the static distortion and this extra distortion can be interchanged because the system is linear. These are subtle points that require some thought.

3.6 PROBABILITY DISTRIBUTION FOR GALLERY HEIGHTS

Fig. (3.13) shows the probability distributions $P_A(d)$ and $P_B(d)$ obtained from computer simulations, for various representative cases. It is striking that these distributions are not bounded between 0 and 1, as some of the long bonds are stretched and some of the short bonds are compressed. This did not occur in the bilayers studied in **I**. The reason for this perhaps surprising effect can be seen most easily in the dilute limit, where the distribution of the gallery heights of each intercalant is a main peak surrounded by two satellites. If a single large intercalant is inserted into the system, as in Fig. (3.2), then the adjacent short bonds in the *same* gallery are expanded, whereas the two short bonds in the galleries *above* and *below* are compressed. More interesting is that when $k_A = k_B$, the two peaks for the A and B distributions in the random case in Fig. (3.13) have *the same shape.* This unexpected result was first suggested to us by the computer simulations and then proved rigorously. The result is true for all compositions x so long as both, the distribution remains random and $k_A = k_B$. If either $k_A \neq k_B$ or correlations are present this symmetry is destroyed. This symmetry is especially interesting in the dilute limit, where it relates the host and inclusion distributions.

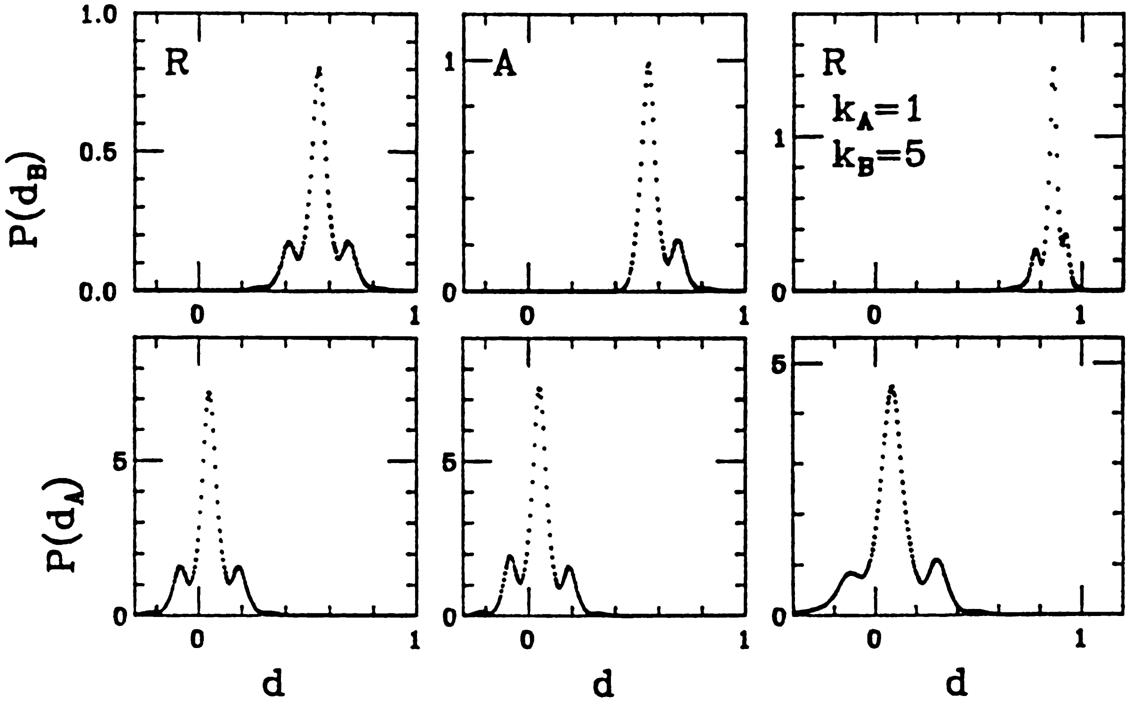

Figure 3.13: The probability distributions $P(d_A)$ and $P(d_B)$ are shown from computer simulations for the $2d$ multilayer system, as a function of the dimensionless distance d. Here $x = 0.1$ in the first two pairs of panels which have $k = k_A = k_B = k_T$. Here R, A stand for Random and Anticlustering respectively. The third pair of panels is also Random with $k_T = k_A$ and $k_B = 5k_A$.

3.6.1 Distribution Function $P_A(d)$ and $P_B(d)$

First let's define the distribution function for d_A and d_B,

$$P_\epsilon(d) \equiv \left\langle \left(\frac{1+\epsilon\sigma_{\rm i}}{2}\right) \delta(d-d_{\rm i})\right\rangle , \tag{3.57}$$

where $(1+\epsilon\sigma_{\rm i})/2$ is the projection on A (or B) when $\epsilon = +1$ (or -1). Replacing the δ-function by a q integral, we get

$$\begin{aligned} P_\epsilon(d) &= \left\langle \left(\frac{1+\epsilon\sigma_{\rm i}}{2}\right) \frac{1}{2\pi}\int_{-\infty}^{+\infty} e^{iq(d-d_{\rm i})}dq\right\rangle \\ &= \frac{1}{2\pi}\int_{-\infty}^{+\infty} e^{iqd}F_\epsilon(q)dq , \end{aligned} \tag{3.58}$$

where

$$F_\epsilon(q) = \left\langle \left(\frac{1+\epsilon\sigma_{\rm i}}{2}\right) e^{-iqd_{\rm i}}\right\rangle . \tag{3.59}$$

and the dimensionless length $d_{\rm i}$ in the above equations can be obtained analytically when $k_A = k_B$ by combining Eq. (3.3) , Eq. (3.7), Eq. (3.11), and Eq. (3.13),

$$d_{\rm i} = x + \sum_{\rm j} A_{\rm ij}\sigma_{\rm j} , \tag{3.60}$$

where

$$A_{\rm ij} = -\frac{1}{2}\left[2({\rm M}^{-1})_{\rm ij} - ({\rm M}^{-1})_{{\rm i}+\nu{\rm j}} - ({\rm M}^{-1})_{{\rm i}-\nu{\rm j}}\right] . \tag{3.61}$$

Substituting $d_{\rm i}$ into Eq. (3.59), we get

$$\begin{aligned} F_\epsilon(q) &= \left\langle \left(\frac{1+\epsilon\sigma_{\rm i}}{2}\right) e^{-iqx}e^{-iq\sum_{\rm j} A_{\rm ij}\sigma_{\rm j}}\right\rangle \\ &= e^{-iqx}\left\langle \left(\frac{1+\epsilon\sigma_{\rm i}}{2}\right) \prod_{\rm j}(\cos qA_{\rm ij} - i\sigma_{\rm j}\sin qA_{\rm ij})\right\rangle , \end{aligned} \tag{3.62}$$

where we have made use of the identity $\sigma_{\rm i}^2 = 1$. So,

$$F_\epsilon(q) = \frac{1}{2}e^{-iqx}\left\{ \langle \prod_{\rm j}(\cos qA_{\rm ij} - i\sigma_{\rm j}\sin qA_{\rm ij})\rangle \right.$$

$$+\epsilon\langle\prod_{j\neq i}(\cos qA_{ij} - i\sigma_j \sin qA_{ij})\rangle \cdot \langle(\sigma_i \cos qA_{ii} - i \sin qA_{ii})\rangle \Big\} \quad (3.63)$$

Notice that the product is over distinct galleries, and so expanding, we will have to average quantities such as $\langle\sigma_l\sigma_m...\sigma_n\rangle$, which is just $\langle\sigma_l\rangle\langle\sigma_m\rangle...\langle\sigma_n\rangle$ in the random case. This means that we can factorize all such products. Using $\langle\sigma_j\rangle = 1 - 2x$, we have

$$F_\epsilon(q) = \frac{1}{2}e^{-iqx}\left[\prod_{j\neq i}(\cos qA_{ij} - i(1-2x)\sin qA_{ij})\right]$$

$$\cdot\Big\{\cos qA_{ii} - i(1-2x)\sin qA_{ii} + \epsilon[(1-2x)\cos qA_{ii} - i\sin qA_{ii}]\Big\} \quad (3.64)$$

Making use of the fact that $\epsilon^2 = 1$, we can rewrite $F_\epsilon(q)$ as

$$\begin{aligned} F_\epsilon(q) &= \left[\frac{1+\epsilon(1-2x)}{2}\right] e^{-iqx}(\cos qA_{ii} - i\epsilon\sin qA_{ii})\prod_{j\neq i}[\cos qA_{ij} - i(1-2x)\sin qA_{ij}] \\ &= \left[\frac{1+\epsilon(1-2x)}{2}\right] e^{-iqx-i\epsilon qA_{ii}}\prod_{j\neq i}[\cos qA_{ij} - i(1-2x)\sin qA_{ij}]\,. \end{aligned} \quad (3.65)$$

Comparing Eq. (3.61) with Eq. (3.24), we know that $A_{ii} = -\frac{1}{2}W(k)$. Therefore,

$$\begin{aligned} \frac{F_A(q)}{F_B(q)} &= \frac{F_+(q)}{F_-(q)} \\ &= \frac{1-x}{x}e^{iqW}\,. \end{aligned} \quad (3.66)$$

This tells us that the two distributions have a weight ratio of $(1-x)/x$ and their positions are shifted by $W(k)$. This is most easily seen by doing the back Fourier Transform to obtain the appropriate probability distribution functions. *Their shapes, however, are exactly the same.*

All information about the system is contained in the distribution function or its Fourier transformation $F_\epsilon(q)$. We have obtained the first and the second moments in **Sec. 3.3**. We can also calculate the moments of the distribution from $F_\epsilon(q)$ as shown

below. Introduce an auxiliary distribution function $F^*(q)$ by the relation,

$$F_A(q) = (1-x)e^{-iqx(1-W)}F^*(q) \ , \tag{3.67}$$

where

$$F^*(q) = e^{-i(1-2x)qA_{\mathrm{ii}}} \prod_{\mathrm{j}\neq\mathrm{i}} [\cos qA_{\mathrm{ij}} - i(1-2x)\sin qA_{\mathrm{ij}}] \ . \tag{3.68}$$

$F_B(q)$ can also be expressed in terms of $F^*(q)$ as

$$F_B(q) = xe^{-iq[1-(1-x)(1-W)]}F^*(q) \ . \tag{3.69}$$

Note that $[x(1-W)]$ and $[1-(1-x)(1-W)]$ are the average values of d_A and d_B, respectively. The quantity $F^*(q)$ is the Fourier transformation of the reduced distribution function $P^*(d)$ which has an average value of 0. From the equation

$$P^*(d) = \frac{1}{2\pi}\int e^{iqd}F^*(q)dq \ , \tag{3.70}$$

we obtain the moment expansion

$$\begin{aligned} F^*(q) &= \int P^*(d)e^{-iqd}d(d) \\ &= \sum_n \left[\frac{(-i)^n}{n!}\int P^*(d)d^n d(d)\right] q^n \\ &\equiv \sum_n c_n^* q^n \ . \end{aligned} \tag{3.71}$$

Note that $\langle d^* \rangle = 0$, so that:

$$M_n \equiv \langle (d^* - \langle d^* \rangle)^n \rangle = \langle (d^*)^n \rangle = \int P^*(d)d^n d(d) = \frac{nc_n^*}{(-i)^n} \ . \tag{3.72}$$

The moments M_n can be calculated from the expansion coefficients c_n^* (see **Appendix B**):

$$M_1 = 0 \tag{3.73}$$

$$M_2 = x(1-x)(W_1 - W^2) \ . \tag{3.74}$$

These results agree with our previous results. Higher moments can also be obtained, although they rapidly become very involved.

$$M_3 = 8x(1-x)(2x-1)\sum_{\mathbf{j}\neq\mathbf{i}} A_{\mathbf{ij}}^3 \,, \tag{3.75}$$

and

$$M_4 - 3M_2^2 = x(1-x)[1-6x(1-x)]\sum_{\mathbf{j}\neq\mathbf{i}} A_{ij}^4 \tag{3.76}$$

We have checked the x dependence of M_3 and M_4 against our simulation results and the agreement is excellent. We have not attempted to calculate the multidimensional integrals necessary to obtain the constants involving the A_{ij} in the expressions for M_3 and M_4 above. This special symmetry is lost when either $k_A \neq k_B$ or correlations are present as indicated in Fig. (3.13). The results we have obtained in this section are general and apply to all types of lattice networks as long as $k_A = k_B$ and the two species are distributed randomly.

There is an accidental symmetry for the $2d$ square net when $k_A = k_B = k$. It can be seen from Fig. (3.13), when $P = 1$, the peak for A (or B) is symmetric around its center. This symmetry can also be demonstrated rigorously by proving the disappearance of all the odd moments of $P^*(d)$. (see **Appendix C**).

3.6.2 Low and High Concentrations

When x is small, the B intercalants can be treated as defects. The single-defect and double-defect problems can be solved exactly. For a single B defect at the origin $\mathbf{i} = 0$, we can obtain all the A heights from Eq. (3.10), where the vector $\mathbf{\Phi}$ has only a single non zero element:

$$d_A(\mathbf{j}) = \frac{1}{N}\sum_{\mathbf{q}} \frac{2[1-\cos(\mathbf{q}\cdot\nu)]}{\lambda_{\mathbf{q}}}\cos(\mathbf{q}\cdot\mathbf{r}_{\mathbf{j}}) \,, \tag{3.77}$$

and

$$d_B^s(0) = \frac{1}{N}\sum_{\mathbf{q}} \frac{2[1-\cos(\mathbf{q}\cdot\nu)]}{\lambda_{\mathbf{q}}} \,. \tag{3.78}$$

Here, the superscript 's' implies a single defect, which has a unique d associated with it. Summing over $\mathbf{j}$ in Eq. (3.77) gives the distribution of d_A in this limit. Eq. (3.78) does not give the distribution of d_B although it gives the position of the center of the distribution. The double-defect configuration, say one B at $\mathbf{i} = \mathbf{0}$ and the other at $\mathbf{j}$, gives us

$$d_B(\mathbf{j}) = \frac{1}{N}\sum_{\mathbf{q}} \frac{2[1 - \cos(\mathbf{q}\cdot\nu)]}{\lambda_{\mathbf{q}}}[1 + \cos(\mathbf{q}\cdot\mathbf{r_j})] \qquad (3.79)$$

Subtracting the position of the center $d^s_B(0)$ from $d_B(j)$, we get the relative position of d_B ,i.e.,

$$\begin{aligned} d^*_B(\mathbf{j}) &= d_B(\mathbf{j}) - d^s_B(0) \\ &= d_A(\mathbf{j})\,. \end{aligned} \qquad (3.80)$$

This explains why the distributions of A and B are identical in this limit. It is interesting that *different* configurations contribute in similar ways to give this equivalence. The above argument in the dilute limit is informative and in particular is helpful in understanding the distributions when the ILC is turned on. In the random case, the configuration $\{...ABBA...\}$ has the same probability as the configuration $\{...ABA...ABA...\}$. The angular brackets $\{....\}$ denote a configuration along the c direction. The $\{...ABBA...\}$ configuration is highly suppressed in the antiferromagnetic (anticlustering) case. So we expect that the distribution of d_B is affected by this suppression. In $\{...ABBA...\}$, B is compressed to a smaller size than in $\{...ABA...ABA...\}$ [from Eq. (3.79)]. This leads to a decrease in the weight of the left satellite of the d_B distribution, while the distribution of d_A is barely affected because this effect is of order x^2. This can be seen by comparing the first two panels in Fig. (3.13). In the random case, $P = 1$, and we have satellites on both sides of the main peak of the d_B distribution. In the strong anticlustering situation, $P = 500$, and the simulation results show that the left satellite of d_B vanishes whereas the distribution of d_A barely changes.

3.7 CONCLUSIONS

We have investigated randomly intercalated multilayer systems described with a harmonic spring model and have obtained an analytic solution for certain cases. We also have reached an understanding of the probability distribution function for the heights of the galleries containing the intercalants and the modification caused by interlayer correlations. Our effective medium theory for both random and correlated intercalation works extremely well in the representative situations tested. It is hoped that our results will be tested experimentally using **EXAFS** in the near future. The formalism used in this work is quite generally applicable and has been used to describe random alloys where the displacements are not uniaxial.[19] Comparing our theoretical results with experiment, the system that comes closest to the situation $R_A = R_B$ is the stage-1 ternary $K_{1-x}Rb_xC_8$. According to our model, this system should show a Vegard's law behavior for the average gallery height(average c-axis periodity) $\langle d \rangle$. There is however a small deviation from Vegard's law; the origin of which is electronic and cannot be accounted for within the present elastic model. In intercalated layered silicates such as $Rb_{1-x}Cs_x$ vermiculite, one observes a sigmoidel x-dependence of $\langle d \rangle$. The initial sublinear x-dependence has been understood[10] in terms of the preferential occupation of non-gallery sites by the larger Cs intercalants. These intercalants do not contribute to the gallery expansion. If one corrects for these sites and considers $\langle d \rangle$ as a function of X_g, the concentration of Cs ion occupying the gallery sites, then one observes a superlinear behavior. This can be understood within the present model as the Cs ion is larger than the Rb ion. Gallery expansion in Li_xC_6 and Li_xTiS_2 can also be included within the present model by treating these systems as $V_{1-x}Li_xC_6$ and $V_{1-x}Li_xTiS_2$ respectively, where V is a vacancy and $R_{Li}/R_V > 1$.[20] More detailed comparison with high quality experimental results remains to be done.

Bibliography

[1] F. S. Galasso, *Structure and Properties of Inorganic Solids* (Pergammon, New York, 1970).

[2] L. Vegard, Z. Phys. **5**, 17 (1921).

[3] J. B. Thompson, in *Researches in Geochemistry*, Vol. II, ed. by P. H. Abelson, (Wiley, New York, 1967) p. 340.

[4] J. R. Dahn, D. C. Dahn, and R. R. Haering, Solid State Comm. **42**, 179 (1982).

[5] J. E. Fisher and H. J. Kim, Phys. Rev. B **35**, 3295 (1987).

[6] S. A. Solin and H. Zabel, Adv. Phys. **37**, 87 (1988).

[7] P. C. Chow and H. Zabel, Phys. Rev. B **38**, 12837 (1988).

[8] D. Medjahed, R. Merlin, and R. Clark, Phys. Rev. B **36**, 9345 (1987).

[9] W. Jin and S. D. Mahanti, Phys. Rev. B **37**, 8647 (1988).

[10] H. Kim, W. Jin, S. Lee, P. Zhou, T. J. Pinnavaia, S. D. Mahanti, and S. A. Solin, Phys. Rev. Lett. **60**, 2168 (1988); S. Lee, S. A. Solin, W. Jin and S. D. Mahanti, in *Graphite Intercalation Compounds: Science and Technology*, Ed. by M. Endoh, M. S. Dressellhaus and G. Dressellhaus, p. 41 (Materials Research Society, 1988).

[11] M. F. Thorpe, Phys. Rev. B **39**, 10370 (1989).

[12] M. F. Thorpe, W. Jin, and S. D. Mahanti, Phys. Rev. B **40**, 10294 (1989).

[13] M. Mori, S. C. Moss, Y. M. Yan and H. Zabel, Phys. Rev. B **25**, 1287 (1982).

[14] K. Komatsu, J. Phys. Soc. of Japan, **6**, 438 (1951); see also S. Lee, H. Miyazaki, S. D. Mahanti, and S. A. Solin, Phys. Rev. Lett. **62**, 3066 (1989).

[15] D. C. Mattis, *The Theory of Magnetism*, (Harper & Row, New York, 1965), p. 258.

[16] See for example, J. C. Mikkelson, Jr. and J. B. Boyce, Phys. Rev. B **28**, 7130 (1983).

[17] S. Feng, M. F. Thorpe, and E. Garboczi, Phys. Rev. B **31**, 276 (1985).

[18] R. P. Feynman, Phys. Rev. **56**, 340 (1939).

[19] M. F. Thorpe and E. J. Garboczi, Phys. Rev. B**42**,8405(1990)

[20] S. Lee, H. Miyazaki, S. D. Mahanti, and S. A. Solin.(See Ref.14)

Chapter 4

STRUCTURAL CHARACTERISATION OF SEMICONDUCTOR ALLOYS

This chapter is to be submitted to Physical Review B. This preliminary version is written by the author and the paper will be published under the names of Y. Cai and M. F. Thorpe.

4.1 INTRODUCTION

Electronic properties of semiconductors can be changed by varying the concentration of components. Structural information on semiconducting materials is of fundamental importance in calculating and predicting these properties. Extended X-ray absorption fine structure (EXAFS) experiments have found that pseudobinary semiconductor alloy system $(A_{1-x}B_x)C$ shows a bimodal structure.[2]-[7] The first neighbor cation-anion distance remains closer to that in the pure binary compound than to that of the average or virtual crystal distance. The discovery inspired considerable theoretical interest.[8]-[11] All these theories are quite successful though they focus

on the dilute limit. In this chapter we study all the pseudobinary semiconductor alloys, with arbitrary concentrations within the valence force model. They are shown to be isomorphous to the general **length mismatch problem.** [13],[14] The model is also applicable to binary alloy system like Ge_xSi_{1-x} and the quaternary alloys $A_{1-x}B_xC_{1-y}D_y$. Our investigation provides a better understanding of the Vegard's law[1]. This chapter will be presented in the following way. As an introduction to later work, we first discuss the valence force models in sect. **4.2**. The force constants of the models are fit from elastic measurements for known pure binary crystals. In sect. **4.3** we apply the appropriate valence force model to the alloy system and give exact solution to pure length mismatch problem when there is no force constant disorder. The simple result allows us appreciate the importance of the **Watson Integral,** which characterizes the topological rigidity of the lattice system. We will also discuss its importance in the construction of an effective medium theory, for use when there is force constant disorder. In sect. **4.4** we study in considerable detail all ternary $III-V$ and $II-VI$ semiconductor alloys using both effective medium theory and computer simulation. It is found the theory very well reproduce the structural features observed in experiment.

4.2 VALENCE FORCE MODELS

In this section we study the Kirkwood Modeland Keating Model[15] together in a combined form. Valence force models have been used to study semiconductors quite successfully. In diamond or zincblende structure, nearest neighbor interaction along can not solidify the system. There are one third vibrational modes of zero frequency because of the understraining. Farther range interactions are needed to stabilize the system. Kirkwood and Keating model contain second neighbor interactions and are all able to stabilize the zincblende structures that we are going to discuss. There are some subtle differences between these two models. And Keating model is tested to be

better. This may be due to the fact that Keating derived his model from symmetric point of view, while Kirkwood model does not satisfy the rotational invariance. We will see the difference is minor. In Kirkwood model, the angular restoring part of the deformation energy is written as the square of angular difference,

$$E_{kirkwood} = \frac{\alpha}{2}\sum_{\langle ij\rangle}(h_{ij} - h^0_{ij})^2 + \frac{\beta'}{8}\sum_{\langle ijl\rangle}(\cos\theta_{ijl} - \cos\theta^0_{ijl})^2 \tag{4.1}$$

α and β' are nearest neighbor and angular force constant respectively. h_{ij} is the bond length between atoms i and j. h^0_{ij} is the natural length. θ_{ijl} is the angle made by nearest neighbor bonds ij and il. The natural angle θ^0_{ijl} is usually taken to be about 109^o as in perfect diamond lattice. The sign $\langle\rangle$ under summation excludes the double counting.

The energy can be written in expansion form for small length mismatch. Denote h_e the nearest neighbor distance of the underline crystal structure, and $\mathbf{u}_i$ the displacement vector of atom i from its crystalline position, and keep to linear term,

$$h_{ij} = h_e + \hat{\mathbf{r}}_{ij}\cdot\mathbf{u}_{ij} \tag{4.2}$$

where $\hat{\mathbf{r}}_{ij}$ is the unit vector in crystalline structure pointing from atom j to i. Redefine the angular force interaction parameter,

$$\beta = \frac{\beta'}{h_e^2} \tag{4.3}$$

we have the expansion form(only keep to linear terms for simplicity and it is found to be a good approximation):

$$E_{kirkwood} = \frac{\alpha}{2}\sum_{\langle ij\rangle}(h_e - h^0_{ij} + \hat{\mathbf{r}}_{ij}\cdot\mathbf{u}_{ij})^2 + \frac{\beta}{8}\sum_{\langle ijl\rangle}[\hat{\mathbf{r}}_{ij}\cdot\mathbf{u}_{il} + \hat{\mathbf{r}}_{il}\cdot\mathbf{u}_{ij} + \frac{1}{3}(\hat{\mathbf{r}}_{ij}\cdot\mathbf{u}_{ij} + \hat{\mathbf{r}}_{il}\cdot\mathbf{u}_{il})]^2 \tag{4.4}$$

In the perfect system, there is no length mismatch and $h_e = h^0_{ij}$, we have,

$$E_{kirkwood} = \frac{\alpha}{2}\sum_{\langle ij\rangle}(\hat{\mathbf{r}}_{ij}\cdot\mathbf{u}_{ij})^2 + \frac{\beta}{8}\sum_{\langle ijl\rangle}[\hat{\mathbf{r}}_{ij}\cdot\mathbf{u}_{il} + \hat{\mathbf{r}}_{il}\cdot\mathbf{u}_{ij} + \frac{1}{3}(\hat{\mathbf{r}}_{ij}\cdot\mathbf{u}_{ij} + \hat{\mathbf{r}}_{il}\cdot\mathbf{u}_{il})]^2 \tag{4.5}$$

To compare with Keating Model,

$$E_{keating} = \frac{\alpha}{2}\sum_{\langle ij\rangle}(\hat{\mathbf{r}}_{ij}\cdot\mathbf{u}_{ij})^2 + \frac{\beta}{8}\sum_{\langle ijl\rangle}(\hat{\mathbf{r}}_{ij}\cdot\mathbf{u}_{il} + \hat{\mathbf{r}}_{il}\cdot\mathbf{u}_{ij})^2 \tag{4.6}$$

It can be seen that these two models are very similar except there are two more terms in Kirkwood model. In fact we can combine them in a single model and study them together,

$$E_{\lambda} = \frac{\alpha}{2}\sum_{\langle ij\rangle}(\hat{\mathbf{r}}_{ij}\cdot\mathbf{u}_{ij})^2 + \frac{\beta}{8}\sum_{\langle ijl\rangle}[\hat{\mathbf{r}}_{ij}\cdot\mathbf{u}_{il} + \hat{\mathbf{r}}_{il}\cdot\mathbf{u}_{ij} + \frac{\lambda}{3}(\hat{\mathbf{r}}_{ij}\cdot\mathbf{u}_{ij} + \hat{\mathbf{r}}_{il}\cdot\mathbf{u}_{il})]^2 \tag{4.7}$$

where $\lambda = 0$ stands for Keating model and $\lambda = 1$ stands for Kirkwood model.

The elastic modulus of the combined λ-model can be solved in the similar way as in Keating's original chapter.[15] The results are,

$$\begin{aligned} C_{11} &= \frac{1}{4}(\alpha + 3\beta - \frac{2\lambda\beta}{3} + \frac{\beta\lambda^2}{3}) \\ C_{12} &= \frac{1}{4}(\alpha - \beta - \frac{2\lambda\beta}{3} + \frac{\beta\lambda^2}{3}) \\ C_{44} &= \frac{1}{4}\left\{\alpha + \beta - \frac{2\lambda\beta}{3} + \frac{\beta\lambda^2}{9} - \frac{[\alpha - \beta(9-\lambda^2)/9]^2}{\alpha + \beta(1+\lambda/3)^2}\right\} \end{aligned} \tag{4.8}$$

and we can also work out the frequency of the optical phonon at $\mathbf{k} = 0$ for the combined λ-model,

$$\omega_0 = \sqrt{\frac{8}{m}[\alpha + \beta(1 + \frac{\lambda}{3})^2]} \tag{4.9}$$

where m is the mass and the lattice constant is taken to be one.

The force constants in the models are so chosen to fit C_{11} and bulk modulus. We list in Table.(I) the force constants for different compounds. It can be seen that β is the same for both the Keating model and the Kirkwood model. The α constants do not change too much from Kirkwood to Keating description. The main reason that

	Kirkwood		Keating	
	α	β	α	β
AlP	65.03386	14.19144	60.30338	14.19144
$AlAs$	44.18573	8.94280	41.20480	8.94280
$AlSb$	35.69020	6.79200	33.42620	6.79200
GaP	48.06614	10.69252	44.50197	10.69252
$GaAs$	44.34032	9.25720	41.25459	9.25720
$GaSb$	34.29977	7.33188	31.85581	7.33188
InP	41.72646	6.60229	39.52569	6.60229
$InAs$	35.09977	5.75993	33.17979	5.75993
$InSb$	31.30400	5.07011	29.61396	5.07011
ZnS	40.30599	4.78803	38.70998	4.78803
$ZnSe$	33.74111	4.56242	32.22031	4.56242
$ZnTe$	31.06783	4.66933	29.51139	4.66933
CdS	35.66434	4.75621	34.07893	4.75621
$CdSe$	33.18513	4.37257	31.72761	4.37257
$CdTe$	27.30606	2.72412	26.39802	2.72412
$HgTe$	30.72841	2.93264	29.75086	2.93264

Table 4.1:

we adopt the Kirkwood model is its simplicity when there is size difference in the system. As can be seen in Eq.(4.1), the length mismatch enters only in the α part. This makes it easy to be solved in a familiar way.[13],[14] Considering that the β part contributes less than the α part, we expect that the two models should generate qualitalively similar results.

For most of the binary alloys we studied, as in table (**I**), the fitted force constants α and β give C_{44} and ω_0 within 20% of the experimental values. Of course it is possible to choose different angular force constants for ABA and BAB type bonding and this leads to better fitting of the elastic constants and optical mode frequency. One can further consider the charge transferring and deploy shell model. However our current effective medium theory does not tolerate too many disorders in the force constants and on the other hand the local structure is not very sensitive to the difference. And more sophisticated potential like the Embedded Atom Potential can only be studied in numerical simulations. We will adopt the one-set-parameter fitting to get simple theoretical predictions.

4.3 THEORY

In this section we first solve the pure length mismatch problem of $(A_{1-x}B_x)C$ system. Then we study the **Watson Integral**. Finally we discuss the effective medium method.

The structure is zincblende for pure AC and BC binary system. For example, in the AC binary system, A and C each occupy one of the FCC sublattices in the zincblende structure, and the same for BC binary alloy. To make $(A_{1-x}B_x)C$, AC and BC alloys are mixed with appropriate concentration $1-x$ and x. In the final structure, C-type atoms take one of the FCC sublattices while A and B occupy the other FCC sublattice randomly. We assume no correlations between A and B atoms.

4.3.1 Solution to Pure Length Mismatch

Our theoretical approach to the problem assumes harmonic approximation. This is valid in small mismatch situation. Start from the energy form of Eq.(4.4). It can be written in compact form. We discard the subscript "Kirkwood" from now on,

$$E = \frac{1}{2}\mathbf{U}^{+}\mathbf{M}\mathbf{U} - \mathbf{U}^{+}\phi + E_0; \tag{4.10}$$

where **U** is the displacement vector and **M** is the structure or connectivity matrix. The disorder vector ϕ can be expressed as,

$$\begin{aligned} \phi &= \sum_{\langle ij\rangle} \phi_{ij}\hat{\mathbf{r}}_{ij}|ij> \\ &= \sum_{\langle ij\rangle} \phi_{ij}|\vec{\mathbf{ij}}> \end{aligned} \tag{4.11}$$

where

$$\phi_{ij} = -\alpha(h_e - h_{ij}^0) \tag{4.12}$$

and E_0 takes the form,

$$E_0 = \frac{\alpha}{2}\sum_{\langle ij\rangle}(h_e - h_{ij}^0)^2 \tag{4.13}$$

Define the reduced length d as,

$$d = \frac{h - h_A^0}{h_B^0 - h_A^0} \tag{4.14}$$

Apply the same idea as in multilayer system[13], we get the total average length, average length of AC type bond, BC type bond and distortion energy(see **Appendix D**).

The results turn out to be very similar in form to the results we reached in the Intercalated Graphite Multilayer system[13] and the 2d triangular network.[14]

$$\begin{aligned} \langle d\rangle &= x \\ \langle d_{AC}\rangle &= x(1 - a^{**}) \end{aligned}$$

$$\begin{aligned}\langle d_{BC} \rangle &= 1-(1-x)(1-a^{**}) \\ \epsilon &= \frac{1}{2}x(1-x)(1-a^{**}) \end{aligned} \tag{4.15}$$

ϵ is the reduced energy per site. The Watson integral a^{**} here is for sites case instead of bond case. It can be evaluated from the static Green's function directly(see **Appendix D**).

The simple results above should be properly appreciated because of the correlation involved in the site mixing case. In the AB type random alloy the solution is lengthy and more lattice integrals are involved.[17] The compact form is attributed to the regular occupying of one sublattice by C type atoms.

To write down the length fluctuation it needs the introduction of another "Watson" integral a_1^{**},[13]

$$a_1^{**} = -\alpha^2 \frac{\partial(a^{**}/\alpha)}{\partial \alpha} \tag{4.16}$$

where α the central force constant. For example the fluctuation of AC type bond length,

$$\langle d_{AC}^2 \rangle - \langle d_{AC} \rangle^2 = x(1-x)(a_1^{**} - a^{**2}) \tag{4.17}$$

The derivation for fluctuations is more difficult than that given in **Appendix D** but shares the same old idea.[13],[14] In triangular and FCC lattice[14] a^{**} is independent of the force constant α. So $a_1^{**} = a^{**}$. It is not the case in Zincblende structure because of the angular force term in the energy expression. In general these quantities depend on ratio of the force constants as well as the concentration. We will address this aspects of the Watson Integral specifically next.

	Keating			*Kirkwood*		
	C_1	C_2	C_3	C_1	C_2	C_3
a^*	2.198	3.200	0.796	2.0058	3.200	0.880
a^{**}	2.2786	4.600	2.629	1.2489	3.600	1.171

Table 4.2:

4.3.2 Watson Integrals as Function of Force Ratio

We need to study the Watson integrals because they are the only parameters involved in all local properties. These integrals characterize the rigidity of the system and contain the information about the correlation. The ratio of the force constants, $y \equiv \alpha/\beta$, varies from 0.1 to 0.6 under valence force model description. For the purpose of effective medium study, we needs a simple analytic form to describe the change of these integrals as function of the force ratio. And it is found the following form well describes the Watson integral in the ratio range from 0.0 to 0.7,

$$a^*(y) = \frac{1 + C_1 y}{1 + C_2 y + C_3 y^2} \tag{4.18}$$

The integral used in fluctuations associated with a^* is defined as:

$$a_1^*(y) = \frac{\partial(y a^*)}{\partial y} \tag{4.19}$$

The values of the parameters are listed in Table. (**II**). And Fig.4.1 demonstrates the good representation of the Watson Integral by the above simple analytic form.

4.3.3 Effective Medium Theory

When there are disorder not only in size, but also in force constants, there is no analytic solution. And in practice this is always the case. We need to develop methods with more approximation. The Effective Medium Approximation we used here has been applied by Thorpe and et. al. to many other problems. The essential idea is

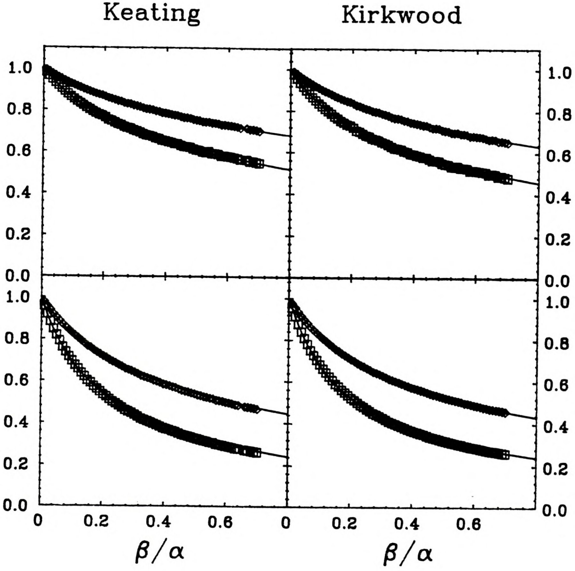

Figure 4.1: The Watson Integral as function of the force ratio α/β. The top panels for a^* and bottom for a^{**}. Diamond denotes a and square denotes a_1 which relates to the derivative of a and can be calculated from the fluctuation of distribution. These two symbols are from computer simulation. Straight lines are the three parameter fitting.

to replace the effect of the matrix on an embedded chemical bond by another bond of appropriate strength and natural length so to reach self consistency. The rigidity and correlation information are contained in the Watson Integrals which appear in the expressions of the quantities concerned.

We will list the results only and leave the derivation to reference paper[13] for interested readers. The results are written in reduced variables d instead of h, and subscript A means AC bond and B means BC type.

$$\langle d \rangle = x + x(1-x)F_d \tag{4.20}$$

$$\langle d_A \rangle = \frac{x k_e k'_e k_B}{k(k'_e + k_A)(k'_e + k_B)} \tag{4.21}$$

$$\langle d_B \rangle = 1 - \frac{(1-x) k_e k'_e k_A}{k(k'_e + k_A)(k'_e + k_B)} \tag{4.22}$$

$$\varepsilon = \frac{1}{2}\sqrt{k_A k_B}\, x(1-x)(h_B^0 - h_A^0)^2 F_\varepsilon \, , \tag{4.23}$$

where

$$F_d = \frac{k_e k'_e (k_B - k_A)}{k(k'_e + k_A)(k'_e + k_B)} \tag{4.24}$$

and

$$F_\varepsilon = \frac{F_d \sqrt{k_A k_B}}{k_B - k_A} \, . \tag{4.25}$$

And the fluctuations,

$$\langle (d_A - \langle d_A \rangle)^2 \rangle = \frac{x(1-x)\{[k_A k_B k_e^2]/[k(k'_e + k_A)^2 (k'_e + k_B)]\}^2}{W^2/(W_1 - W^2) + [(k - k_A)(k - k_B)]/[(k'_e + k_A)(k'_e + k_B)]} \tag{4.26}$$

$$\langle (d - \langle d \rangle)^2 \rangle = \frac{x(1-x)\{[k_A k_B k_e]/[k(k'_e + k_A)(k'_e + k_B)]\}^2 W_1/(W_1 - W^2)}{W^2/(W_1 - W^2) + [(k - k_A)(k - k_B)]/[(k'_e + k_A)(k'_e + k_B)]} \tag{4.27}$$

In pure length mismatch problem, the EMT goes back to exact solution, and we observe the generalized Vegard's law, i.e., linear changing of average length with concentration, not only for the total average length, but also for specific average length AC and BC, even when there is correlation. However, Vegard's law is destroyed when the force constants α and β are different for AC and BC binary systems.

In real compounds, the difference in the ratio of force constants, α/β, is not large. And this leads to the non-remarkable deviation from Vegard's law in the experimental data. But in general, Vegard's law is not obeyed.

4.4 APPLICATION

Out of the 36 possible ternary alloys that could be formed from Zn, Cd, Hg, P, As, Sb, and Al, Ga, In, Si, Ge, Sn, we study the 29, for which force constants can be extracted from experimental data. We use the Kirkwood model so to get the comparison between simulation and effective medium theory.

It is easy to solve the effective medium approximation using the function form of the Watson Integral given in Eq.(4.18). Fig.(4.2) to Fig.(4.5) show the computer simulations and effective medium results. The excellence of EMT is well demonstrated. Compared with experiments data availible, we plot the "Z" curves for $In_xGa_{1-x}As$ in Fig.(4.6) and $Zn_xCd_{1-x}Te$ in Fig.(4.7).

We see that both simulation and EMT give fairly good account of the experimental measurements. All the curves are essentially straight plus a miner bowing, as the following description,

$$h = p_1(1-x) + p_2 x + p_3 x(1-x) \tag{4.28}$$

p_1 is the length at the zero concentration and p_2 on the 100% side. p_3 denotes the bowing of the curve.

The three parameters can be solved from EMT numerically. We can also derive an approximate values of these three parameters from EMT equation.

Denote $\bar{\alpha} = (\alpha_A + \alpha_B)/2$, and $\bar{\beta} = (\beta_A + \beta_B)/2$. For AC type bond,

$$p_1 = h_A^0 + \frac{h_B^0 - h_A^0}{1 + \alpha_A/\{\alpha_B[1/a^{**}(\beta_B/\alpha_B) - 1]\}}$$

$$p_2 = h_A^0$$

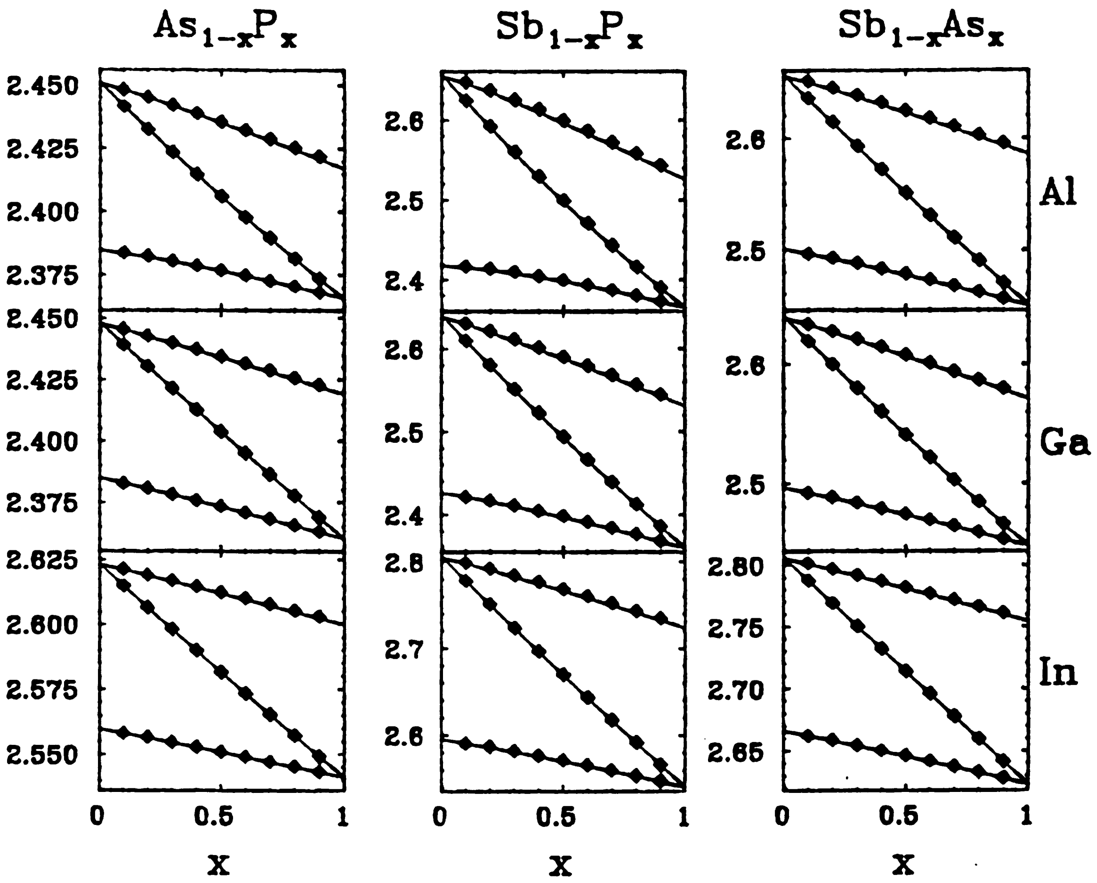

Figure 4.2: .

The "Z" curve for $III - V$. Solid lines are from Effective Medium Theory. The Kirkwood model is used in the computer simulation

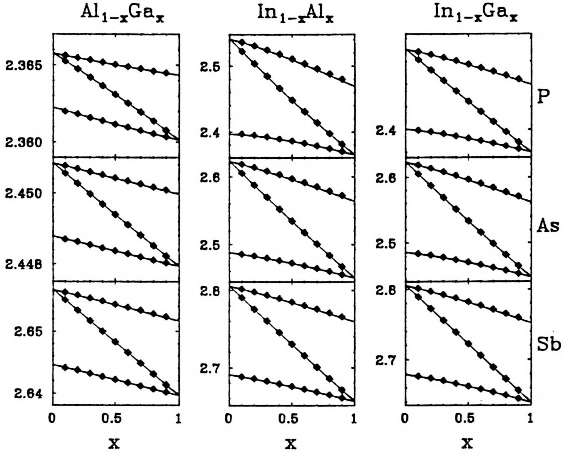

Figure 4.3: .

The "Z" curve for $III - V$. Solid lines are from Effective Medium Theory. The Kirkwood model is used in the computer simulation

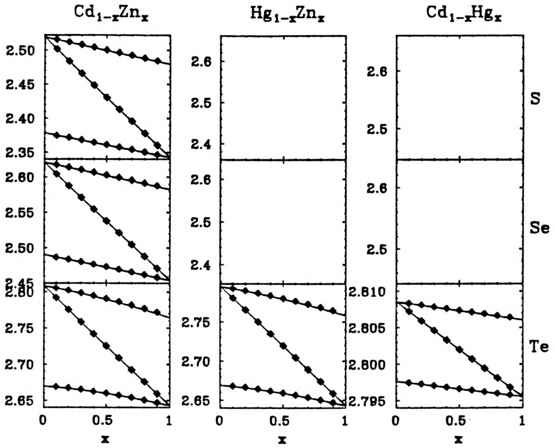

Figure 4.4: .

The "Z" curve for $II - VI$. Solid lines are from Effective Medium Theory. The Kirkwood model is used in the computer simulation

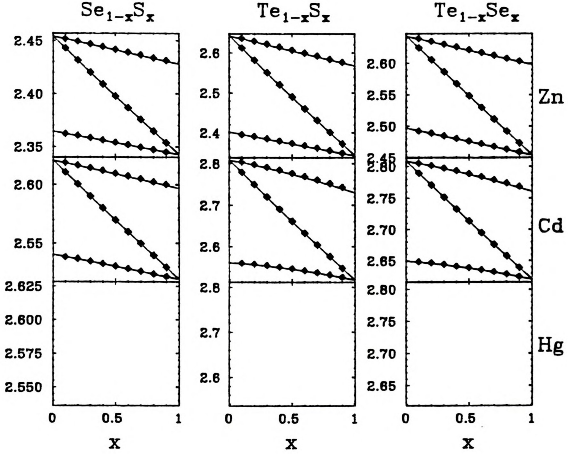

Figure 4.5: .

The “Z” curve for $II - VI$. Solid lines are from Effective Medium Theory. The Kirkwood model is used in the computer simulation

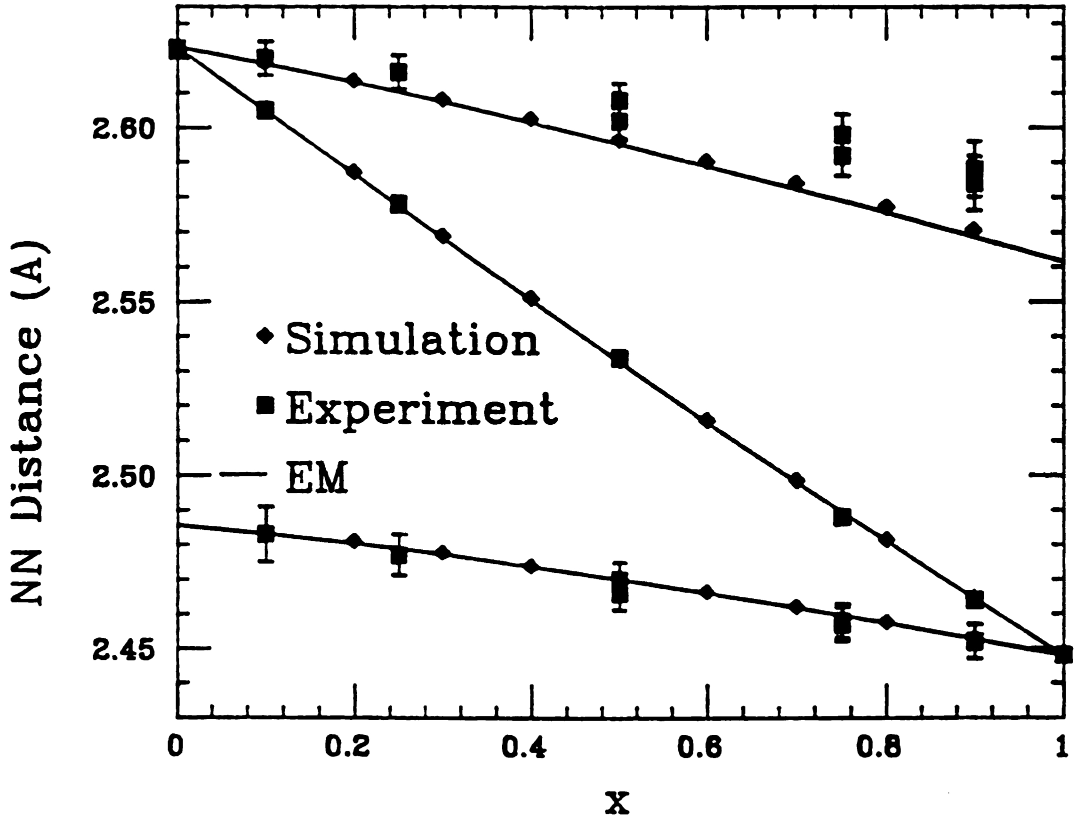

Figure 4.6: The "Z" curve for $In_{1-x}Ga_xAs$. Solid lines are from Effective Medium Theory. The Kirkwood model is used in the computer simulation. Experimental data goes with error bar.

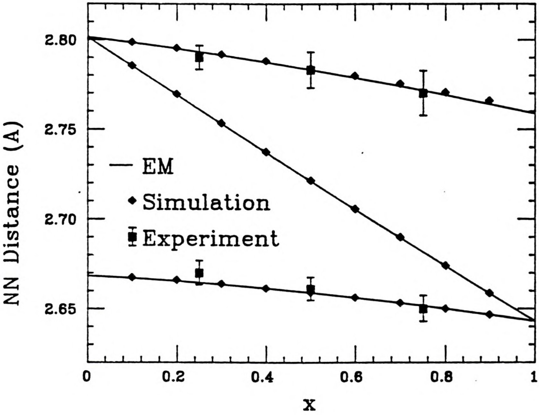

Figure 4.7: The "Z" curve for $Cd_{1-x}Zn_xTe$. Solid lines are from Effective Medium Theory. The Kirkwood model is used in the computer simulation,experimental data goes with error bar.

$$p_3 = \{[1 - a^{**}(\bar{\beta}/\bar{\alpha})]^2(\frac{\alpha_B - \alpha_A}{\bar{\alpha}}) + a^{**\prime}(\bar{\beta}/\bar{\alpha})(\frac{\beta_B - \beta_A}{\bar{\beta}})](h_B^0 - h_A^0) \quad (4.29)$$

The prime means derivative over the argument inside. For the BC type bond, the parameter p_3 takes the same form. p_1 takes the form of p_2 for the AC bond, but with A and B switched. The same change occurs for parameter p_2.

For the total average,

$$p_1 = h_B^0$$

$$p_2 = h_A^0$$

$$p_3 = \{[1 - a^{**}(\bar{\beta}/\bar{\alpha})](\frac{\alpha_B - \alpha_A}{\bar{\alpha}})(h_B^0 - h_A^0) \quad (4.30)$$

It is interesting to analyze the approximation expression above. We can see that the bowing of the curve for AC and BC are the same. They depend on the differences of α and β of the two binary components. However, the bowing of the total length average only depends on the difference of the central force α. For most alloys the bowing of total average and specific average go in opposite directions, i.e., the angular force difference is dominating in the bowing in specific length average.

The length distribution is approximately Gaussian. Fig.4.8 shows the distribution of nearest neighbor in $Cd_{0.5}Zn_{0.5}Te$ system. There is barely any overlap between two peaks, in contrary to the situation in metal alloys, where distributions have very remarkable overlap. This is mainly due to the soft angular force in semiconducting materials, in which deformation in atomic distance is more energetic than that in the angle of two neighboring chemical bonds. The widths of AC and BC distribution is not exactly the same because of the difference in force constants and also because of the bond-correlation in site disordered system. Like in correlated Intercalated Graphite system, EMT does not give good prediction for the width of the distribution. Of course we can get these informations from computer simulations.

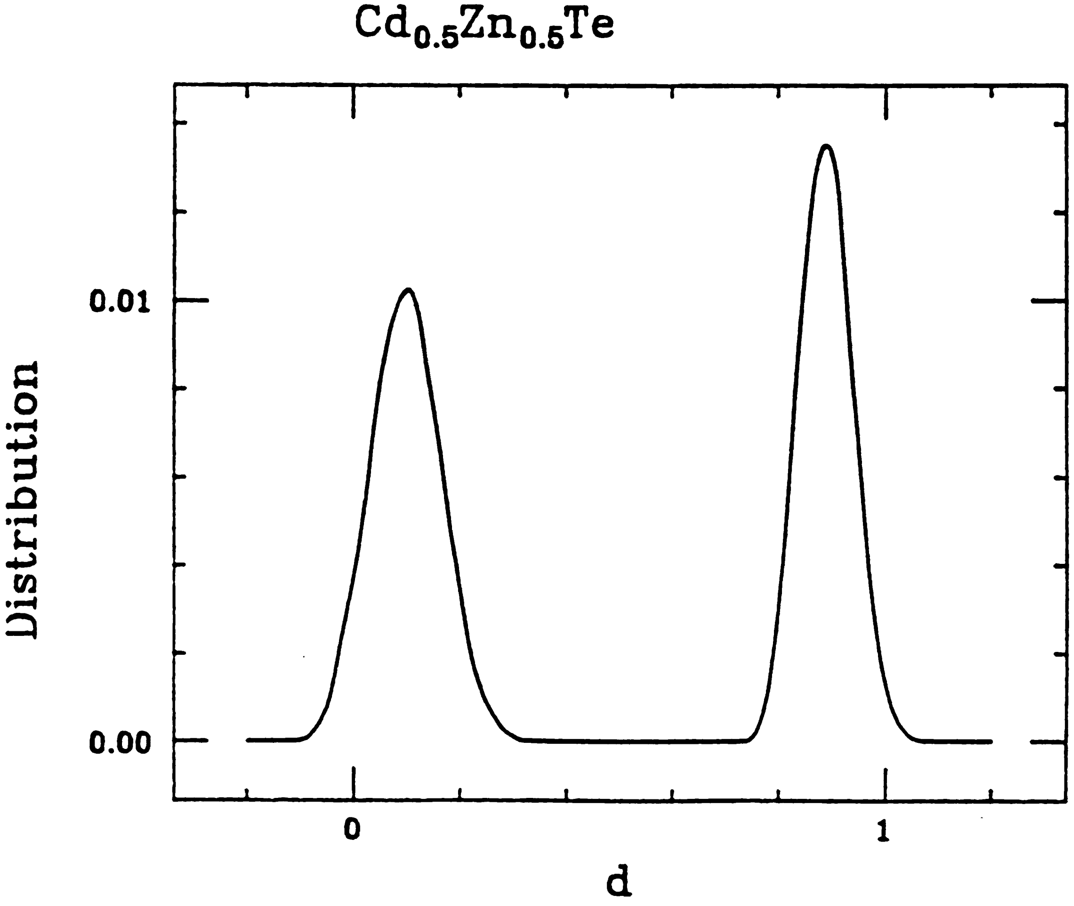

Figure 4.8: The length distribution of $Cd_{0.5}Zn_{0.5}Te$. The shapes are approximately gaussian. Correlations and the difference in the α force constants make the two peak different.

4.5 CONCLUSIONS

We studied the properties of the Kirkwood and the Keating model by combining them into a unified model. Then we studied the structure of the $(A_{1-x}B_x)C$ system. An exact solution is found for the pure length mismatch problem. And effective medium theory is applied to multinary compounds and get good agreement. While preliminary information is available from theory, the full configuration of multinary system can be solved by computer simulation. The X-ray scattering calculation can also be performed.[16] It reveals the long range properties of structure of multinary compounds. The accomplishment allows us to appreciate more of the simplicity by introducing the concepts of chemical bond and natural length in solid state materials. And we point out that the bimodel properties is characteristic of all "length mismatch problems". In these systems the nature of the chemical bond is assumed not to change significantly in different circumstances and a natural length for the chemical bonding is adopted to simplify the interaction picture. The relaxation of the natural length in mismatched system inevitably leads to the bimodel observations that the deformed chemical bond will stay as close as possible to its natural length.

Bibliography

[1] L. Vegard, Z. Physik 5 (1921) 17.

[2] J. C. Mikkelsen and J. B. Boyce, Phys. Rev. Lett. **40**, 9001978.

[3] J. C. Mikkelsen, Jr. and J. B. Boyce, Phys. Rev. B28(1983).

[4] J. C. Mikkelsen and J. B. Boyce, Phys. Rev. Lett. **49**, 14121982.

[5] J. B. Boyce and J. C. Mikkelsen, Jr., Phys. Rev. B31 (1883) 6803.

[6] A. Balzarotti, in: Ternary and Multinary compounds, Eds. S. K. Deb and Zunger(Material Research Society, Pittsburgh, PA, 1987)p.333.

[7] T. Sasaki, T. Onda, R. Ita and N. Ogasawara, Japan, J. Appl. Phys. 25 (1986) 231.

[8] J. L. Martins and A. Zunger, Phys. Rev. B30 (1984) 6217

[9] A. B. Chen, A. Sher, Phys. Rev. B32 (1885) 3695

[10] C. K. Shih, W. E. Spicer, W. A. Harrison and A. Sher, Phys. Rev. B31 (1985) 1139

[11] M. Podgorny, M. T. Czyzyk, A. Balzarotti, P. Letardi, N. Motta, A. Kisiel and M. Zimnal-Starnawska, Solid State Commun. 55 (1985) 413

[12] Y. Cai and M. F. Thorpe, Phys. Rev. B40 (1989) 10535

[13] Y. Cai, J. S. Chung, M. F. Thorpe and S. D. Mahanti, Phys. Rev. B**42**, 8827 (1990)

[14] M. F. Thorpe and E. J. Garboczi, Phys. Rev. B**42**, 8405 (1990)

[15] P. N. Keating, Phys. Rev. **145**, 637(1966)

[16] M. F. Thorpe, J. S. Chung and Y. Cai, to be published in Phys. Rev. B.

[17] J. Chen and M. F. Thorpe, unpublished

[18] "Group III: Crystal and Solid State Physics", V22, semiconductors, Landolt-Bornstein.

Chapter 5

DIFFRACTION FROM RANDOM ALLOYS

This paper is published in Physical Review B. Reference: M. F. Thorpe, J. S. Chung and Y. Cai, Phys. Rev. B**43**, 8282(1991)

5.1 INTRODUCTION

The elastic scattering (diffraction) from a random alloy is a complex problem that has received considerable attention over the years. In this chapter, we describe the diffraction pattern caused by the correlated static displacements from an underlying crystalline structure. We find a set of Bragg peaks (determined by the average lattice), modified by an appropriate Debye-Waller factor. Each Bragg peak has some diffuse (Huang) scattering associated with it. To quote from Huang,[1] "Considering a crystal lattice formed of randomly distributed atoms of two kinds mixed in comparable proportions, it must obviously be extremely difficult to describe qualitatively the distorted configuration", and he goes on to consider the case of isolated impurities. Modern analytic techniques and computer simulations now allow us to treat the concentrated alloy. Although the example worked through here is simple, we have

found it instructive and we hope the reader will too.

We use the model alloy of Thorpe and Garboczi[2] (henceforth referred to as I) for an $A_{1-x}B_x$ alloy. This consists of a crystalline lattice containing two kinds of bonds, A and B which are randomly positioned throughout the lattice with probabilities $1-x$ and x respectively. The static structure is obtained by minimizing the energy associated with the potential

$$V = \frac{K}{2}\sum_{ij}(|\vec{R}_i - \vec{R}_j| - L_{ij}^0)^2 \tag{5.1}$$

Here L_{ij}^0 can take on the two values L_A^0 and L_B^0 with probability $1-x$ and x respectively. The summation goes over all nearest neighbor bonds ij and the angular brackets denote that nearest neighbor bonds are only counted once. The vector $\vec{R}_i$ goes to the site i at the end of the bond ij from some (arbitrary) origin. The potential (5.1) can be minimized with respect to the $\vec{R}_i$ to give,

$$0 = \sum_{j}[(\vec{R}_i - \vec{R}_j) - L_{ij}^0\hat{R}_{ij}] \tag{5.2}$$

Here $\hat{R}_{ij}$ is a unit vector along the relaxed bond direction. These equations determine the equilibrium positions of all the sites, as described fully in I. An example is shown in Fig.5.1, which can be visualized as static concentration waves of all wavelengths freezing out from a perfect crystalline lattice. We will take all the spring constants to be equal in this note as it simplifies the analytic treatment as discussed in I, and does not qualitatively effect the result.

5.2 COMPUTER SIMULATIONS

We have used an FCC lattice rather than the triangular net as in I. This is because of the well known instability of two-dimensional lattice ordering to fluctuations.[3] While this does not effect quantities like the mean bond length, it does have a profound effect on the diffraction pattern, which is very sensitive to long range order. The general

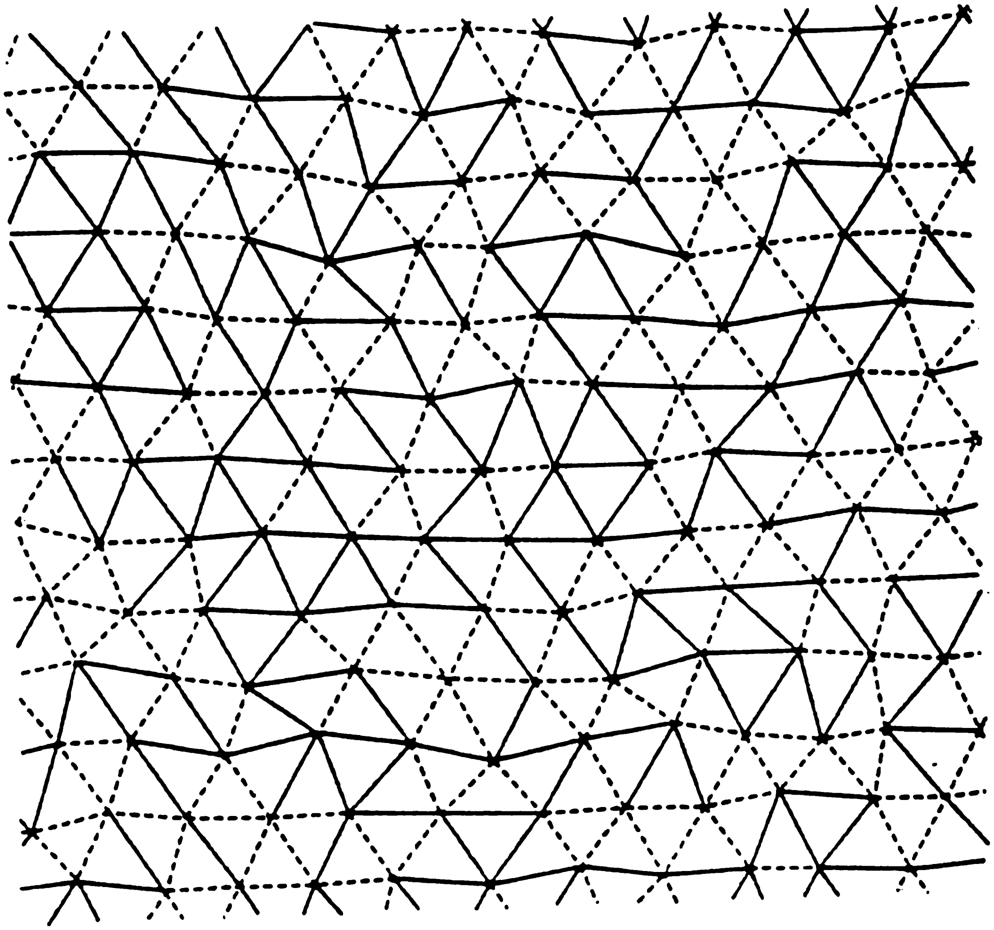

Figure 5.1: A piece of a relaxed triangular network. This figure is reproduced from I. The short bonds are shown as dashes and the long bonds by solid lines. The sample shown has equal numbers of short and long bonds ($x = 0.5$) and the natural length of the long bonds is 30% greater than the natural length of the short bonds. The two spring constants are equal.

formalism of I, which is geared towards the calculation of local distances, applies equally well in any dimension. We have used $M \times M \times M$ FCC samples with periodic boundary conditions containing $N = 4M = 32,000$ atoms and $24M = 192,000$ bonds, which were randomly assigned to be A or B with probability $1 - x$ or x respectively. The simulation program, which uses a variant of the conjugate gradient method,[4] adjusted the positions of all the atoms and the size of the supercell to minimize the energy. The simulation was terminated when the energy agreed with the exact energy $3Nx(1-x)(L_B^0 - L_A^0)^2/2$ as given in I, to better than 1%. The supercell was kept strictly cubic to facilitate the analysis. The mean bond length $\langle L \rangle$, which is proportional to the sample size, is given by Vegard's law as discussed in I

$$\langle L \rangle = (1-x)L_A^0 + xL_B^0 \tag{5.3}$$

The diffraction pattern was computed from the relaxed coordinates using

$$I(\mathbf{q}) = \frac{1}{N} |\sum_i \exp(i\mathbf{q} \cdot \mathbf{R}_i)|^2 \tag{5.4}$$

where $I(\mathbf{q})$ is the scattered intensity per site.

5.2.1 Bragg Scattering

The diffraction pattern is dominated by the Bragg peaks shown in Fig. 5.2, for different directions in reciprocal space, and for different values of the length mismatch parameter $(L_B^0 - L_A^0)/\bar{L}$. The Bragg peaks are Kronecker delta functions, rather than Dirac delta functions, because of the finite size of the supercell. We have taken out a factor N from the computed intensity, to make the connection between the computed Kronecker delta functions and the calculated Dirac delta functions used in the next section. These Bragg peaks have no width and are associated with a single superlattice point in reciprocal space. It can be seen that the diffracted intensity falls off as a Gaussian in all three cubic directions. This is certainly what would be naively expected, and is similar to the situation with dynamic disorder caused by phonons

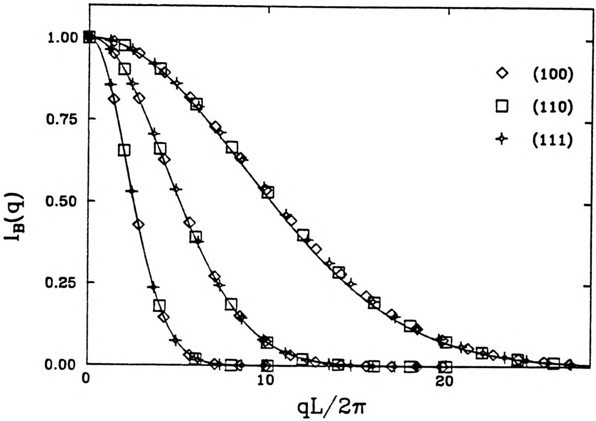

Figure 5.2: The Bragg scattering for a random FCC alloy with two kinds of bond lengths, similar to that shown in Fig. 5.1. The length mismatch parameters are 4% (upper curve), 8% (middle curve) and 16% (lower curve) and the concentration $x = 0.5$. The symbols indicate the different cubic directions and the solid line is the Debye-Waller factor calculated in the text. The intensity is averaged over the different equivalent directions of a single $20 \times 20 \times 20$ cubic sample containing 32,000 atoms. The solid line is the theory (5.8) using the Debye-Waller factor (5.12).

that produces a Debye-Waller factor,[5] although the static case requires handling in a slightly different way.

5.2.2 Huang Scattering

The computed background is artificially reduced by a factor N with respect to the Bragg peaks because of the Kronecker delta functions caused by the supercell, and therefore cannot be seen in Fig. 5.2. The background scattering is shown in Figs. 5.3 and 5.4 for different values of the length mismatch parameter. The noise in the results was greater than for the Bragg peaks and so we have averaged over 9 samples. The scattered intensity is shown at the $2M-1=39$ superlattice points between pairs of Bragg peaks in the 100 direction. This Huang scattering[1] is seen to be largest at the Bragg peaks in the 100 direction. Similar results are found around all the Bragg peaks.

5.3 THEORY

It is convenient to separate the scattering into two parts; the Bragg scattering $I_B(\mathbf{q})$, and the remainder that we will refer to as the Huang scattering $I_H(\mathbf{q})$, so that

$$I(\mathbf{q}) = I_B(\mathbf{q}) + I_H(\mathbf{q}) \tag{5.5}$$

5.3.1 Bragg Scattering

The cross section (5.4) can be conveniently rewritten as

$$I(\mathbf{q}) = \frac{1}{N}\sum_{i,j} \exp[i\mathbf{q}\cdot\mathbf{R}^0_{ij}]\langle\exp[i\mathbf{q}\cdot\mathbf{u}_{ij}]\rangle \tag{5.6}$$

where $\mathbf{R}_i = \mathbf{R}^0_i + \mathbf{u}_i$, and the $\mathbf{R}^0_i$ define the underlying mean lattice and the $\mathbf{u}_i$ represent the (small) displacements from it. The angular brackets $\langle ... \rangle$ in (5.6) denote an ensemble average over different static configurations. The size of the mean lattice

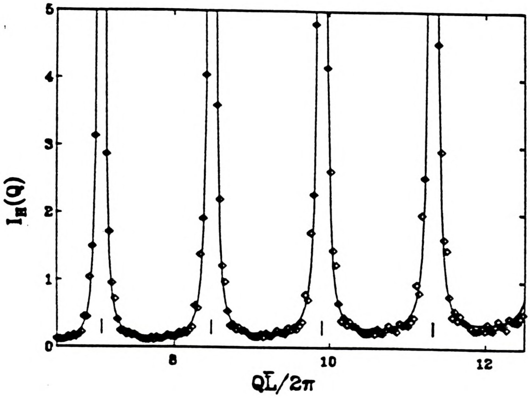

Figure 5.3: The Huang scattering in the 100 direction for a random *FCC* alloy with two kinds of bond lengths. The length mismatch parameter is 4% and the concentration $x = 0.5$. This figure is a magnified version of the Bragg peaks shown in Fig. 5.2 and is averaged over the different 100 directions for nine $20 \times 20 \times 20$ cubic samples, each containing 32,000 atoms. The solid line is the theory (5.16) given in the text and the vertical bars mark the positions of the Bragg peaks shown in Fig. 5.2.

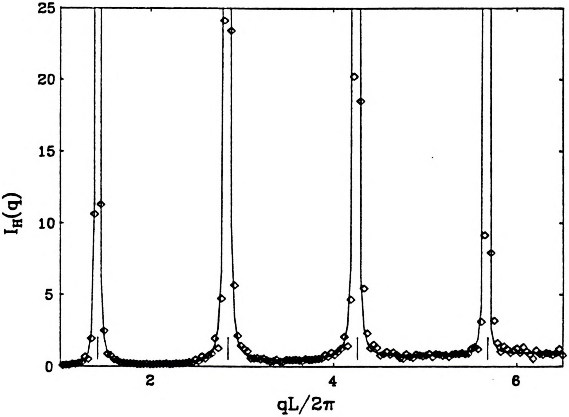

Figure 5.4: The same as Fig. 5.3, except that the lattice mismatch parameter has been increased to 16%.

is given by Vegard's law (5.3). Inasmuch as the diffraction pattern_is dominated by the Bragg peaks as shown in Fig. 5.2, it is suggestive that we should make the conventional approximation,[5]

$$\langle \exp(i\mathbf{q}\cdot\mathbf{u}_{ij})\rangle = \langle \exp(i\mathbf{q}\cdot\mathbf{u}_i)\rangle\langle \exp(-i\mathbf{q}\cdot\mathbf{u}_j)\rangle = \exp(-2W) \qquad (5.7)$$

which assumes that the displacements at each site are independent, as with "frozen Einstein oscillators", where the displacement at each site is chosen independently. This is manifestly not the case here, as we will discuss later. Nevertheless the assumption (5.7) leads to excellent answers. Inserting (5.7) into (5.6), we find that,

$$I_B(\mathbf{q}) = \exp(-2W)\delta(\mathbf{q}-\mathbf{g}) \qquad (5.8)$$

where $\mathbf{g} = (\sqrt{2}/\bar{L})(n_1, n_2, n_3)$ with the integers n_1 ,n_2 ,n_3 either all even or all odd, are the reciprocal lattice vectors for the FCC lattice with a mean lattice spacing $\bar{L}$ given by Vegard's law (5.3).

In I, it was shown that the displacements $\mathbf{u}_i$, could be expanded in terms of the Green functions $\mathbf{G}_{ij}$ of the perfect lattice, the various natural bond lengths L^0_{ij} , and the nearest neighbor vector directions $\hat{\mathbf{R}}_{ij}$ of the perfect lattice

$$\mathbf{u}_i = K\sum_{l,m}\mathbf{G}_{il}\cdot\hat{\mathbf{R}}_{lm}(L^0_{lm} - \langle L\rangle). \qquad (5.9)$$

After some manipulation, of the kind discussed in I and involving doing the statistical averaging[6] over the (random) bonds, we may write the full Debye- Waller factor as

$$W = -\frac{1}{2}\sum_{l,m}\ln\{1 - 4x(1-x)\sin^2[\frac{1}{2}K\mathbf{q}\cdot\mathbf{G}_{il}\cdot\hat{\mathbf{R}}_{lm}(\mathrm{L}^0_B - L^0_A)]\}. \qquad (5.10)$$

This would be complex to evaluate numerically as all the lattice Green functions $\mathbf{G}_{il}$ must be used in the summation. However for reasonable values of the length mismatch parameter $(L^0_B - L^0_A)/\bar{L}$, the argument of the sine term in (5.10) is small and so to leading order

$$W \;=\; \frac{1}{2}K^2x(1-x)(L^0_B - L^0_A)^2\sum_{l,m}(\mathbf{q}\cdot\mathbf{G}_{il}\cdot\hat{\mathbf{R}}_{lm})^2$$

$$= \frac{1}{2}\langle(\mathbf{q}\cdot\mathbf{u})^2\rangle = \frac{q^2}{6}\langle u^2\rangle. \qquad (5.11)$$

which is the conventional Debye-Waller factor. We have dropped the site label from $\langle u^2\rangle$ as it is the same for all sites. After some manipulation, we find the result,

$$W = \frac{q^2}{6}\langle u^2\rangle = \frac{K}{2}q^2x(1-x)(L_B^0 - L_A^0)^2\langle 1/\omega^2\rangle. \qquad (5.12)$$

where $\langle 1/\omega^2\rangle$ is the mean inverse squared frequency of the FCC lattice with nearest neighbor springs K. The "phonon" band[7] is defined by the frequencies $0 < \omega^2 < 8K$, and we find by numerical integration that $\langle 1/\omega^2\rangle = 2.38K$. Thus the Debye-Waller factor can be regarded as known through (5.12).

5.3.2 Huang Scattering

By subtracting the Bragg scattering (5.8), from the total scattering as (5.4), we find that the Huang scattering[1] [8][9] is given by

$$I_H(\mathbf{q}) = \exp(-2W)\frac{1}{N}\sum_{i,j}\exp(i\mathbf{q}\cdot\mathbf{R}_{ij}^0)[\langle\exp(i\mathbf{q}\cdot\mathbf{u}_{ij})\rangle\exp(2W) - 1]. \qquad (5.13)$$

This is as hard as the original expression to evaluate, and so we approximate (5.13) by expanding the terms in the final square bracket. The approximation (5.7) is replaced by the improved approximation

$$\begin{aligned} \langle\exp(i\mathbf{q}\cdot\mathbf{u}_{ij}\rangle &= \exp -2w[1 + \langle(\mathbf{q}\cdot\mathbf{u}_i\rangle\langle(\mathbf{q}\cdot\mathbf{u}_j\rangle + O(q^4)] \qquad for \;\; i \neq j; \\ &= 1 \qquad for \;\; i = j. \quad (5.14) \end{aligned}$$

Note that because of inversion symmetry, the correction terms to (5.14) are $O(q^4)$. Doing the summations, we are led to the result[6]

$$I_H(\mathbf{q}) \;\approx\; 1 - (1+2W)\exp(-2W) + \exp(-2W)\frac{1}{N}\sum_{i,j}\exp(i\mathbf{q}\cdot\mathbf{R}_{ij}^0)\langle(\mathbf{q}\cdot\mathbf{u}_i)(\mathbf{q}\cdot\mathbf{u}_j)\rangle$$

$$= \quad 1 - (1 + 2W)\exp(-2W) + \exp(-2W)\langle(\mathbf{q}\cdot\mathbf{u_q})(\mathbf{q}\cdot\mathbf{u_{-q}})\rangle$$

$$= \quad [1 - (1 + 2W)\exp(-2W)] - \exp(-2W)Kx(1-x)(L^0_B - L^0_A)\mathbf{q}\cdot\mathbf{G}(\mathbf{q})\cdot\mathbf{q}. \tag{5.15}$$

Here $\mathbf{u_q}$ is the Fourier transform of the displacements $\mathbf{u}_i$. The Green function $\mathbf{G}(\mathbf{q})$ is the Fourier transform of $\mathbf{G}_{ij}$, and diverges at small q as q^2 . The term $[1-(1+2W)\exp(-2W)]$ in (5.15) is small and accounts for most of the background away from the Bragg peaks. For this reason, it is important to include the higher order diagonal terms, even though the higher order off-diagonal terms are neglected in (5.14). The last term in the expression (5.15) does not lead to large scattering near the origin as the q^{-2} divergence is cancelled by the q^2 factor in (5.15). However this divergence remains at all Bragg peaks. Note that this divergence is integrable because of the phase space factor in three dimensions. We have lumped together all the non-Bragg terms into (5.15) for convenience, although they could have been separated into a diffuse background term (the first term in square brackets) and the divergent scattering (last term). The result (5.15) along the principal cubic directions becomes

$$I_H(\mathbf{q}) = 1 - (1+2W)\exp(-2W) + \exp(-2W)x(1-x)[q(L^0_B - L^0_A)]^2/\sin^2\phi. \tag{5.16}$$

where $\phi = q\bar{L}/\sqrt{8}$ in the 100 direction and $\phi = q\bar{L}/\sqrt{6}$ in the 111 direction. The divergences in (5.16) occur at the Bragg peaks ($\phi = n\pi$, where n is any non-zero integer). We show the results along the 100 direction in Figs. 5.3 and 5.4 for different values of the length mismatch parameter $(L^0_B - L^0_A)/\bar{L}$. Although the Huang scattering falls away from the Bragg peak as $(g-q)^2$ in all directions, it is not isotropic around the Bragg peak as can seen from (5.15). In some directions, as those shown in Figs. 5.3 and 5.4, the coupling is entirely to the longitudinal phonon modes, while in others it is entirely to the tranverse modes. In an arbitary direction, the coupling is to both kinds of mode. This is quite different from the scattering from single isolated site impurities,[8] where the spherically symmetric strain field leads to only a longitudinal coupling. The difference arises because we are substituting bonds and not sites in our model system. The analysis can be extended to the more complex of concentrated site substitution.[17]

To obtain the total integrated strength, we make the rough assumption that the scattering is isotropic around each Bragg peak, and integrate the last term in (5.16) inside a sphere of radius equal to half the spacing to the nearest Bragg peak in the same principal direction. This leads to the ratio of intensities

$$I_H(g)/I_B(g) = Ax(1-x)[g(L_B^0 - L_A^0)]^2 \tag{5.17}$$

where A is a constant that is ~ 0.1. This is to be expected from sum rule considerations. If the length mismatch parameter $(L_B^0 - L_A^0)/\bar{L}$ is increased slowly from zero, then the intensity of a Bragg peak is decreased by a factor $\exp(-2W) = 1 - 2W$, and the intensity $2W = x(1-x)[g(L_B^0 - L_A^0)]K\langle 1/\omega^2\rangle = 0.42x(1-x)[g(L_B^0 - L_A^0)]^2$ appears at the base of the Bragg peak as the Huang scattering. These estimates are in agreement apart from a numerical factor of about 4, due to the rough integration that was done to obtain (5.17). Note that the background term $1-(1+2W)\exp(-2W)$ in (5.16) is $O(q^4)$. The q dependence of the Huang scattering $g^2\exp(-\langle u^2\rangle g^2/3)$ means that it is absolute maximum at $g^2 = 3/\langle u^2\rangle$, when the Debye-Waller factor is down by a factor $e_{-1} = 0.368$. However, relative to the Bragg peak, the Huang scattering keeps on increasing in intensity as q increases as given in (5.15).

The $(g-q)^{-2}$ divergence of the Huang scattering at the Bragg peaks is due entirely to the correlations between the displacements $\mathbf{u}_i$. When the displacements at each site are independent, as with "frozen Einstein oscillators", correcting the expression (5.7) for the self terms, leads to an intensity $1-\exp(-2W)$ for the Huang scattering which is just a non-divergent background.

5.4 RESULTS

To make a direct check of the result (5.12), we have obtained $\langle u^2 \rangle$ from the simulation results. To do this is was necessary to superimpose and position a perfect FCC grid, of the appropriate size as given by (5.3). The positioning was done by minimizing $\sum_i u_i^2$ with respect to rigid motions of the grid to obtain the best registry, and is accomplished by using the conjugate gradient method. The results are shown in Fig. 5.5, where the agreement with the parabolic composition dependence $x(1-x)$ and overall magnitude of $\langle u^2 \rangle$ is verified. Note that there are no adjustable parameters in (5.12), as we have calculated the magnitude via the inverse second frequency moment of the FCC lattice.

5.4.1 Bragg Scattering

We show the result (5.8) for the Bragg scattering $I_B(\mathbf{q})$ in Figs. 5.2 and 5.6, where the Debye-Waller factor is obtained from (5.12). The agreement, involving a total more than 50 separate Bragg peaks, is very good. Some simulation points lie slightly above the theoretical Debye-Waller factor, especially at intermediate q values for a 4% mismatch, as can also be seen in Fig. 5.5. We have tested the size dependence of our results by varying the size of the supercell and find no significant changes. This small discrepancy at intermediate q may be real and due to higher order terms in q in the full Debye-Waller factor as written in (5.10). We note that we have no higher order anharmonic terms in our potential (5.1) which would also modify the Debye-Waller factor.[11] We have computed the displacement- displacement correlation function for nearest neighbor sites, with the result[12] that $\langle \mathbf{u}_i \cdot \mathbf{u}_j \rangle / \langle u^2 \rangle = 0.08$ and $3\langle (\mathbf{u}_i \cdot \hat{\mathbf{R}}_{ij})(\mathbf{u}_j \cdot \hat{\mathbf{R}}_{ij}) \rangle / \langle u^2 \rangle = 0.40$. These two ratios are obtained for all concentrations x and for all values of the length mismatch parameter $(L_B^0 - L_A^0)/\bar{L}$. While these correlations do fall off rapidly with distance, in no sense are the local displacements associated with the static concentration wave uncorrelated and insignificant. Nevertheless, our results

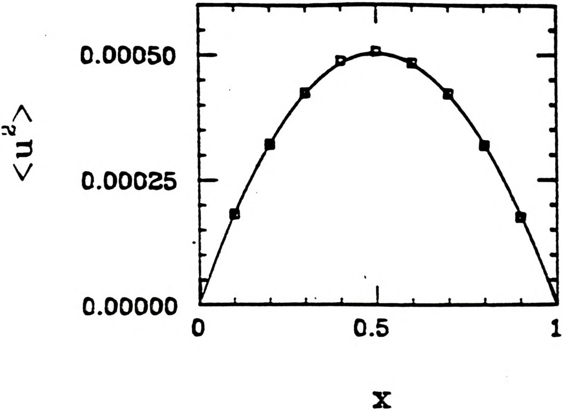

Figure 5.5: Illustrating the parabolic dependence of the mean squared displacement $\langle u^2 \rangle$ for a random FCC alloy as a function of the composition. The squares are from the computer simulation and the solid line is the theoretical result (5.12). The natural bond lengths are 0.98 and 1.02, so that the length mismatch parameter is 4%.

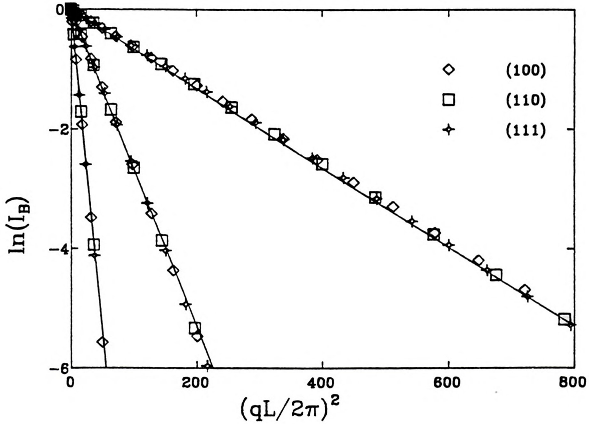

Figure 5.6: The same as Fig. 5.2, but shown as the logarithm of the Bragg intensities plotted against the square of the wavevector. This is often referred to as a Wilson plot when used to analyze experimental data.

show that these correlations have no effect on the Bragg Scattering.

5.4.2 Huang Scattering

We show the result (5.16) for the Huang scattering $I_H(\mathbf{q})$ in Figs. 5.3 and 5.4 for two different values of the lattice mismatch parameter. It can be seen that the agreement between theory and the simulation results is very good, considering that the approximation (5.14) has been made in the theory. This fit is equally good at all q values, except that at large q the scattering is weak due to the Debye-Waller factor (see Fig. 5.2) and the simulations become noisy. This result pleasantly surprised us as the approximation (5.14) is only good to $O(q^2)$ in the off-diagonal terms. It appears that the higher order off-diagonal terms are insignificant and non- divergent.

There is no evidence for any rounding of the peak, as would occur if the $(g-q)^{-2}$ divergence were associated with the wings of a Lorentzian. Equally, there is also no evidence for additional divergent terms as might have occurred from the higher order terms ignored in the approximation (5.14). It might have been expected that differences might have appeared when the lattice misnmatch parameter was as large as 16%, but the comparison between theory and simulation is about as good in Fig. 5.4 as in Fig. 5.3.

5.5 DISCUSSION

As well as the static effects considered here, the thermal vibrations about the distorted static lattice, such as shown in Fig. 5.1, also contribute to the observed scattering. The cross section in (5.6) is modified to give

$$I(q) = \frac{1}{N}\sum_{ij} \exp(i\mathbf{q}\cdot\mathbf{R}^0_{ij})\langle\exp(i\mathbf{q}\cdot\mathbf{u}_{ij})\rangle\langle\exp(i\mathbf{q}\cdot\mathbf{u}^T_{ij})\rangle_T \tag{5.18}$$

where $\mathbf{R}_i = \mathbf{R}^0_i + \mathbf{u}_i + \mathbf{u}^T_i$ and the $\mathbf{u}^T_i$ are the thermal displacements. The thermal average[13] $\langle ... \rangle_T$ is independent of the static average, when both the static and dy-

namic displacements are controlled by the potential (5.1). The approximation (5.7), when applied to the expression (5.18), means that the total Debye-Waller factor is a product of the static part discussed previously, and a thermal part which has the form[13] $\exp(-2W)$ so that $W \rightarrow W + W_T$, where

$$W_T = \langle (u^T)^2 \rangle_T = \frac{hq^2}{2M} \langle [n(\omega) + \frac{1}{2}]/\omega \rangle \tag{5.19}$$

and $n(\omega) = [\exp(h\omega/k_B T) + 1]^{-1}$ is the Planck function. All the expressions in the previous sections must be modified using the replacement (5.19). At low temperatures the thermal part of (5.19) involves only the zero point vibrations, which are small except for very light atoms. At high temperatures (greater than the Debye temperature), we obtain the classical result

$$W_T = \frac{k_B T}{2M} \langle 1/\omega^2 \rangle \tag{5.20}$$

This is the same $\langle 1/\omega^2 \rangle$ that occurs in the static Debye-Waller factor (5.12), except that the mass M is relevant. For the static distortions, the mass was irrelevant and set equal to 1. For the FCC lattice the phonon band is now defined by $0 < \omega^2 < 8K/M$ so that the thermal Debye-Waller factor (5.20) is larger than the static Debye-Waller factor (5.12) if

$$k_B T > x(1-x) K (L_B^0 - L_A^0)^2 \tag{5.21}$$

which compares the thermal energy $k_B T$ to the potential energy associated with a displacement $L_B^0 - L_A^0$, weighted with the usual alloy factor $x(1-x)$. We note from I that the strain energy per bond $\epsilon = Kx(1-x)(L_B^0 - L_A^0)/4$ so that (5.21) is equivalent to $k_B T > 4\epsilon$. Note that the condition (5.21) is quite general and not lattice specific as all the lattice effects occur through the common factor $\langle 1/\omega^2 \rangle$.

In thermal neutron scattering, the neutron has a low energy so that the "transit time" for the neutron is sufficiently long that it sees the time averaged lattice. The phonon motion leads to Bragg scattering modified by a Debye-Waller factor $exp[-2(W + W_T)]$, as discussed in the previous paragraph. The term invoving

$\langle(\mathbf{q}\cdot\mathbf{u}_i^T)(\mathbf{q}\cdot\mathbf{u}_j^T)\rangle_T$ that arises when (5.18) is subject to the approximation (5.14), leads to one phonon inelastic scattering. Thus there is no thermal equivalent equivalent of Huang scattering and all the $(g-q)^2$ scattering around the base of the Bragg peaks can be attributed to Huang scattering from the static distortions.

In X-ray scattering, the high energy of the X-ray leads to a fast "transit time" so that the structure is effectively frozen. The X-ray scattering is an average over all such frozen structures, which means that the diffraction spectrum is an integral over all frequencies. The quantity W is replaced by $W + W_T + W_F$, where W_T is the thermal part discussed in the previous paragraph and W_F is the contribution from the atomic form factor. The Bragg scattering is still modified by the Debye-Waller factor. The term involving $\langle(\mathbf{q}\cdot\mathbf{u}_i^T)(\mathbf{q}\cdot\mathbf{u}_j^T)\rangle_T$ from applying the approximation (5.14) to the thermal part of (5.18), leads to thermal diffuse scattering; the divergent piece of which has the form[13]

$$e^{-2W}\langle(\mathbf{q}\cdot\mathbf{u}_q^T)(\mathbf{q}\cdot\mathbf{u}_{-q}^T)\rangle_T = -e^{-2W}\frac{h}{\pi}\int_{-\infty}^{\infty}\frac{Im[\mathbf{q}\cdot\mathbf{G}(\mathbf{q},\omega)\cdot\mathbf{q}]}{1-\exp(-h\omega/k_BT)}d\omega \tag{5.22}$$

At low temperatures (5.22) diverges like $|g-q|$ around the Bragg peaks and is generally expected to be weak and masked by the Huang scattering. At high temperatures (compared to the Debye temperature), the thermal diffuse scattering (5.22) becomes

$$-\,e^{-2W}k_BT\;\mathbf{q}\cdot\mathbf{G}(\mathbf{q},\omega=0)\cdot\mathbf{q}/M \tag{5.23}$$

This has the same form as (5.15) with the two Green functions being identical except for a factor M, so that the thermal diffuse scattering is like the Huang scattering shown in Fig. 5.3, including the background terms. The condition that the divergent $(g-q)^{-2}$ thermal diffuse scattering is greater than the Huang scattering is again (5.21).

5.6 CONCLUSION

We have shown that the elastic scattering from a model alloy consists of two parts; the Bragg scattering and the Huang scattering. The Bragg scattering is modulated by a

Debye-Waller factor and the divergent Huang scattering comes entirely from the second order displacement-displacement correlations. Our central approximation (5.14) has been shown to essentially numerically exact, and can be used with confidence in more complex alloys and geometries.

Bibliography

[1] K. Huang, Proc. Roy. Soc. A190, 102 (1947).

[2] M. F. Thorpe and E. J. Garboczi, Phys. Rev. B**42**,8405(1990)

[3] See for example, R. M. White and T. H. Geballe in Solid State Physics, (Academic Press, New York, 1979) Vol. 15, page 45.

[4] W. H. Press, B. P. Flannery, S. A. Teukolsky and W. T. Vetterling, Numerical Recipes (Cambridge University Press, Cambridge, England, 1986) page 301.

[5] See for example, N. W. Mermin and N. D. Ashcroft, Solid State Physics, (Saunders College, Philadelphia, 1976), page 790.

[6] The most important result from the statistical averaging that we use in this note is $\langle u_{i\alpha} u_{j\beta} \rangle = -Kx(1-x)(L_B^0 - L_A^0)^2 G_{ij}^{\alpha\beta}$. All the lattice Green functions G used in this chapter are evaluated in the static limit. The Green function for the FCC latice is defined as the inverse of the dynamical matrix and is given in E. J. Garboczi and M. F. Thorpe, Phys. Rev. B32, 4513 (1985).

[7] L. von Heimendahl and M. F. Thorpe, J. Phys. F L87 (1975). Note that the masses of the atoms are irrelevant for statics and we set them equal to unity.

[8] M. A. Krivoglaz, The Theory of X-ray and Thermal Neutron scattering from Real Crystals (Plenum, New York, 1969).

[9] H. E. Cook, J. Phys. Chem. Solids, 30, 1097 (1969); W. Fenzl and S. C. Moss, J. Phys. F17, 1285 (1986) and references contained therein.

[10] A. J. C. Wilson, Nature 150, 152 (1942).

[11] A. A. Maradudin and A. E. Fine, Phys. Rev. 128, 2589 (1962)

[12] Using the result in I for the total strain energy, it can be shown that the ratio $3\langle(\mathbf{u}_i \cdot \hat{\mathbf{R}}_{ij})(\mathbf{u}_j \cdot \hat{\mathbf{R}}_{ij})\rangle / \langle u^2 \rangle = 1 - \frac{1}{2}(1 - a^*)/\langle K/\omega^2 \rangle = 0.40$ for the FCC lattice where $a^* = 1/2$. These ratios are independent of the concentration x and the length mismatch parameter $(L_B^0 - L_A^0)/\bar{L}$.

[13] The required thermal averages are given by $\langle u_{i\alpha}^T u_{j\beta}^T = -\frac{h}{\pi} \int_{-\infty}^{\infty} ImG_{ij}^{\alpha\beta}(\omega)/[1 - \exp(-h\omega/k_B T)] d\omega$, as discussed for example by M. F. Thorpe, Phys. Rev. B8, 5352 (1973).

Chapter 6

TWO DIMENSIONAL MIXED CRYSTAL

This paper is published in Physical Review B. Reference: M. F. Thorpe and Y. Cai, Phys. Rev. B**43**, 11019(1991)

6.1 INTRODUCTION

The melting transition has been extensively studied in single component two dimensional systems.[1]-[5] It is known that thermal fluctuations destroy the long range positional order at any finite temperature. This produces a phase with quasi-long-range-order that is characterized by a power law decay in the position-position correlation function at all temperatures up to some temperature T_1. This phase has power-law peaks in the diffraction pattern, where the Bragg peaks would have been. However the long range orientational order remains all the way up to T_1 above which the angular correlations decay algebraically, in the *hexatic* phase.[5] Finally at some higher temperature T_2, melting is completed, and both the positional and angular correlations fall off exponentially.

In this paper, we investigate the idea that the size-mismatch between the two components in a two dimensional random alloy $A_{1-x}B_x$ also destroys the long range positional order in an analogous way to the thermal disorder in a single component system, as previously discussed by Nelson.[5] We set up a triangular network with nearest neighbor forces with spring constant K and natural spring lengths L_A^0 and L_B^0. The topology of this network cannot be changed and every atom always has the same six nearest neighbors so that the disorder is quenched in. Nevertheless, the long-range positional order is destroyed, even though the fixed topology prohibits the formation of either *disclinations* or *dislocations*.[5] Our approach is analogous to the spin wave description of the thermal disordering of the classical XY model.[6],[7]

We show that it is possible to define an effective *temperature* T_D associated with the disorder via,

$$k_B T_D = Kx(1-x)(L_B^0 - L_A^0)^2 \tag{6.1}$$

where $L_B^0 - L_A^0$ is the length mismatch. The triangular lattice is shown in Figs.6.1 and 6.2, with two kinds of *bonds* A and B that are randomly located in the lattice with probabilities $1-x$ and x respectively. This mathematical simplification to *bond* disorder rather than *site* disorder does not qualitatively effect any of our results. For example, if the lattice is made up of randomly positioned A and B *sites* with probabilities $1-x$ and x respectively, then the disorder temperature in Eq. (6.1) is replaced by

$$k_B T_D = \frac{1}{2} Kx(1-x)(L_{BB}^0 - L_{AA}^0)^2 \tag{6.2}$$

where L_{BB}^0 and L_{AA}^0 are the lengths of the AA and BB bonds, and the AB bonds have natural lengths $L_{AB}^0 = \frac{1}{2}(L_{BB}^0 + L_{AA}^0)$.[8] Other models for the length disorder would lead to more complex expressions for T_D.

In the next section, we recall that the short range properties are entirely conventional and similar to those in higher dimensions. In section **6.3**, we show that the decay of the positional correlations is controlled by the parameter η, which leads to power law peaks in the diffraction pattern if $\eta < 2$, with *no* peaks if $\eta > 2$. In section **6.4** it is shown that the angular correlations do display long range order which is cal-

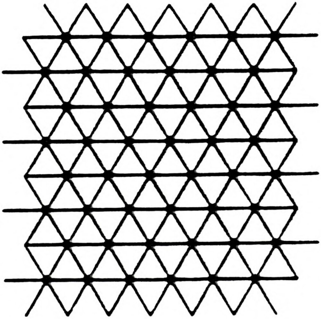

Figure 6.1:

The regular triangular lattice.

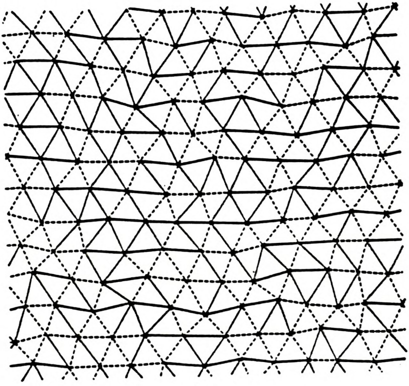

Figure 6.2: The relaxed triangular lattice with two different kinds of bonds with different natural lengths. The concentration $x = 0.5$; the shorter bonds are shown as dashed lines, and the longer bonds as solid lines. The length mismatch parameter $(L_B^0 - L_A^0)/\langle L \rangle$ is 30%.

culated. Throughout this paper we compare our results with computer simulations. In sections **6.3** and **6.4**, we show that the positional order is finally destroyed when the lattice *pleats.*[9] The pleating is not described by our linearized approach, and is brought about by the fixed topology that prevents a more reasonable *disordering* of the lattice at a smaller length mismatch. Nevertheless, the pleating is of some interest in its own right as it relates to the crumpling transition;[10] the difference being that no motion out of the plane is permitted in *pleating* whereas it is permitted in *crumpling.* We stress that the pleating transition is unphysical, because of the absence of any repulsive forces at short distances in our model, as well as the imposition of a fixed topology. The pleating transition takes place at a length mismatch of about 50% which is way beyond the region of physical interest as no random solid solutions can tolerate length mismatches of more than about 15%.[11] In section **6.5** we discuss finite size scaling and in the conclusions, we explore ways in which the model needs to be modified to give a more realistic description of size-mismatch effects in two dimensions.

6.2 SHORT RANGE PROPERTIES

The triangular network is described by a potential

$$V = \frac{K}{2}\sum_{\langle ij\rangle}(L_{ij} - L_{ij}^0)^2 \tag{6.3}$$

where K is the force constant between nearest neighbor atoms, denoted in the summation by the angular brackets. The length of the bond **ij** in the network is L_{ij} and the natural (unstrained) length of this bond is L_{ij}^0. The bonds are chosen randomly on a triangular network to be either type A with probability $1 - x$ or type B with probability x.

The short range properties of this model have been well studied and are qualitatively the same in two and three dimensions,[9],[12] as summarized below. The network is relaxed so as to minimize the strain energy. This gives fairly broad distributions of the A and B bond lengths, from which the mean lengths are given by,[9]

$$\langle L_A \rangle = L_A^0 + \frac{x}{3}(L_B^0 - L_A^0)$$

$$\langle L_B \rangle = L_B^0 - \frac{1-x}{3}(L_B^0 - L_A^0) \tag{6.4}$$

where the angular brackets $\langle ... \rangle$ denote an ensemble average. The mean overall length, which determines the size of the sample obeys Vegard's law[13]

$$\begin{aligned} \langle L \rangle &\equiv (1-x)\langle L_A \rangle + x\langle L_B \rangle \\ &= (1-x)L_A^0 + xL_B^0. \end{aligned} \tag{6.5}$$

The widths of the A and B distributions are equal and given by

$$\begin{aligned} \langle L_A^2 \rangle - \langle L_A \rangle^2 &= \langle L_B^2 \rangle - \langle L_B \rangle^2 \\ &= \frac{2}{9}x(1-x)(L_B^0 - L_A^0)^2 \end{aligned} \tag{6.6}$$

The total strain energy E_s can also be found, and is given by

$$\begin{aligned} \frac{E_s}{N} &= \frac{1}{2}Kx(1-x)(L_B^0 - L_A^0)^2 \\ &= \frac{1}{2}k_B T_D \end{aligned} \tag{6.7}$$

where N is the number of sites and the disorder temperature T_D has been previously defined in Eq. (6.1).

6.3 DIFFRACTION PATTERN

In three dimensions, the model (6.3) on say a face centered cubic lattice, leads to conventional Bragg peaks and associated Huang scattering in the diffraction pattern.[14],[12].

The situation is very different in two dimensions. Assuming the scattering length of all atoms to be *unity*, the elastic scattering cross section for neutrons can be written as

$$I(\mathbf{Q}) = \frac{1}{N}\sum_{ij} e^{i\mathbf{Q}\cdot\mathbf{R}^{0}_{ij}}\langle e^{i\mathbf{Q}\cdot\mathbf{u}_{ij}}\rangle. \tag{6.8}$$

where $\mathbf{Q}$ is the momentum transfer. In this equation, $\mathbf{R}^0_i$ is the equilibrium position of atom $\mathbf{i}$, and the average displacement $\langle \mathbf{u}_i \rangle$ is required to be zero to define a *reference lattice* with nearest neighbor distance $a = \langle L \rangle$ as given by Eq. (5). The approximation for the average needed to evaluate (6.8), up to terms $O(Q^4)$ is,

$$\langle e^{i\mathbf{Q}\cdot\mathbf{u}_{ij}}\rangle = C_{\mathbf{Q}}(R) \simeq e^{-\frac{1}{2}\langle(\mathbf{Q}\cdot\mathbf{u}_{ij})^2\rangle} \tag{6.9}$$

This is defined as the density-density correlation function $C_{\mathbf{Q}}(R)$, where R is distance between sites $\mathbf{i}$ and $\mathbf{j}$. From our previous work[9],[15]

$$\langle \mathbf{u}_i \mathbf{u}_j \rangle = -Kx(1-x)(L^0_B - L^0_A)^2 \mathbf{G}_{ij} \tag{6.10}$$

which is similar to the relationship for long wavelength phonons in a single component lattice at a temperature T, if we were to replace $Kx(1-x)(L^0_A - L^0_B)^2$ by $k_B T$. Using (6.10) we have,

$$\frac{1}{2}\langle(\mathbf{Q}\cdot\mathbf{u}_{ij})^2\rangle = -\frac{K}{2}x(1-x)(L^0_A - L^0_B)^2\left[\mathbf{Q}\cdot(\mathbf{G}_{ii} + \mathbf{G}_{jj} - 2\mathbf{G}_{ij})\cdot\mathbf{Q}\right] \tag{6.11}$$

The Green's function can be written in k-space using the Fourier transform,

$$\mathbf{G}_{ii} + \mathbf{G}_{jj} - 2\mathbf{G}_{ij} = \frac{2}{N}\sum_{k}\mathbf{G}(\mathbf{k})(1 - e^{i\mathbf{k}\cdot\mathbf{R}^{0}_{ij}}). \tag{6.12}$$

For small $\mathbf{k}$, we may write,

$$\mathbf{G}(\mathbf{k}) = \frac{A_L\hat{\mathbf{k}}\hat{\mathbf{k}} + A_T(\mathbf{I} - \hat{\mathbf{k}}\hat{\mathbf{k}})}{k^2} \tag{6.13}$$

where, for the triangular lattice,[16]

$$A_T = 3A_L = \frac{8}{3a^2K} \tag{6.14}$$

and a is the lattice constant. Evaluating the integrals, we have

$$\begin{aligned}\frac{1}{2}\langle(\mathbf{Q}\cdot\mathbf{u_{ij}})^2\rangle \quad &= Kx(1-x)[Q(L_B^0 - L_A^0)]^2 \frac{1}{N}\sum_k \frac{A_T + (A_L - A_T)(\hat{\mathbf{Q}}\cdot\hat{\mathbf{k}})^2}{k^2}(1 - e^{i\mathbf{k}\cdot\mathbf{R}^0_{\mathbf{ij}}}) \\ &= Kx(1-x)[Q(L_B^0 - L_A^0)]^2 \frac{\sqrt{3}a^2}{8\pi}(A_L + A_T)\ln R^0_{ij} + const. \qquad (6.15)\end{aligned}$$

where we have used the integral,

$$\int \frac{(1 - e^{i\mathbf{k}.\mathbf{R}^0_{\mathbf{ij}}})}{k^2} d^2\mathbf{k} = 2\pi \ln R^0_{ij} + const. \qquad (6.16)$$

which is valid for large R^0_{ij}. The logarithmic distance dependence in (16) comes from the integrand around the origin, where the approximation (13) is valid. This leads us to the result,

$$e^{-\frac{1}{2}\langle(\mathbf{Q}\cdot\mathbf{u_{ij}})^2\rangle} = \frac{B(\mathbf{Q})}{(R^0_{ij})^\eta} \qquad (6.17)$$

and hence

$$C_{\mathbf{Q}}(R) = \frac{B(\mathbf{Q})}{R^\eta} \qquad (6.18)$$

where to leading order we can ignore the difference between R^0_{ij} and R. The exponent η given by,

$$\begin{aligned}\eta \quad &= Kx(1-x)[Q(L_B^0 - L_A^0)]^2 \frac{\sqrt{3}a^2}{8\pi}(A_L + A_T) \\ &= \frac{4}{3\sqrt{3}\pi}x(1-x)[Q(L_B^0 - L_A^0)]^2 \qquad (6.19)\end{aligned}$$

The correlation function $C_{\mathbf{Q}}(R)$ has the same form as that derived by Nelson,[5] with Lamé constants $\lambda = \mu = \sqrt{3}K/4$ and the real temperature replaced by T_D from Eq. (6.1), plotted in Fig.6.3. The results are averaged over the six equivalent nearest neighbor bond directions. Both the longitudinal and transverse distortions contribute to η in (19) through A_L and A_T. A similar result to Eq. (6.19) for *site* rather than *bond* disorder leads to a result for T_D as given in Eq. (6.2). In the site case, the distortions around each site have radial symmetry, which means that only the long

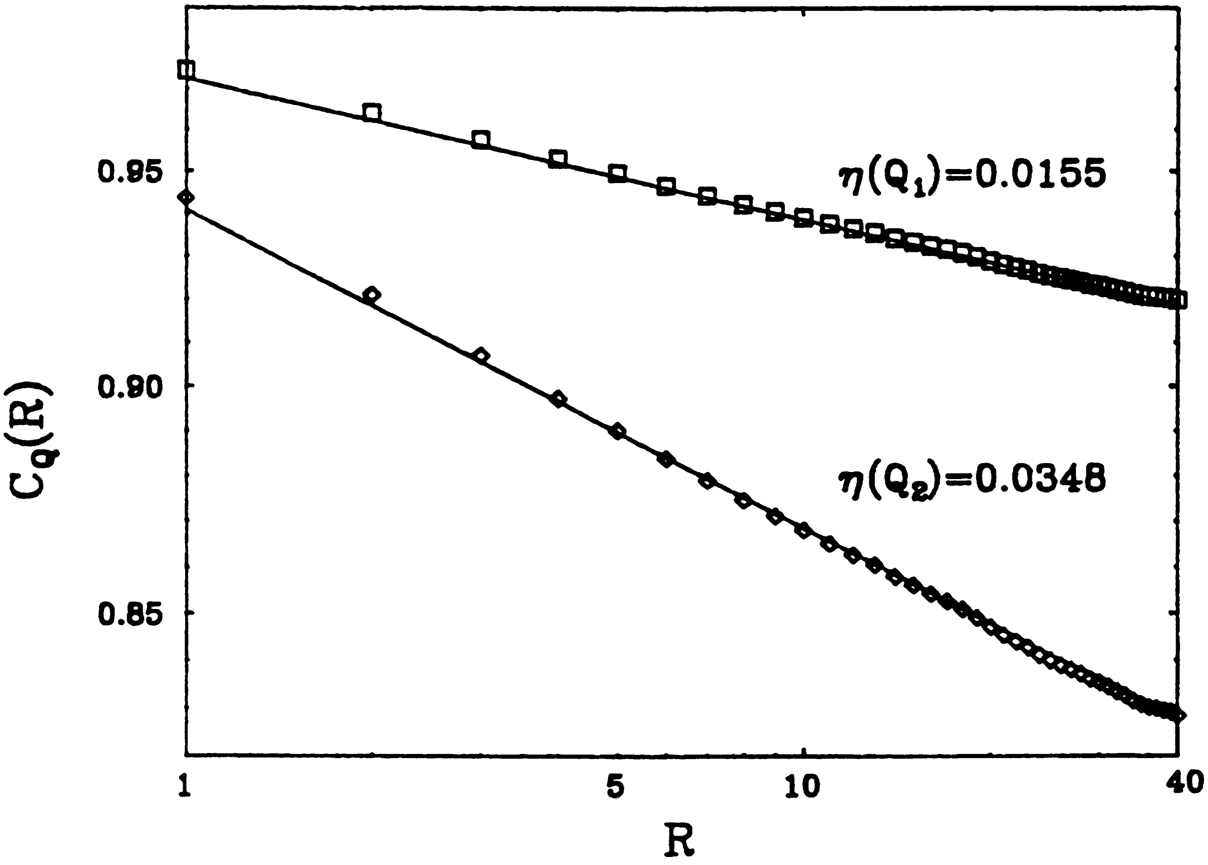

Figure 6.3: The density-density correlation function $C_{\mathbf{Q}}(R)$ plotted against the distance R in units where the mean bond length is unity. The results are averaged over the six equivalent nearest neighbor bond directions. The length mismatch parameter $(L_B^0 - L_A^0)/\langle L\rangle$ is 4% and the results are averaged over 4 samples, each of which is 100×100. The solid line is using the theory in Eqs. (18) and (19). The upper line is for $Q_1 a = 3\pi$ and the lower curve for $Q_2 a = 4\pi$; neither of which are reciprocal lattice points.

wavelength *longitudinal* distortions contribute to η through A_L.[8] The algebraic decay of the correlation function (6.18) is checked against computer simulations as shown in Fig.6.3, where the amplitude $B(\mathbf{Q})$ is treated as an adjustable constant. We can see that the theoretical approximation (6.18) is adequate.

The disordering of the perfect lattice is controlled by the parameter η which is determined by the size-mismatch rather than the temperature.[5] From the result (6.18), we are able to calculate the asymptotic form of the $I(\mathbf{q})$ around the reciprocal lattice vector at **g**=**Q**-**q**, where **q** is measured from the *nearest* reciprocal lattice vector **g**. Divergent behaviour is found for peaks with $\eta < 2$. However, contrary to previous claims[5] there is *no* cusp when $\eta > 2$. Combining Eqs. (6.8), (6.9) and (6.18), we have,

$$\begin{aligned} I(q) &= \int_a^\infty \int_0^{2\pi} e^{iqR\cos\theta}(\frac{a}{R})^\eta R dR d\theta \\ &= \int_a^\infty J_0(qR)(\frac{a}{R})^\eta R dR \\ &= a^\eta q^{\eta-2}\int_{qa}^\infty J_0(x)x^{1-\eta}dx \qquad (6.20) \end{aligned}$$

When $\eta < 2$, the kernel of the integral is well behaved at the low cut-off which can be replaced by zero. The integral (6.20) contributes a multiplier and $I(\mathbf{q})$ is divergent at small q as $q^{-(2-\eta)}$ where q is measured from the reciprocal lattice vector. When $\eta > 2$, we can not replace the low cut-off in (6.20) by zero. Using the fact that $J_0(x) \simeq 1$ for small x, we see that the lower cut-off gives a constant contribution $a^2/(2-\eta)$, and so we obtain an analytic result for $I(\mathbf{q})$. This suggests no **Q**-dependence in $I(\mathbf{Q})$ and hence no cusp when $\eta > 2$, which is verified by our simulation results shown in Fig.6.4.

The *pleating* transition occurs at a length mismatch of about 50%, so that the pleating is very apparent at a length mismatch of 60% as shown in Fig.6.5. Just before a 50% length mismatch, a few sites begin to pleat and the number increases rapidly as the size-mismatch exceeds 50% as shown in Fig.6.6.

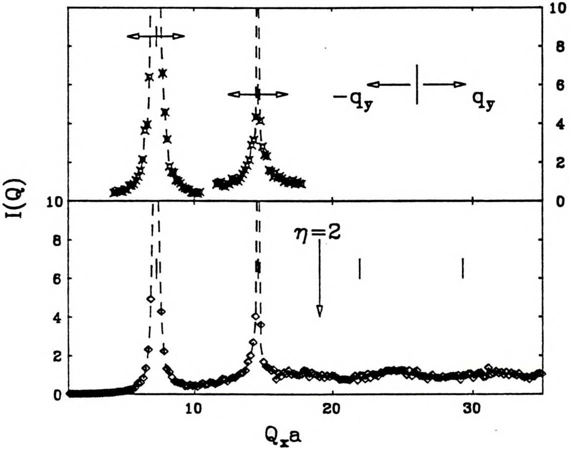

Figure 6.4: The lower panel shows the diffracted intensity $I(\mathbf{Q})$ plotted against the momentum variable Q_x, where the x direction contains a nearest neighbor bond, and the results are averaged over the six equivalent directions. The length mismatch parameter $(L_B^0 - L_A^0)/\langle L\rangle$ is 4% and an average is taken over 87 samples of 40 × 40 triangular lattices. The upper panel shows the diffracted intensity around the reciprocal lattice points in the lower panel but in the perpendicular direction.

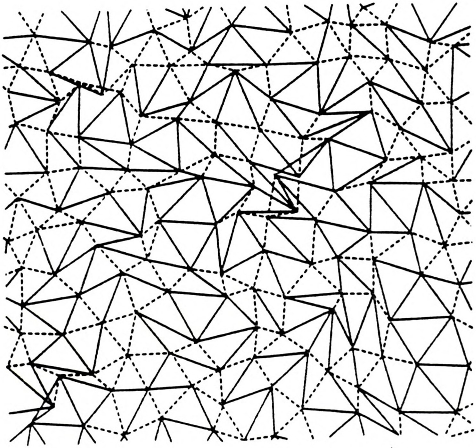

Figure 6.5: The relaxed triangular lattice after *pleating* has occurred. The length mismatch parameter $(L_B^0 - L_A^0)/\langle L \rangle$ is about 60%.

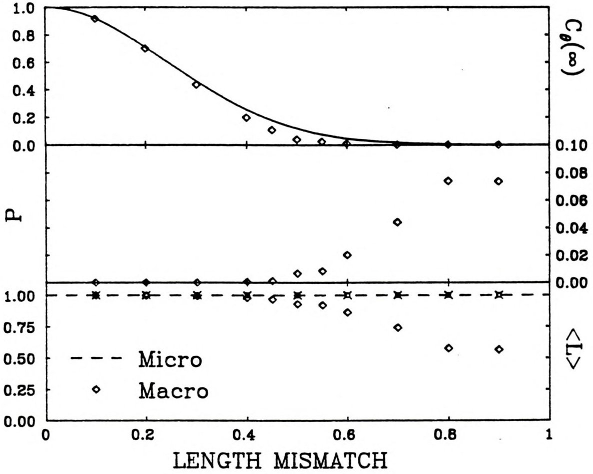

Figure 6.6: Showing the long range angular correlation $C_\theta(\infty)$, the pleating P, and the microscopic and macroscopic lengths $\langle L \rangle$ plotted against the length mismatch parameter $(L_B^0 - L_A^0)/\langle L \rangle$. The symbols are from the computer simulations and the dashed and solid lines are the theoretical results from Eq.(6.31) and ref.(6.5).

A pleated site is defined to have all six bonds to its nearest neighbors lying to one side within the 180° arc of a semicircle. The network chooses this form of disordering for large size-mismatches because it is prevented from forming dislocations and disclinations as occurs in the thermal case.[5] In the thermal case, the solid begins to melt as first dislocations and then disclinations begin to unbind, destroying the topological order. However, the topology is preserved in our model even when pleating occurs because the six nearest neighbors of a site remain fixed.

6.4 ANGULAR CORRELATION

Long range angular correlations are present and can be calculated within our model. The angular correlation function is defined as,

$$C_\theta(R) \equiv |\langle e^{i6\theta_{ij}}\rangle| \tag{6.21}$$

where $\theta_{ij} = \theta_i - \theta_j$ is the angle between two bonds emanating from lattice points i and j, and R is their separation. It is convenient to measure the θ_i from the underlying reference lattice, but it could also be measured from the line joining the sites i and j; the result would be the same to leading order. Because long range angular correlations exist, for large R,

$$\langle e^{i6\theta_{ij}}\rangle \longrightarrow \langle e^{i6\theta_i}\rangle\langle e^{-i6\theta_j}\rangle \tag{6.22}$$

and,

$$e^{-W_6} \equiv |\langle e^{-i6\theta_i}\rangle| \simeq e^{-\frac{1}{2}\langle(6\theta_i)^2\rangle} \tag{6.23}$$

and only the deviation $\delta\theta = \theta_i - n\pi/3$, where n is integer, is needed

$$\delta\theta = \frac{(\mathbf{u_{12}} \times \mathbf{R^0_{12}})}{\langle \mathbf{L} \rangle} \tag{6.24}$$

and $\langle L\rangle$ is the mean bond length. This gives us,

$$W_6 \quad = \frac{18\langle \mathbf{u^2_{12}} - (\mathbf{u_{12}} \cdot \mathbf{R^0_{12}})^2\rangle}{\langle L\rangle^2}$$

$$= -36Kx(1-x)\left[\frac{(L_A^0 - L_B^0)}{\langle L\rangle}\right]^2 Tr\left[(\mathbf{1} - \mathbf{R_{12}^0 R_{12}^0})(\mathbf{G_{11}} - \mathbf{G_{12}})\right]. \quad (6.25)$$

where we have used Eq. (6.10). We know that $\mathbf{R_{12}^0} \cdot (\mathbf{G_{11}} - \mathbf{G_{12}}) \cdot \mathbf{R_{12}^0} = -d/z$, where d is the dimension and z the coordination number.[17] For the triangular lattice, $d/z = 1/3$, so that,

$$W_6 = -36Kx(1-x)\left[\frac{(L_A^0 - L_B^0)}{\langle L\rangle}\right]^2 \left[Tr(\mathbf{G_{11}} - \mathbf{G_{12}}) - \frac{1}{3}\right] \quad (6.26)$$

where

$$\begin{aligned} Tr(\mathbf{G_{11}} - \mathbf{G_{12}}) &= \frac{1}{N}\sum_{\mathbf{k}} Tr\mathbf{G}(\mathbf{k})(1 - e^{i\mathbf{k}\cdot\mathbf{R_{12}^0}}) \\ &= \frac{1}{N}\sum_{\mathbf{k}} Tr\mathbf{G}(\mathbf{k})(1 - \gamma_{\mathbf{k}}) \\ &= -\frac{1}{N}\sum_{\mathbf{k}} \left[\frac{1}{\omega_1^2(\mathbf{k})} + \frac{1}{\omega_2^2(\mathbf{k})}\right](1 - \gamma_{\mathbf{k}}) \end{aligned} \quad (6.27)$$

and $\omega^2 = D_1 \pm \sqrt{D_2}$. The expressions needed are,

$$\gamma(\mathbf{k}) = \frac{1}{3}(\cos 2x + 2\cos x \cos y) \quad (6.28)$$

$$D_1 = 3 - 2\cos 2x - 2\cos x \cos y \quad (6.29)$$

$$D_2 = (\cos x \cos y - \cos 2x)^2 + 3\sin^2 x \sin^2 y \quad (6.30)$$

where $x \equiv k_x a/2$ and $y \equiv \sqrt{3}k_y a/2$. The $\mathbf{k}$-integration in (6.27) is done numerically to give,

$$W_6 = 17.2x(1-x)\left[\frac{(L_A^0 - L_B^0)}{\langle L\rangle}\right]^2 \quad (6.31)$$

and for large R gives,

$$C_\theta(\infty) = e^{-2W_6}. \quad (6.32)$$

The result (6.32) shows that the long range angular order always exists in our linearized calculation. When pleating occurs, the long range angular correlation is

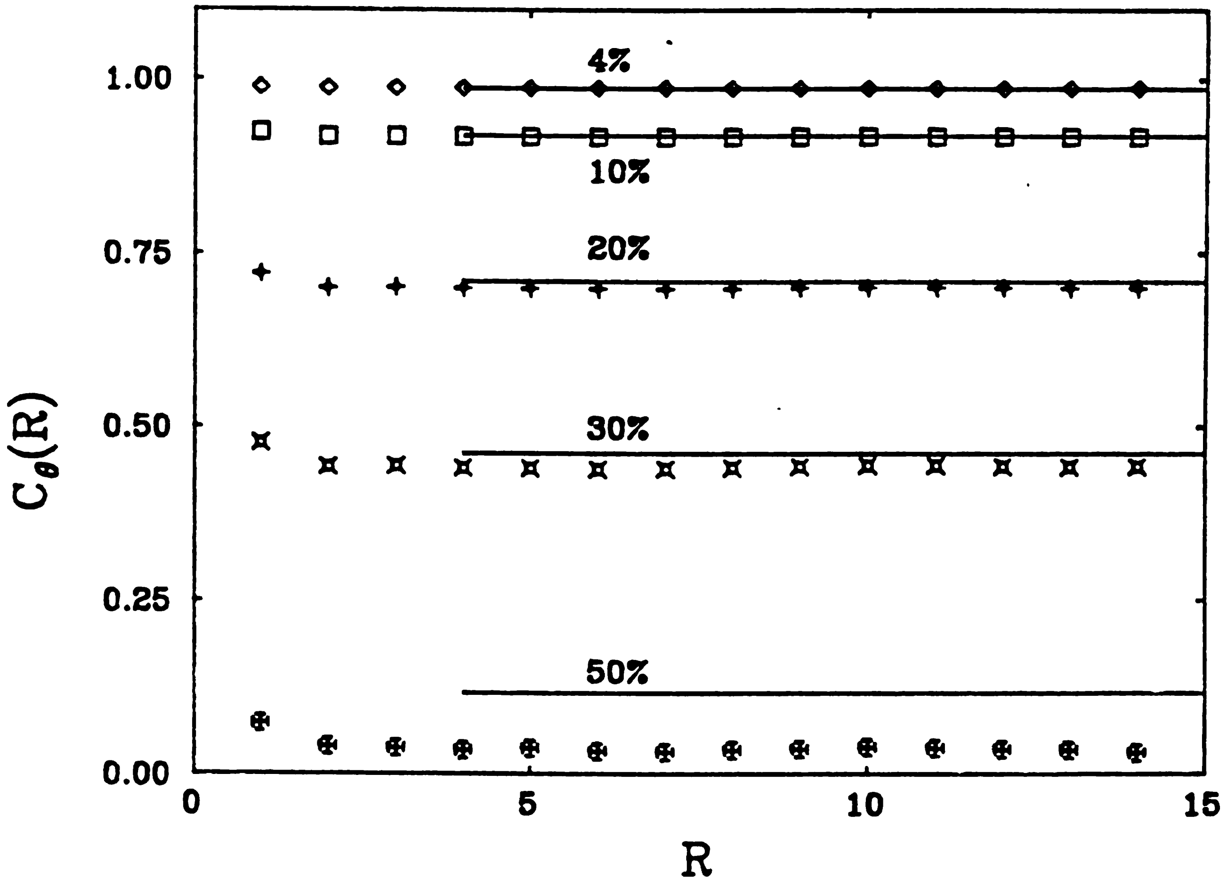

Figure 6.7: The angular correlation function $C_\theta(R)$ plotted against R in units where the mean bond length is unity. The results are averaged over the six equivalent directions defined by the nearest neighbor bonds. The results were obtained by averaging over 9 samples each of which was 40×40. The solid line is the asymptotic theory and the various values of the the length mismatch parameter $(L_B^0 - L_A^0)/\langle L \rangle$ are indicated.

destroyed as shown in Fig.6.6. We have performed simulations for different length mismatches and the results are shown in Figs.6.6 and 6.7. When there is no pleating, our analytic results agree well with the computer simulations. When pleating occurs, the computer result begins to drop below the prediction. The top panel in Fig.6.6, shows a comparison between the calculated long range angular correlation $C_\theta(\infty) = exp(-2W_6)$ and the simulation results. The agreement is very good up to about a 30% length mismatch, when effects due to pleating first start to have an effect. The theory predicts that the long range angular correlations are always present as no account is taken of pleating. In the second panel of Fig.6.6, we show the fraction of sites P that are pleated. This gives the clearest signature of the phase transition, although there is rounding as a result of finite size effects. The fraction of pleated sites may be thought of as a *disordering* parameter. In the bottom panel of Fig.6.6, we show the microscopic length and the macroscopic length from simulations. The microscopic length, defined as the average bond length, is constant as predicted by the theory (6.5), while the macroscopic length, deduced from the sample size, decreases above the pleating transition as would be expected. In pleating, the network folds over on itself, in the same manner as a pleat put in a piece of material, and hence reduces the area.

6.5 FINITE SIZE SCALING

Because of finite size effects, the Bragg peaks are never completely eliminated in our simulations. This is because of the artificial long range order imposed by the periodic boundary conditions. Nevertheless it is convenient to keep these boundary conditions as then every atom has exactly six nearest neighbors. We need to estimate the magnitude of this effect and try to extract the infinite size behaviour from the finite size simulations. This is easy for some quantities, like $C_\theta(R)$, and very difficult for others, like $I(\mathbf{Q})$. The scattering at the *Bragg* momentum $\mathbf{g}$ is, from Eqs. (6.8)

and (6.17),

$$\begin{aligned} I(\mathbf{g}) &= \frac{1}{N}\sum_{ij}\frac{B(\mathbf{g})}{(R^0_{ij})^\eta} \\ &\propto \int_a^L \frac{d^2\mathbf{R}}{R^\eta} \end{aligned} \tag{6.33}$$

For $\eta > 2$ and $L >> a$, this leads to,

$$I(\mathbf{g}) \propto L^{2-\eta} \tag{6.34}$$

and because $L^2 \propto N$, we may write,

$$\frac{I(\mathbf{g})}{N} \propto L^{-\eta} \tag{6.35}$$

This remnant Bragg peak contains an extra factor N because it is a Kronecker delta rather than a Dirac delta function.[12] Otherwise the Bragg peaks vanish as the system gets larger according to Eq. (6.35). This finite size scaling law can be verified by computer simulation and we have roughly verified that it does work using rather small samples with $L \leq 200$. The Bragg peak of the perfect lattice ($\eta = 0$) has a height proportional to N. As disordering is introduced by increasing T_D, and hence η, this weight is redistributed locally. In three dimensions, it becomes the Huang scattering,[12] while in two dimensions it either becomes a power law peak if $\eta < 2$ or background if $\eta > 2$ as shown in Fig.6.4. For large Q, the scattering tends to unity as the phases in Eq. (6.8) become random. Note that there is always a Bragg peak at the origin with weight N that represents a Dirac delta function with weight unity. When $L^{-\eta} << 1$, the scattering profile approaches that of the infinite sample. In Fig.4.4 the Bragg residue contains 30% of the weight of the first peak, while the second peak has only a 0.75% Bragg residue and is therefore representative of an infinite sample.

6.6 CONCLUSION

We have shown that the long-ranged properties of a two dimensional mixed crystal can be described by a linearized small displacement theory, as long as the topology

is kept fixed and no disclinations and/or dislocations are allowed. This is achieved naturally in a spring model with a fixed triangular network topology. While there is always long range orientational order present, the positional correlation function falls off algebraically, leading to power law peaks in the diffraction pattern.

This situation is similar to the thermal disordering of two dimensional lattices, and indeed many of our results can be understood if the temperature T in the thermal case is replaced by the disorder temperature T_D as defined by the strain energy in Eq. (6.1) or (6.2). This model can be regarded as the analogue of the quadratic θ^2 model of Zittartz[6] and José et al.[7] for spin wave excitations in the classical XY model in two dimensions. Like our model, the θ^2 model does not appear to contain any disclinations or dislocation type excitations, while successfully accounting for the instability against long range positional disorder and for the initial thermal disordering of the lattice. Our model can be regarded in a similar way. A more complete treatment would require abandoning the constraint of having six defined nearest neighbors, and using pair potentials for the AA, BB and AB interactions between the two kinds of atoms A and B in the random alloy $A_{1-x}B_x$. The repulsive part of the pair potential will completely inhibit the pleating, but the possibility of switching nearest neighbors leads to the flexibility of lowering the energy by creating disclinations, dislocations etc. Taking the thermal analogy seriously, such excitations would be expected to be present in the ground state as T_D is increased.

Thermal effects can be incorporated into our model at low temperatures. If the thermal and static displacements are controlled by the same force constant K, then the thermal and configuration averages can be done separately to give,

$$\eta = \frac{4q^2 k_B(T + T_D)}{3\sqrt{3}\pi K} \tag{6.36}$$

In the limit that T_D goes to zero, the usual thermal result is recovered.

Bibliography

[1] J. M. Kosterlitz and D. J. Thouless, J. Phys. C: Solid State Phys. **6**, 1181 (1973)

[2] D. R. Nelson, Phys. Rev. B**18**, 2318 (1978); B**27**, 2902 (1983)

[3] D. R. Nelson and B. I. Halperin, Phys. Rev. B**19**, 2457 (1979)

[4] K. Standburg, Rev. Mod. Phys., **60**, 1 (1988)

[5] D. R. Nelson, in **Phase Transitions and Critical Phenomena**, Ed. by C. Domb and J. L. Lebowitz, **7**, 1 (1983)

[6] J. Zittartz, Z. Physik B**31**, 89 (1978)

[7] J. José, L. P. Kadanoff, S. Kirkpatrick and D. R. Nelson, Phys. Rev. B**16**, 1217 (1977)

[8] J. Chen and M. F. Thorpe, unpublished

[9] M. F. Thorpe and E. J. Garboczi, Phys. Rev. B**42**, 8405 (1990)

[10] M. Paczuski, M. Kardar and D. R. Nelson, Phys. Rev. Letts., **60**, 2638 (1988) and references contained therein.

[11] W. Hume-Rothery, **The Structure of Metals and Alloys**, Institute of Metals, London, 1936

[12] M. F. Thorpe, J. S. Chung and Y. Cai, to be published in Phys. Rev. B.

[13] L. Vegard, Z. Phys. **5**, 17 (1921)

[14] K. Huang, Proc. Roy. Soc. A**190**, 102 (1947)

[15] Y. Cai, J. S. Chung, M. F. Thorpe and S. D. Mahanti, Phys. Rev. B**42**, 8827 (1990)

[16] E. J. Garboczi and M. F. Thorpe, Phys. Rev. B**32**, 4513 (1985)

[17] S. Feng, M. F. Thorpe and E. Garboczi, Phys. Rev. B**31**, 276 (1985)

Chapter 7

OVERVIEW AND PERSPECTIVE

This chapter is to be submitted to Physical Review B. This preliminary version is written by the author and the paper will be published under the names of Y. Cai and M. F. Thorpe.

7.1 LENGTH MISMATCH PROBLEM

We summarize the length mismatch problem[1] in this section and discuss the problem from a mathematical point of view in the next section.

7.1.1 Quaternary Solution and Sublattice Decoupling

Given small displacement, it is possible to expand it in a quadratic form,

$$E = \frac{1}{2}\mathrm{U}^{+}\mathrm{M}\mathrm{U} + \mathrm{U}^{+}\phi + E_0 \tag{7.1}$$

U is the displacement field vector and **M** the connectivity matrix. For a pure crystal, ϕ is usually the external force. For an alloy system, ϕ originates from different

types kind of disorder, such as disorder in the interaction strengths and lattice constants(natural lengths). It is then interpreted as internal strain. When the mismatch between natural lengths is small, the harmonic expansion is always valid.

The displacement field when relaxed minimizes the distortion energy, so we have the field equation:

$$\mathbf{MU} = \phi \tag{7.2}$$

The pure "Length Mismatch Problem" involves only disorder in the natural lengths so that the matrix **M** is free of disorder and only ϕ contains randomness. Technically this field equation can be solved by inverting **M** to obtain the Green's Function **G** and then evaluating **G** in momentum space,

$$\mathbf{U} = \mathbf{G}\phi \tag{7.3}$$

We will demonstrate this by solving the pure "Length Mismatch Problem" for a quaternary system $A_{1-x}B_xC_{1-y}D_y$ using the Kirkwood model where the disorder vector ϕ is linearly proportional to the length mismatch. The assumption needed for obtaining an analytic solution is that the natural lengths of the chemical bonds are additive.

The quaternary compounds $A_{1-x}B_xC_{1-y}D_y$ are interesting in the semiconductor industry because of the two tunable parameters that can satisfy the requirement of matching the substrate lattice constant and designing the band gap of coating material. One example is $In_{1-x}Ga_xP_{1-y}As_y$. The compound takes diamond structure. There are two FCC sublattices in the diamond lattice. Ga and In occupy one FCC while P and As take the other. Therefore in terms of A, B, C and D, there is no nearest neighbor connection between A, B and between C, D, and they take appropriate concentrations x and y in these different sublattices. This system is very general in the sense that we can reduce other alloy system into this form. For example, $Si_{1-x}Ge_x$ can be written as a quaternary as $Si_{1-x}Si_xGe_{1-x}Ge_x$. And ternary system such as $In_{1-x}Ga_xAs$ can be represented by $As_{1-y}As_yIn_{1-x}Ga_x$ and so on. The idea

is applicable to two dimensional system also, e.g., by decoupling a triangular lattice into three equivalent sublattices.

The sublattice decoupling actually transforms a system of less components to a system of more components. The trade-off to the increase of components is the decoupling of randomness between nearest neighbors so that the statistics can be performed independently in two sublattices. It is very useful when short range properties like the distribution of nearest neighbor distance is concerned. It may not be applicable to the problem of long range properties such as diffraction patterns because we need to decouple the system to such a degree that within the "concerned range" no lattice points belong to the same sublattice. The importance of decoupling of randomness will be seen in the following derivations.

We can calculate the distribution function of the nearest neighbor distance, from which the specific average lengths(first moment) and fluctuation(second moment) can be derived. We will proceed to give the full derivation of the distribution function.

We first make rules for the notation. Length with superscript "0" denotes natural length. Roman letter $i, j, ...$ denote one of the sublattices and Greek letter $\alpha, \beta, ...$ denote the other.

Denote the atomic radii of atom A, B, C and D as r_A, r_B, r_C and r_D. The additive of atomic radii means,

$$\begin{aligned} h^0_{AC} &= r_A + r_C \\ h^0_{AD} &= r_A + r_D \\ h^0_{BC} &= r_B + r_C \\ h^0_{BD} &= r_B + r_D \end{aligned} \tag{7.4}$$

Vegard's law is valid in the pure length disorder case. It means that the NN-

distance of the underline virtual crystal, or the mean NN-distance of the disorder system, is,

$$\begin{aligned} h_e &= (1-x)(1-y)h^0_{AC} + (1-x)yh^0_{AD} + x(1-y)h^0_{BC} + xyh^0_{BD} \\ &= (1-x)r_A + xr_B + (1-y)r_C + yr_D \end{aligned} \tag{7.5}$$

Now we introduce the projection operator on the site i as σ_i, and the same for the other sublattice by replacing i by α. σ is an $1d$ variable, i.e., when $\sigma = +1$, the site is A(or C), and when $\sigma = -1$, the site is B(or D). Given the concentration in two sublattices, $\langle \sigma_i \rangle = 1 - 2x$ or $\langle \sigma_\alpha = 1 - 2y$. The ensemble average is independent of i or α.

The natural length of any bond $i\alpha$ can be expressed in terms of the projection operators and the atomic radii,

$$\begin{aligned} h^0_{i\alpha} &= \frac{1+\sigma_i}{2}\cdot\frac{1+\sigma_\alpha}{2}h^0_{AC} + \frac{1+\sigma_i}{2}\cdot\frac{1-\sigma_\alpha}{2}h^0_{AD} \\ &\quad + \frac{1-\sigma_i}{2}\cdot\frac{1+\sigma_\alpha}{2}h^0_{BC} + \frac{1-\sigma_i}{2}\cdot\frac{1-\sigma_\alpha}{2}h^0_{BD} \\ &= \frac{1+\sigma_i}{2}r_A + \frac{1-\sigma_i}{2}r_B + \frac{1+\sigma_\alpha}{2}r_C + \frac{1-\sigma_\alpha}{2}r_D \\ &= h_m + \Delta_{AB}\sigma_i + \Delta_{CD}\sigma_\alpha \end{aligned} \tag{7.6}$$

where $h_m = (r_A + r_B + r_C + r_D)/2$ and $\Delta_{AB} = r_A - r_B$, $\Delta_{CD} = r_C - r_D$.

The length distribution function of certain kind of bond is defined as,

$$P_{\epsilon_1\epsilon_2}(h) \equiv \left\langle \frac{1+\epsilon_1\sigma_i}{2}\cdot\frac{1+\epsilon_2\sigma_\alpha}{2}\delta(h - h_{i\alpha})\right\rangle \tag{7.7}$$

the ϵ can be $+1$ for A(or C), and -1 for B(or D). So there are four combinations of $\epsilon_1\epsilon_2$ for AC,AD,BC and BD respectively.

Replacing the δ-function by a q integral, we have,

$$P_{\epsilon_1\epsilon_2}(h) = \left\langle \frac{1+\epsilon_1\sigma_i}{2}\cdot\frac{1+\epsilon_2\sigma_\alpha}{2}\frac{1}{2\pi}\int_{-\infty}^{+\infty} e^{iq(h-h_{i\alpha})}dq\right\rangle$$

$$= \frac{1}{2\pi}\int_{-\infty}^{+\infty} e^{iqh} F_{\epsilon_1\epsilon_2}(q)dq, \tag{7.8}$$

where

$$F_{\epsilon_1\epsilon_2}(q) = \left\langle \frac{1+\epsilon_1\sigma_i}{2} \cdot \frac{1+\epsilon_2\sigma_\alpha}{2} e^{-iqh_{i\alpha}} \right\rangle \tag{7.9}$$

Now we need the expression for $h_{i\alpha}$ which is supposed to be solved from Eq.(7.3). We will utilize the Kirkwood model as an example to solve the length mismatch problem here.

Kirkwood model with only natural length disorder takes the form,

$$E = \frac{\alpha}{2}\sum_{\langle ij\rangle}(h_{ij} - h_{ij}^0)^2 + \frac{\beta}{2}\langle h_c\rangle^2 \sum_{\langle ijk\rangle}(\cos\theta_{ijk} + \frac{1}{3})^2 \tag{7.10}$$

In this equation i, j, k can be in either sublattices. The force constant β has the same unit as α in the above expression. The expansion form of Kirkwood model fits the field equation of length mismatch problem in the following first order approximation, namely,

$$h_{i\alpha} = h_e + \hat{\mathbf{r}}_{i\alpha} \cdot \mathbf{u}_{i\alpha} \tag{7.11}$$

This linear approximation is checked to be good by computer simulation for small mismatch. The second order terms of expansion contributes to the disorder in force constants, which is not important in the length distribution when the disorder is not large. The **M** matrix is free of disorder, thus is the same as for the crystalline structure. Disorder only appears in the ϕ vector. It can be written as,

$$\phi = -\alpha\sum_{\langle i\alpha\rangle}(h_e - h_{i\alpha}^0)|i\alpha > \tag{7.12}$$

where $|i\alpha > \equiv |i> - |\alpha>$.

So the $h_{i\alpha}$ is,

$$\begin{aligned} h_{i\alpha} &= h_e + \hat{\mathbf{r}}_{i\alpha} \cdot \mathbf{u}_{i\alpha} \\ &= h_e - \alpha\sum_{j\beta}\mathbf{G}_{i\vec{\alpha},j,\vec{\beta}}(h_e - h_{j\beta}) \end{aligned}$$

$$= \quad h_e + \alpha \sum_{j\beta} \mathbf{G}_{\vec{i\alpha},\vec{j,\beta}} h_{j\beta} \tag{7.13}$$

any element of the green's function in the shorthand notation above is defined as,

$$\mathbf{G}_{\vec{ij},\vec{kl}} \equiv \hat{\mathbf{r}}_{ij} \cdot (< i| - < j|)\mathbf{G}(|k> - |l>) \cdot \hat{\mathbf{r}}_{kl} \tag{7.14}$$

and

$$\sum_{\langle j\beta \rangle} \mathbf{G}_{\vec{i\alpha},\vec{j\beta}} = 0 \tag{7.15}$$

because an uniform displacement keeps the system invariant.

Substitute Eq.(7.6) into Eq.(7.13), and using the properties given by the sum-rule Eq.(7.15), we obtain,

$$\begin{aligned} h_{i\alpha} &= h_e + \frac{\alpha}{2} \sum_{\langle j\beta \rangle} \mathbf{G}_{\vec{i\alpha},\vec{j\beta}} (\Delta_{AB}\sigma_j + \Delta_{CD}\sigma_\beta) \\ &= h_e + \frac{\alpha}{2}\Delta_{AB} \sum_{\langle j\beta \rangle} \mathbf{G}_{\vec{i\alpha},\vec{j\beta}}\sigma_j + \frac{\alpha}{2}\Delta_{CD} \sum_{\langle j\beta \rangle} \mathbf{G}_{\vec{i\alpha},\vec{j\beta}}\sigma_\beta \end{aligned} \tag{7.16}$$

Note that we have decoupled the random variables σ_i and σ_α so that the ensemble average can be perform in the each sublattice separately. Denote

$$\begin{aligned} A_{ij} &= \frac{\alpha}{2}\Delta_{AB} \sum_{\beta(j)} \mathbf{G}_{\vec{i\alpha},\vec{j\beta}} \\ A_{\alpha\beta} &= \frac{\alpha}{2}\Delta_{CD} \sum_{j(\beta)} \mathbf{G}_{\vec{i\alpha},\vec{j\beta}} \end{aligned} \tag{7.17}$$

where $j(\beta)$ means β is the nearest neighbor of j.

We define the lattice integral a^{**} as

$$a^{**} \equiv \sum_{\beta(j)} \mathbf{G}_{i\alpha,j\beta}, \tag{7.18}$$

so,

$$\frac{A_{ii}}{\Delta_{AB}} = \frac{A_{\alpha\alpha}}{\Delta_{CD}} \equiv \frac{1}{2}a^{**} \tag{7.19}$$

a^{**} is one of the lattice integral we encounter most frequently.

With the above notations, and making use the fact that the random variables in two sublattices can be averaged independently, from Eq. (7.9) and Eq. (7.16) we have,

$$F_{\epsilon_1\epsilon_2}(q) = e^{-iqh_e} \left\langle \frac{1+\epsilon_1\sigma_i}{2} e^{-iq\sum_j A_{ij}} \right\rangle \left\langle \frac{1+\epsilon_1\sigma_\alpha}{2} e^{-iq\sum_\beta A_{\alpha\beta}} \right\rangle \tag{7.20}$$

We only have to evaluate one of the average in the above expression and the other is the same.

$$\begin{aligned} I_\epsilon(q) &\equiv \left\langle \frac{1+\epsilon\sigma_i}{2} e^{-iq\sum_j A_{ij}\sigma_i} \right\rangle \\ &= \left\langle \frac{1+\epsilon\sigma_i}{2} \prod_j (\cos qA_{ij} - i\sigma_j \sin qA_{ij}) \right\rangle, \end{aligned} \tag{7.21}$$

where we have made use of the identity $\sigma_i^2 = 1$. So,

$$\begin{aligned} I_\epsilon(q) &= \frac{1}{2} \Big\{ \langle \prod_j (\cos qA_{ij} - i\sigma_j \sin qA_{ij}) \rangle \\ &\quad + \epsilon \langle \prod_{j \neq i} (\cos qA_{ij} - i\sigma_j \sin qA_{ij}) \rangle \cdot \langle (\sigma_i \cos qA_{ii} - i \sin qA_{ii}) \rangle \Big\} \end{aligned} \tag{7.22}$$

Notice that the product is over distinct sites and so expanding, we will have to average quantities such as $\langle \sigma_l \sigma_m ... \sigma_n \rangle$, which is just $\langle \sigma_l \rangle \langle \sigma_m \rangle ... \langle \sigma_n \rangle$ in the random case. This means that we can factorize all such products. Using $\langle \sigma_j \rangle = 1 - 2x$, we have

$$\begin{aligned} I_\epsilon(q) &= \frac{1}{2} \left[\prod_{j \neq i} (\cos qA_{ij} - i(1-2x) \sin qA_{ij}) \right] \\ &\quad \cdot \Big\{ \cos qA_{ii} - i(1-2x) \sin qA_{ii} + \epsilon[(1-2x) \cos qA_{ii} - i \sin qA_{ii}] \Big\} \end{aligned} \tag{7.23}$$

Making use of the fact that $\epsilon^2 = 1$, we can rewrite $I_\epsilon(q)$ as

$$I_\epsilon(q) = \left[\frac{1+\epsilon(1-2x)}{2} \right] (\cos qA_{ii} - i\epsilon \sin qA_{ii}) \prod_{j \neq i} [\cos qA_{ij} - i(1-2x) \sin qA_{ij}]$$

$$= \left[\frac{1+\epsilon(1-2x)}{2}\right] e^{-i\epsilon q A_{ii}} \prod_{j\neq i}[\cos qA_{ij} - i(1-2x)\sin qA_{ij}] \,. \tag{7.24}$$

Substituting this result in the distribution function and regrouping them properly, we obtain the solution,

$$F_{\epsilon_1\epsilon_2}(q) \quad = \frac{1+\epsilon_1(1-2x)}{2} \cdot \frac{1+\epsilon_2(1-2x)}{2} f(q)$$

$$e^{\{-iq[h_e+(\epsilon_1-1+2x)\Delta_{AB}a^{**}/2+(\epsilon_2-1+2y)\Delta_{CD}a^{**}/2)]\}} . \tag{7.25}$$

The function $f(q)$ is independent of the species and has the form,

$$f(q) = \quad e^{-i(1-2x)qA_{ii}} \prod_{j(\neq i)} [\cos qA_{ij} - i(1-2x)\sin qA_{ij}]$$

$$\cdot e^{-i(1-2y)qA_{\alpha\alpha}} \prod_{\beta(\neq\alpha)} [\cos qA_{\alpha\beta} - i(1-2x)\sin qA_{\alpha\beta}], \tag{7.26}$$

Note that $f(q)$ is independent of ϵ_1 and ϵ_2 which specify the type of chemical bonds. From Eq.(7.25) for $F_{\epsilon_1\epsilon_2}(q)$ we conclude that the distribution functions for all four specific bonds are **exactly** the same for all given concentrations. The weights of four peaks are $(1-x)(1-y)$, $(1-x)y$, $x(1-y)$ and xy for AC,AD,BC and BD respectively. Computer simulation result checks with this as shown in Fig.7.1.

From the distribution function we derive the average of specific nearest neighbor distance as,

$$\langle h_{\epsilon_1\epsilon_2}\rangle = h_e + a^{**}[\Delta_{AB}(\epsilon_1 - 1 + 2x) + \Delta_{CD}(\epsilon_2 - 1 + 2y)]/2 \tag{7.27}$$

The width of the distribution are the same for all,

$$\langle h^2_{\epsilon_1\epsilon_2} - \langle h_{\epsilon_1\epsilon_2}\rangle^2\rangle = [x(1-x)\Delta^2_{AB} + y(1-y)\Delta^2_{CD}](a_1^{**} - a^{**2}) \tag{7.28}$$

where constant a_1^{**} is related to a^{**},

$$a_1^{**} = -\alpha^2 \frac{\partial(a^{**}/\alpha)}{\partial\alpha} \tag{7.29}$$

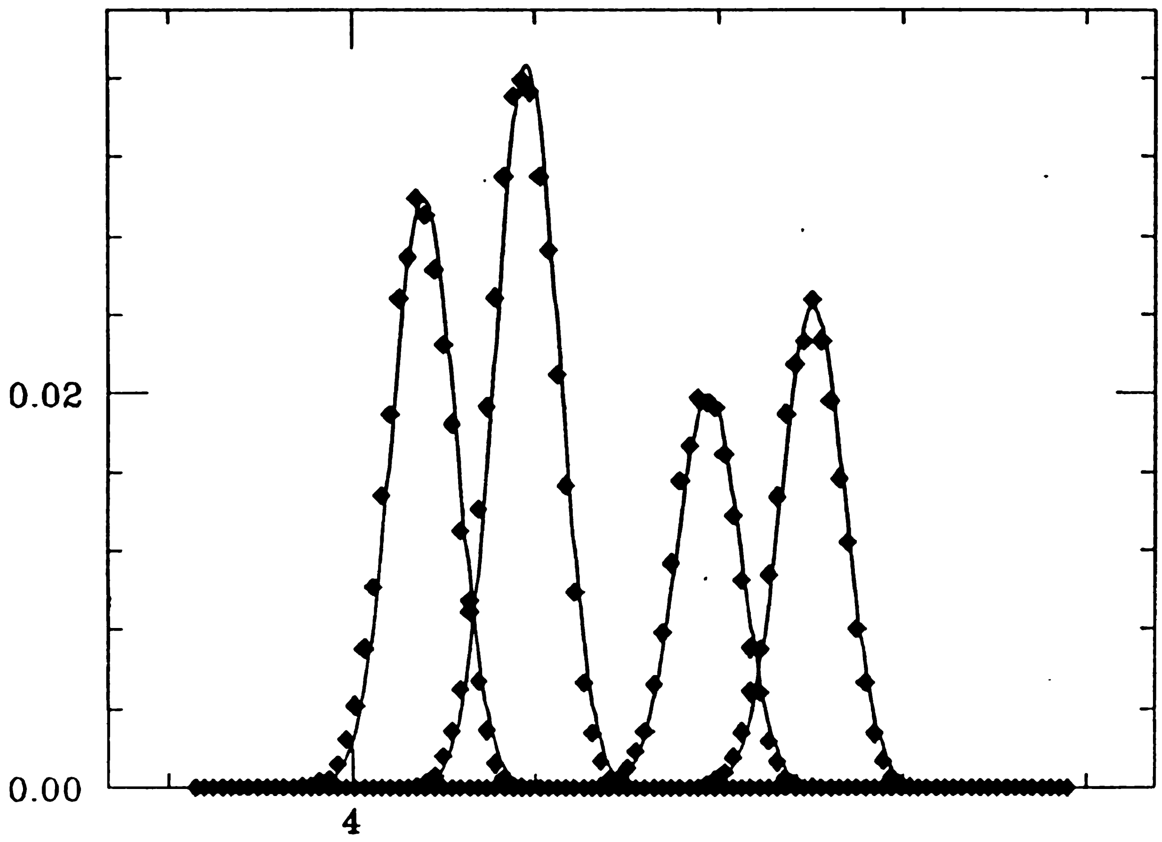

Figure 7.1: Four NN-length distribution of a Quaternary compounds, $A_{1-x}B_xC_{1-y}D_y$. $x = 0.6$ and $y = 0.45$. The four peaks are exactly the same in shape with proper weights 0.27 : 0.33 : 0.18 : 0.22. The symbols are from computer simulation using Kirkwood model with $\beta/\alpha = 0.2$ and the solid line is a gaussian fit use the centers and widths given in the text.

We can also evaluate the averaged next nearest neighbor distance using the projection method. We give below the full derivation.

R_{ij} is the NNN-distance and i, j belong to the same sublattice. Upto linear approximation(same as in Eq.(7.11)), we have,

$$
\begin{aligned}
R_{ij} &= r^e_{nnn} + \hat{\mathbf{r}}_{ij} \cdot \mathbf{u}_{ij} \\
&= r^e_{nnn} + \sqrt{\frac{3}{8}}(\hat{\mathbf{r}}_{i\alpha} - \hat{\mathbf{r}}_{j\alpha}) \cdot (\mathbf{u}_{i\alpha} - \mathbf{u}_{j\alpha}) \\
&= r^e_{nnn} + \sqrt{\frac{3}{8}}\,[(\hat{\mathbf{r}}_{i\alpha} \cdot \mathbf{u}_{i\alpha} + \hat{\mathbf{r}}_{j\alpha} \cdot \mathbf{u}_{j\alpha}) - (\hat{\mathbf{r}}_{i\alpha} \cdot \mathbf{u}_{j\alpha} + \hat{\mathbf{r}}_{j\alpha} \cdot \mathbf{u}_{i\alpha})] \qquad (7.30)
\end{aligned}
$$

$r^e_{nnn} = \sqrt{8/3}h_e$ is the mean next nearest neighbor distance.

The ensemble average of R_{ij} can be performed by using the projection operator $P^i_\epsilon = (1 + \epsilon\sigma_i)/2$,

$$
\langle R \rangle^{i\alpha j}_{\epsilon_1\epsilon_2\epsilon_3} = \frac{1}{\langle P^i_{\epsilon_1} \rangle \langle P^\alpha_{\epsilon_2} \rangle \langle P^j_{\epsilon_3} \rangle} \left\langle P^i_{\epsilon_1} P^\alpha_{\epsilon_2} P^j_{\epsilon_2} R_{ij} \right\rangle \qquad (7.31)
$$

$i\alpha j$ means site α in the middle with i and j connected to it as its nearest neighbors. There are 8 combinations from $\epsilon_1\epsilon_2\epsilon_3$ representing 8 different type NNN-connection. Switching two sublattice notation we have another 8 combinations which are symmetric with the above expression.

Bring Eq.(7.30) and Eq.(7.3) into above equation and perform the ensemble average. Remember that the formula Eq.(7.15) effectively eliminates the constant terms from the averaging. The statistics is straight forward. Regrouping the results properly, we end up with following expression,

$$
\begin{aligned}
\langle R \rangle^{i\alpha j}_{\epsilon_1\epsilon_2\epsilon_3} &= r^e_{nnn} + \sqrt{\frac{8}{3}}a^{**}\Delta_{CD}y(1-y)\frac{\epsilon_2}{\langle P^{\epsilon_2}_\alpha \rangle} \\
&\quad + \sqrt{\frac{3}{8}}b^{**}\Delta_{AB}x(1-x)[\frac{\epsilon_1}{\langle P^{\epsilon_1}_i \rangle} + \frac{\epsilon_3}{\langle P^{\epsilon_3}_j \rangle}]
\end{aligned}
$$

$$= r^e_{nnn} + \frac{1}{2}\sqrt{\frac{8}{3}}a^{**}\Delta_{CD}(\epsilon_2 + 2y - 1)$$

$$+\sqrt{\frac{3}{8}}b^{**}\Delta_{AB}(2x + 1 + \frac{\epsilon_1 + \epsilon_3}{2}), \tag{7.32}$$

where α, i, j denote sublattices as mentioned before. b^{**} is another constant similar to a^{**} and is evaluated from the Green's function,

$$b^{**} = \sqrt{\frac{8}{3}}\sum_{\beta} \mathrm{G}_{\vec{ij},\vec{i\beta}} \tag{7.33}$$

In the expression β and α(implicit) are first neighbors of i and β is summed over. j is the nearest neighbor of α thus the next nearest neighbor of i.

The simple model is extremely good in describing a large class of semiconductor material. For materials where difference in the force constants is appreciable, we resort to the effective medium theory, which appears to be good in describing these kinds of problems. But here we will be satisfied with the qualitative conclusions that can be drawn from the above simple expressions, obtained for the case when force constants are the same.

7.1.2 Topological Rigidity Constants

The constant a^{**}, for example, has been defined in term of Green's function in Eq. (7.18). It can be understood however from another angle. Suppose we have a pure diamond lattice described by the Keating model or the Kirkwood model with force constant α and β. Consider an atom and apply uniform radial forces f on its four neighbors. This opens a cage and the neighbors gain a displacement u. If there is no matrix effect, the displacement is just f/α. But the existence of the matrix makes it harder to open a cage. The force needed for the same displacement is,

$$f = \frac{\alpha}{a^{**}}u \tag{7.34}$$

Note that we use the same parameter a^{**} as above and it is straight forward to show it to be true. Here a^{**} acquires its physical meaning. It represents the rigidity of the matrix which depends on the force ratio β/α and the topology of the lattice construction. We call it the topological constant in opening a cage. A similar approach has been used by Thorpe and Garboczi to describe a triangular net of "bond" disorder, and a different topological rigidity constant a^* is used which corresponds to stretching of a bond by a pair of forces along that bond. We have another constant b^{**} introduced in the last section. Compared to a^{**}, which is related to the displacement of first neighbor when opening a cage, b^{**} is related to the displacement of next nearest neighbor when opening the same cage.

In general, there are infinite number of lattice integrals in a rigid network. Using a simple model we have shown how the local quantities are related to each other by a certain number of characteristic topological rigidity constants. Our approach to the semiconductor alloys has the advantage that it produces simple analytic formulae that make the underlying physics clear in terms of these topological rigidity parameters. The non-additivity of the atomic radii, and the variation of the force constants α and β, can be incorporated into our approach using perturbation theory. Non-random solid solutions can also be handled by defining concentration dependent topological rigidity parameters.

For semiconductor alloy material, a^{**} is around 0.75, while it is about 0.24 for FCC metal alloys. This reflects the large number of nearest neighbors(12 rather than 4). However effects like charge transfer, variation in the force constants, non-additivity of the atomic radii, and even the failure of rigid ion potentials or embeded atom potentials, make the situation much more complex. And a similar approach, involving nearest neighbor central forces is much less successful for some systems like $Au_{1-x}Ni_x$.[5]

7.2 MODEL AND MATHEMATICS

Analytic solutions are useful because it can serve as a starting point. That is why people like to construct models which are mathematically simple and physically realistic. While we define the "Length Mismatch Problem" in such a simple field Eq. (7.2), the structure of semiconductor materials are also studied by more sophisticated method like *ab initio*[2] calculations. Fig.7.2 compares the nearest neighbor distance of $SiGe$ alloy. In the plot there are result from the *ab initio* calculation and experiment, and the simple application of our quaternary result from Eq.(7.27) and Eq.(7.28). The only parameter that we fit is the topological rigidity constant a^{**} which is about 0.707 corresponding to a value of β/α about 0.2 in the Kirkwood model. As we stated before, a^{**} is one of the characteristic of the system. Once the parameter is known, we can express local properties, such as averaged NN-distance and NNN-distance. Fig.7.3 is the nearest neighbor information for $Ga_{1-x}In_xAs$. The characteristic constant, a^{**}, from this diagram, is about 0.8. And given this a^{**} we compare the Z-curve and distribution with computer simulation and experiment. The experiment data agrees very well with on theoretical predictions. And from our model, we know that b^{**} is about one half of a^{**}. From this we can compare the next nearest neighbor distance of the same system with experimental results. The theory is from Eq.(7.32). In Fig.7.4 we can see the agreement is very good. We should point it out that while both *ab initio* calculations and our theory give good agreement with the experiment, *ab initio* calculations show 4% upward bowing in contrast to the 7% downward bowing observed in experiment for the $Si_{1-x}Ge_x$ binary alloy.[6]

Most of our models are simple from mathematical point of view. Our goal has been to understand the physics of certain observation with minimum mathematical complexity. Let's take the model for intercalated graphite multilayer system as an example. The model is a harmonic lattice model of "bond" disorder. First, the introduction of natural lengths simplifies the interaction and makes it possible to write the energy in a compact quadratic form. The next step is the harmonic approximation.

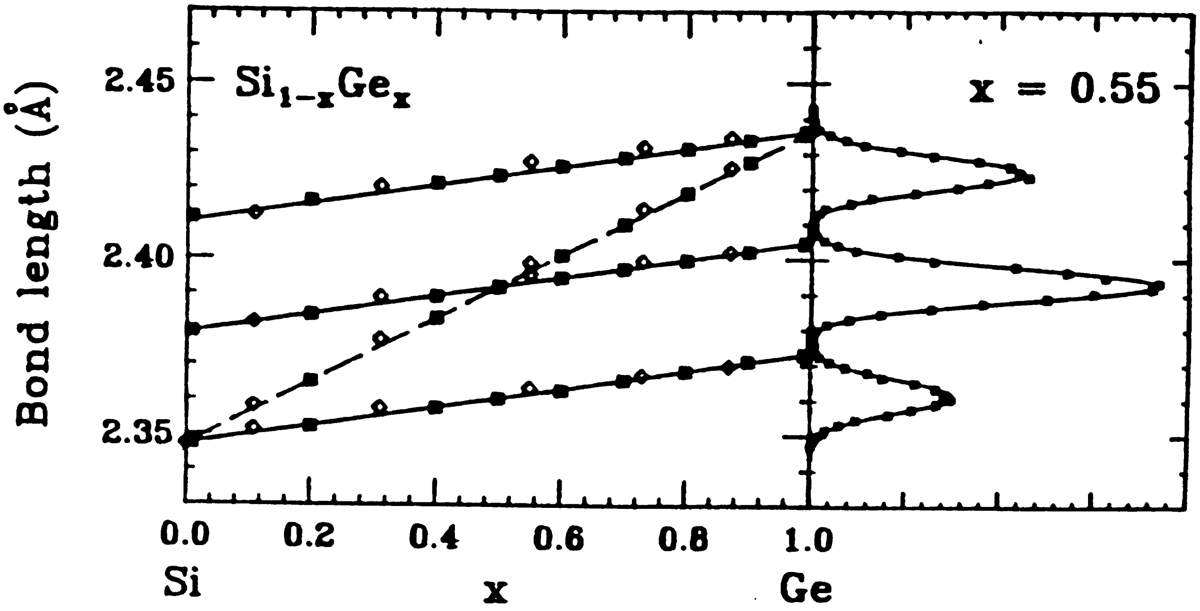

Figure 7.2: The left panel shows the results of our model using the Kirkwood potential with $\beta/\alpha = 0.2$ for $Si_{1-x}Ge_x$ alloys plotted as straight lines, the simulation results for the same model(solid symbols) and the pseudopotential results of ref. [2] (open symbol). The lengths for pure Si and Ge are chosen to agree with ref. [3]. The right panel shows our computer simulation results on a 13, 824 atom sample, with periodic boundary conditions, for the length probability distribution of nearest neighbor Si-Si, Ge-Ge and Si-Ge bonds for $x = 0.55$. The solid curves are Gaussians with centers, widths and weights determined from the equations in the text.

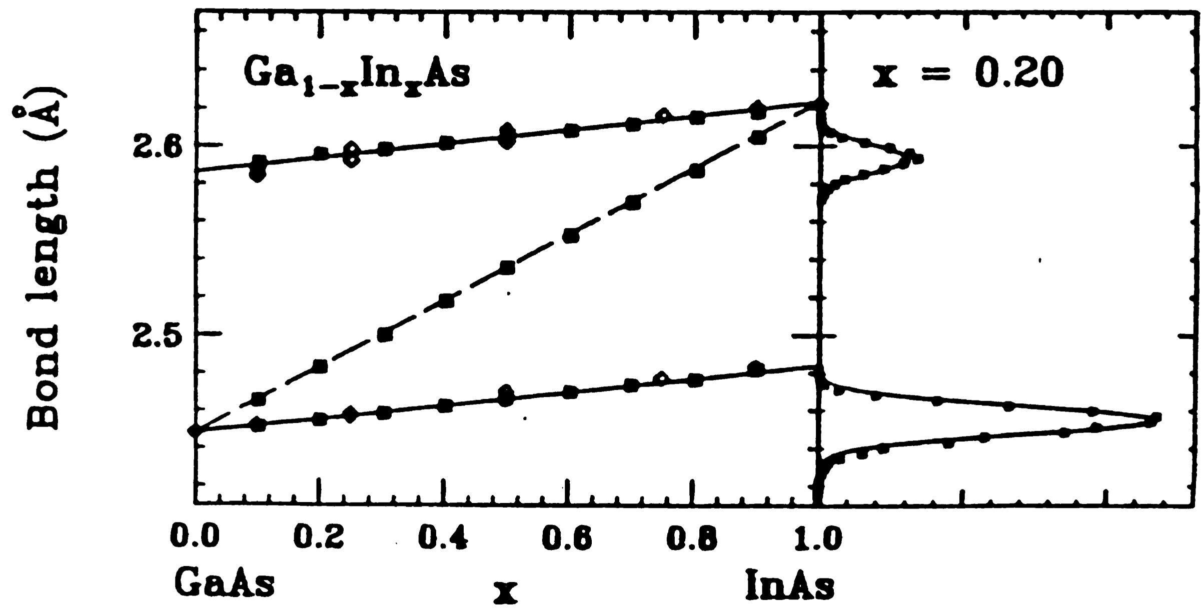

Figure 7.3: The left panel compares the experimental results of Mikkelson and Boyce[3](open symbols) for $Ga_{1-x}In_xAs$ with simulation results using the Kirkwood potential with $\beta/\alpha = 0.12$ (Solid symbols) and straight lines from the theory given in the Eq.(7.27). The right panel shows our computer simulation results on a 13,824 atom sample, with periodic boundary condition, for the length probability distribution of nearest neighbor *Ga-As*,*In-As* bonds for $x = 0.2$. The solid curves are Gaussians with centers, widths and weights determined from the equation in the text

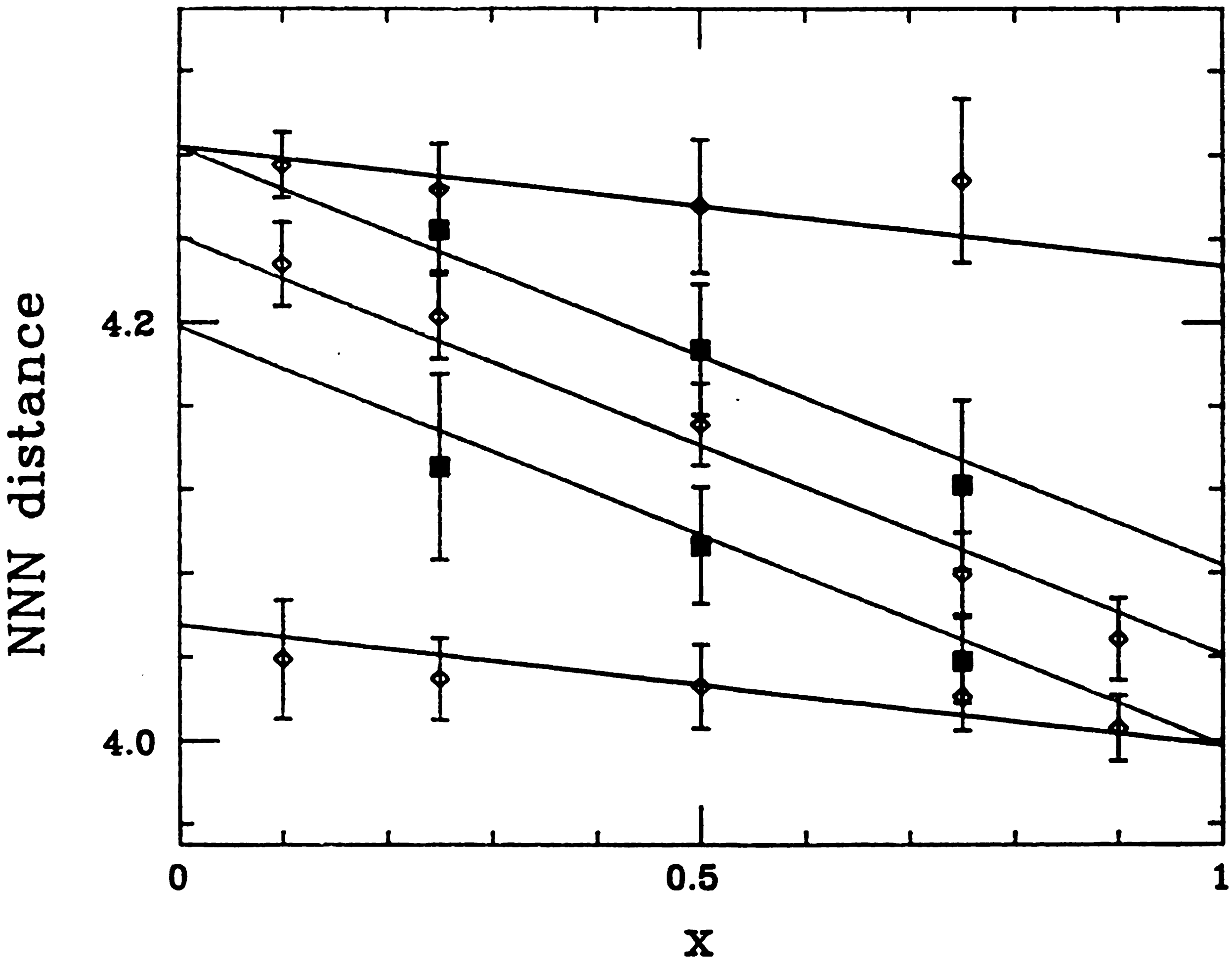

Figure 7.4: The next nearest neighbor distance from experiment(with error bars) and our theory prediction(solid lines). The a^{**} is about 0.8 corresponding to 0.12 of β/α in the Kirkwood model. b^{**} is about 0.4 for the same force constant.

This step can be skipped in this particular system because the field equation is ready to be written down as $\mathbf{MU} = \phi$. Generally, within the lattice model there is disorder in the force constant, mass and natural length. The first two are important to the phonon structure and related electronic properties. But they are less important in determining structural configurations comparing to size difference. The most important reason to stress only the size difference, from a mathematical point of view, is that **M** matrix would be the same as that for a crystalline structure. This makes it possible to invert the **M** matrix to the other side of the equation and give explicit solutions for the displacement field.We can utilize all the methods we know from Bloch theory. The disorder, with or without correlation, can be treated statistically. From this, we conclude that as long as disorder in force constant is negligible, we have a similar path to an analytic solution whether there is correlation or not in the intercalating process. The same idea applies to alloy systems when natural length concept is meaningful. In this case, more steps are however needed in the simplification because we need the lattice model of "site" disorder instead of "bond". Further harmonic approximation is necessary to reach the same field equation as for the "bond" case which we define as the pure "length mismatch problem". We have checked with computer simulation that all the approximation are good up to a moderate size mismatch. (see **Chapter 4**)

We see that "length mismatch problem" is simple from a mathematical point of view while it carries the feature of semiconducting materials when only structural information is concerned. It makes use of the old concept like virtual crystal, consequently the old method of Fourior Transformation or **K** space expansion resulting from the translational invariance.

One however has to bear in mind that analytic solution is not everything. Simplification many time lose subtle features of the original system in the process, especially in dynamic systems. So care has to be taken in any simplification. It is important to have physical insight. Our another model for covalent glasses(**Chapter 2**) serves as

a very good example. It is not soluble analytically, but we have seen it works very well. In the covalent glass systems chemical bonding is quite stable and serves as the major bonding force to solidify the system. This picture has lead to the introduction of rigidity percolation which states that when the number of constraints provided by these bonds drop below the requirement to fix all the degree of freedom of the lattice network, the system becomes floppy and there will be zero frequency modes present. This basic idea leads to the birth of the well known concept of threshold point $\langle r \rangle = 2.4$. [4] It is very important to have this insight that the soft phonon observed in experiment actually are another form of the zero frequency modes resulting from the underconstrainted degrees of freedom in the rigidity percolation problem. The transformation from zero frequency modes to low frequency modes is done by turning on the weak forces which are neglected when doing the percolation analysis. These weak forces are not important when rigidity percolation prevails. But they play important roles in stablizing the system when rigidity fails to percolate. So our model is built to generate the most important ingredient of the system, i.e., the mean coordination number $\langle r \rangle$. This very simple model performs very well and predictions of the model agrees with experiments.

7.3 TWO DIMENSIONAL INSTABILITY

In **Chapter 6** we studied the 2d triangular network. It is found that when the mismatch is very large, the lattice begins to pleat. The pleating is not very physical because there are no repulsive forces between lattice vertices in the simple model. This transition, however, shows the unstablility generally exists in 2d system. The unphysical phenomenon originates from the topological constraint, i.e., the neighbor being fixed. To release this restriction, we use Lennard-Jones potential which is in principle a long range interaction. The fast decrease of interaction strength with distance allows the cutoff in computer simulation. We first study the mismatch problem

of a binary system. It is found that the system becomes unstable around 18% mismatch. It is possible that our simulation study is related to this phenomenon on a very basic level. The instability of 2d binary is characterized by a constant drop of the shear modulus and the appearance of topological defects, see Fig.7.5 and Fig.7.6. The appearance of topological defects with the softening of shear modulus is similar to the well known KTHNY phase transition; but the driving parameter here is not temperature but the size difference. So we call this instability "2d length-mismatch-driven melting". Using Molecular Dynamics simulation on binary system, it is possible to get a complete phase diagram with two axis as temperature and length mismatch. We hope that in the near future we can define this problem clearly and carry out a survey of this interesting phenomenon.

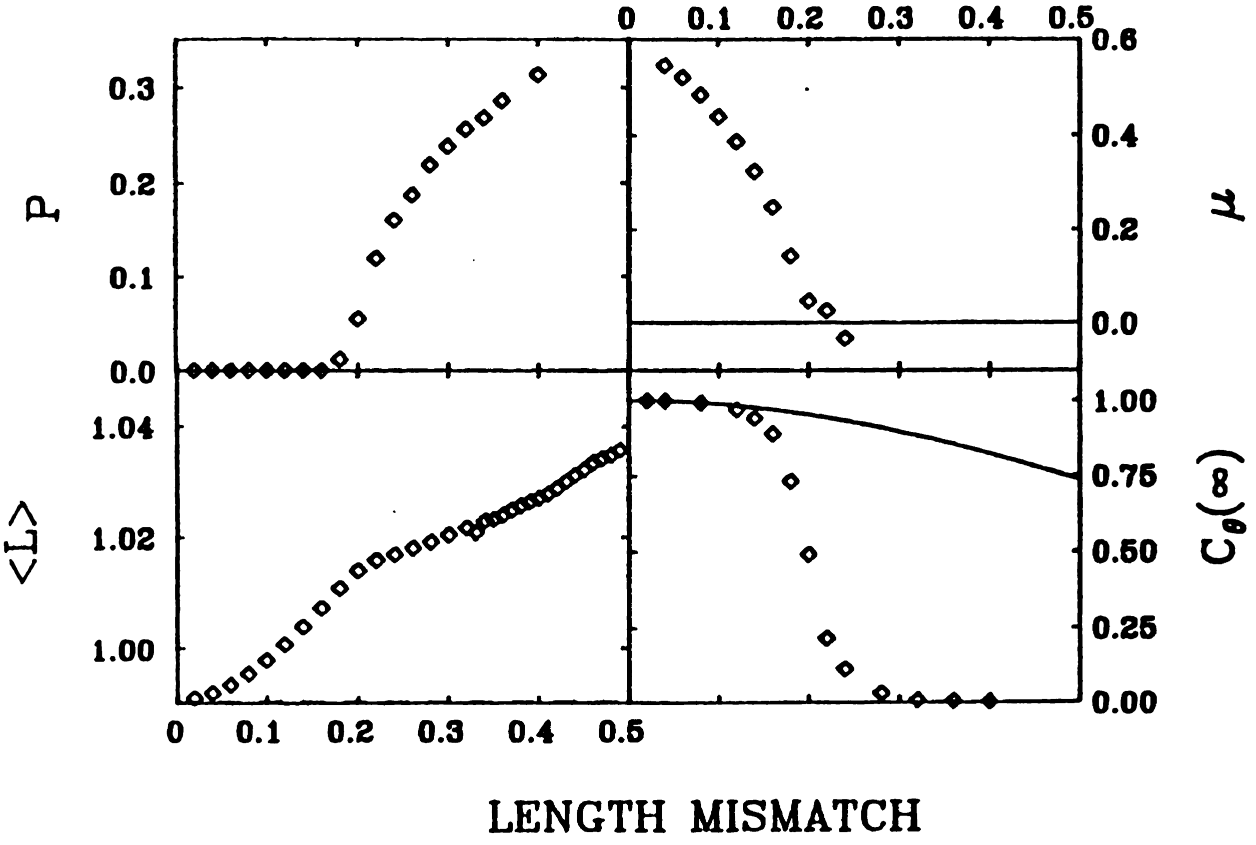

Figure 7.5: The x-axis of all four panels is length mismatch. right top panel shows the percentage of defect points. Defect points have non-six NN. Right low panel is the macroscopic size of the sample after relaxation. Left top panel is the shear modulus of the sample and lower panel the angular correlation function. The solid line in the left lower panel is from theory. We see that the simulation result drops below theory prediction when topological defect is about to present. All four diagram suggest the singularity point which characterize the instability to be about 18%.

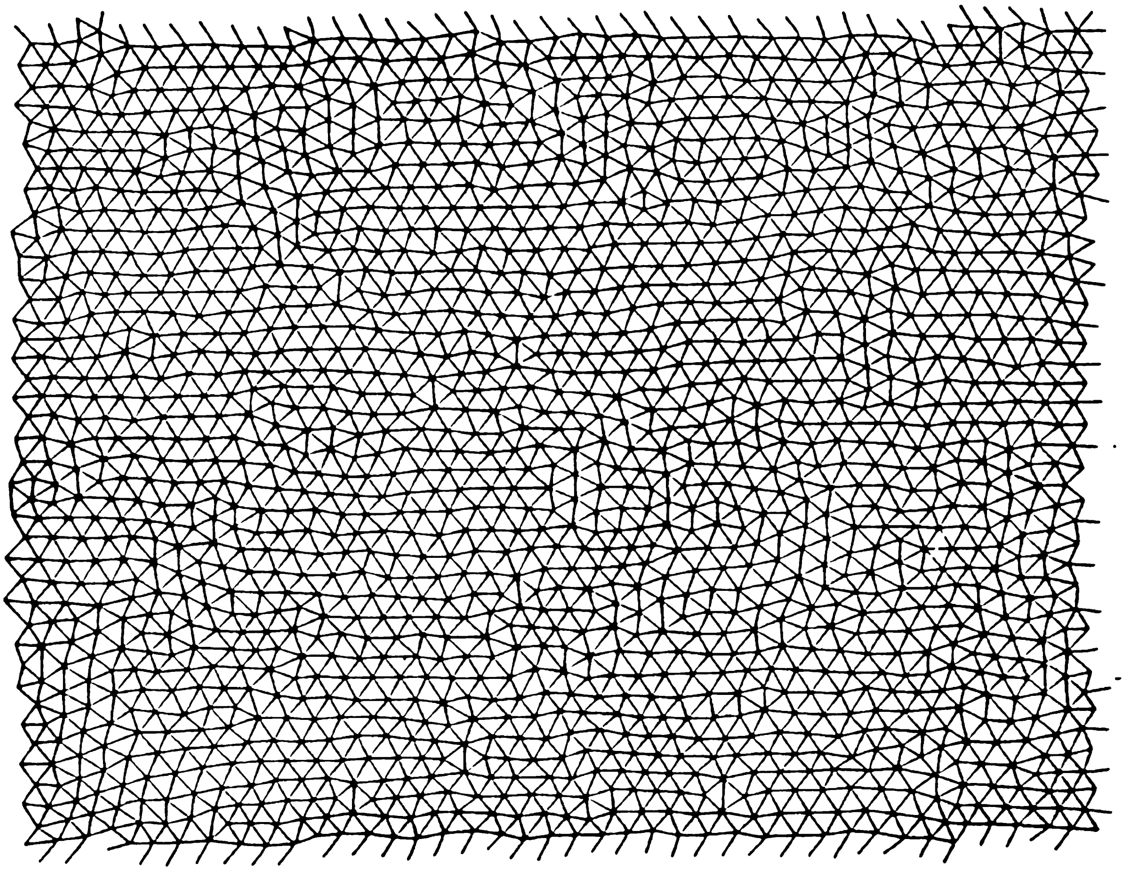

Figure 7.6: The 22% size mismatch diagram. The nearest neighbor connection follow the Voronoi algorithm. The Topological defects are points having more or less than six neighbors. Quadrupoles and dipoles(dislocation) are seen frequently. As mismatch increases, the defects begin to connect and percolate.

Bibliography

[1] Y. Cai and M. F. Thorpe, to be sent to Phys. Rev. B.

[2] S. De Gironcoli, P. Giannozzi and S. Baroni, Phys. Rev. Lett. **66** 2116(1991)

[3] J. B. Mikkelson and J. B. Boyce, Phys. Rev. Lett. **49**, 1412(1982)

[4] H. He and M. F. Thorpe, Phys. Rev.Lett. **54** 355(1983)

[5] N. Mousseau and M. F. Thorpe, submitted to PRB.

[6] J. P. Dismukes, L. Ekstrom and R. J. Paff, J. of Phys. Chem. **68**,3021(1964).

Appendix A

The Equation of Motion

The equation of motion techniqueis a variant of conventional molecular dynamicsthat is useful in disordered harmonic systems. The initial conditions at $t = 0$ are determined by the particular response function it is desired to calculate, and the equations are integrated forward in time with appropriate weighting factors. The equations of motion for any harmonic potential V are given by

$$M_i u_{i\alpha}(t) = -\sum_{j,\beta} V_{ij}^{\alpha\beta} u_{j\beta}(t), \tag{A.1}$$

where $u_{i\alpha}$ is the displacement of the ith atom in the α direction. It is convenient to think of the $u_{i\alpha}$ as classical displacements. The motion in this system can be written as a superposition of normal mode vibrations. Thus,

$$u_{i\alpha} = (1/M_i)^{1/2} \sum_n q_n \xi_n(i,\alpha) \cos(\omega_n t + \delta_n) \tag{A.2}$$

where ω_n is the frequency of the nth normal mode and δ_n is the phase shift that is determined by the initial conditions at $t = 0$. The quantity q_n is the amplitude of the nth normal mode and $\xi_n(i,\alpha)$ is the polarization eigenvector which gives the magnitude of the nth eigenvector on particle i in the α direction. These obey the usual orthogonality relations

$$\sum_{i,\alpha} = \xi_n(i,\alpha)\xi_m(i,\alpha) = \delta_{mn} \tag{A.3}$$

and

$$\sum_n = \xi_n(i,\alpha)\xi_n(j,\beta) = \delta_{ij}\delta_{\alpha\beta}, \tag{A.4}$$

with the eigenvectors chosen to be real because the dynamical matrix is real and symmetric.

In previous work, the initial conditions have corresponded to "plucking" in which the initial velocities are set equal to zero, but the displacements are finite. Here we use the same notation(see **Chapter 2** and references there) to descibe the "kick start".

The initial conditions for a "kick start", where an impulse produces an initial velocity but no displacement, are given by putting $\delta_n = -\pi/2$ in Eq. (A.2):

$$u_{i\alpha}(t) = (1/M_i)^{1/2}\sum_n q_n\xi_n(i,\alpha)\sin(\omega_n t), \tag{A.5}$$

so that the velocities are given by

$$\dot{u}_{i\alpha}(t) = (1/M_i)^{1/2}\sum_n \omega_n q_n\xi_n(i,\alpha)\cos(\omega_n t), \tag{A.6}$$

and the initial velocities are

$$\dot{u}_{i\alpha}(0) = (1/M_i)^{1/2}\sum_n \omega_n q_n\xi_n(i,\alpha), \tag{A.7}$$

which can be inverted using the orthogonality relation (A.3) to give

$$\omega_n q_n = \sum_{j,\beta} M_i^{1/2}\dot{u}_{j,\beta}(0)\xi_n(j,\beta) \tag{A.8}$$

We now compute

$$G(\omega) = \frac{2}{\pi}\int_0^T dt\sin(\omega t)e^{-3(t/T)^2}\sum_{i\alpha} u_{i\alpha}(t). \tag{A.9}$$

We see that

$$\sum_{i,\alpha} A_{i\alpha}u_{i\alpha}(t) = \sum_{i,\alpha}\sum_{j,\beta}\sum_n (M_j/M_i)^{1/2}\xi_n(i,\alpha)\xi_n(j,\beta)A_{i\alpha}\dot{u}_{j\beta}(0)\sin(\omega_n t)/\omega_n, \tag{A.10}$$

and hence

$$G(\omega) = \sum_{i,\alpha} \sum_{j,\beta} \sum_{n} (M_j/M_i)^{1/2} \xi_n(i,\alpha) \xi_n(j,\beta) A_{i\alpha} \dot{u}_{j\beta}(0) [\Delta(\omega - \omega_n) - \Delta(\omega + \omega_n)]/\omega_n, \tag{A.11}$$

and choosing

$$u_{i\alpha}(0) = A_{i\alpha} = \sqrt{2} \cos \theta_{i\alpha}, \tag{A.12}$$

where $\theta_{i\alpha}$ is a random angle uniformly distributed in the interval $0 < \theta_{i\alpha} < 2\pi$. We have

$$\begin{aligned} \langle G(\omega) \rangle &= \sum_{i,\alpha} \sum_{n} \xi_n(i,\alpha) [\Delta(\omega - \omega_n) - \Delta(\omega + \omega_n)]/\omega_n, \\ &= [\Delta(\omega - \omega_n) - \Delta(\omega + \omega_n)]/\omega, \end{aligned} \tag{A.13}$$

which is the density of states divided by the frequency $\rho(\omega)/\omega$. Note that this form leads to an odd function of the frequency because of the sine transform.

$$\rho(\omega)/\omega = \frac{2}{\pi} \int_0^T dt \sin(\omega t) e^{-3(t/T)^2} \sum_{i,\alpha} A_{i\alpha} u_{i\alpha}(t). \tag{A.14}$$

This form artificially forces the density of states to zero as the frequency goes to zero. By happy chance $\rho(\omega)$ in Eq. (A.14) goes as ω^2 at low frequencies, which is the correct form in three dimensions. Thus the form imposed by the numerical method leads to the correct form and will aid convergence somewhat. If we integrate both sides of Eq. (A.14) over frequency and integrate the right hand side by parts, we find the first inverse moment

$$\int_0^{\omega_{max}} d\omega \rho(\omega)/\omega = \langle 1/\omega \rangle = \frac{2}{\pi} \int_0^T dt e^{-3(t/T)^2} \sum_{i,\alpha} A_{i\alpha} u_{i\alpha}(t)/t. \tag{A.15}$$

Because of the "kick start", the displacements $u_{i\alpha}(t)$. t at small times so that the integral (A.15) converges at small times. It also converges at large times because the $|u_{i\alpha}(t)|$ are bounded and so the $1/t$ factor ensures that the integrand decreases.

Appendix B

Distribution Function of Multilayer System

In this appendix, we show how the first few moments can be extracted from the distribution function for the random case when $k_A = k_B$. Recalling Eqs. (3.68) and (3.71), we can write down a generating function for the moments,

$$\sum_n c_n^* q^n = e^{-i(1-2x)qA_{\mathrm{ii}}} \prod_{\mathrm{j}\neq\mathrm{i}} (\cos qA_{\mathrm{ij}} - i(1-2x)\sin qA_{\mathrm{ij}}) \tag{B.1}$$

Taking the logarithms and expanding up to fourth order, the left hand side gives

$$\begin{aligned}
\ln(1 \quad + & \quad c_1^* q + c_2^2 q^2 + c_3^* q^3 + c_4^* q^4 + ...) \\
= & \quad q[c_1^*] \\
& +q^2[c_2^* - \frac{1}{2}c_1^{*2}] \\
& +q^3[c_3^* - c_1^* c_2^* + \frac{1}{3}c_1^{*3}] \\
& +q^4[c_4^* - \frac{1}{2}c_2^{*2} - c_1^* c_3^* + c_1^{*2} c_2^* - \frac{1}{4}c_1^{*4}] \,.
\end{aligned} \tag{B.2}$$

From the right hand side of Eq. (B.1), we have

$$
\begin{aligned}
\ln[\ e^{-i(1-2x)qA_{ii}} & \prod_{j\neq i}(\cos qA_{ij} - i(1-2x)\sin qA_{ij})] \\
= \ & q^2[-2x(1-x)\sum_{j\neq i} A_{ij}^2] \\
& -q^3[i\frac{4}{3}x(1-x)(1-2x)\sum_{j\neq i} A_{ij}^3] \\
& +q^4[\frac{2}{3}x(1-x)(1-6x+6x^2)\sum_{j\neq i} A_{ij}^4]\,. \qquad \text{(B.3)}
\end{aligned}
$$

We confirm that $c_1^* = 0$ and also find that

$$
\begin{aligned}
c_2^* = & \quad -2x(1-x)\sum_{j\neq i} A_{ij}^2 \\
c_3^* = & \quad -i\frac{4}{3}x(1-x)(1-2x)\sum_{j\neq i} A_{ij}^3 \\
c_4^* = & \quad \frac{2}{3}x(1-x)(1-6x+6x^2)\sum_{j\neq i} A_{ij}^2 + \frac{1}{2}c_2^{*2}\,. \qquad \text{(B.4)}
\end{aligned}
$$

Combining with Eqs. (3.24), (3.25) and (3.72) we have

$$
\begin{aligned}
M_2 = & \quad \frac{2!c_2^*}{(-i)^2} \\
= & \quad 4x(1-x)(\sum_{j} A_{ij}^2 - A_{ii}) \\
= & \quad x(1-x)\left[W_1(k) - W(k)^2\right]\ , \qquad \text{(B.5)}
\end{aligned}
$$

which agrees with the result obtained previously in Eq. (3.23) for the fluctuation in random case.

We also obtain results for the higher moments,

$$
M_3 = \quad \frac{3!c_3^*}{(-i)^3}
$$

$$= \quad 8x(1-x)(2x-1)\sum_{\mathbf{j}\neq\mathbf{i}} A_{\mathbf{ij}}^{3} , \tag{B.6}$$

and

$$M_4 - 3M_2^2 = x(1-x)[1-6x(1-x)]\sum_{\mathbf{j}\neq\mathbf{i}} A_{ij}^{4} \tag{B.7}$$

Appendix C

Symmetric Distribution Case

It is apparent from **Appendix B** that all the odd moments have the general form (for $n \geq 1$):

$$M_{2n+1} = \sum_{l=1}^{n} f_{ln}(x) \sum_{\mathbf{j}\neq \mathbf{i}} A_{\mathbf{ij}}^{2l+1} \, . \tag{C.1}$$

When $k_A = k_B = k$, from Eqs. (3.28) and (3.61) and denoting k_T/k as α, for the $2d$ square net only, we can rewrite $A_{\mathbf{ij}}$ as

$$A_{\mathbf{ij}}(\alpha) = -\frac{1}{2N} \sum_{\mathbf{q}} \frac{[1-\cos(\mathbf{q}\cdot\nu)]e^{i\mathbf{q}\cdot\mathbf{r}_{\mathbf{ij}}}}{[1-\cos(\mathbf{q}\cdot\nu)] + \alpha[1-\cos(\mathbf{q}\cdot\delta)]} \, . \tag{C.2}$$

Noticing that the $x(\delta)$ and $z(\nu)$ directions of $\mathbf{q}$ are all summed over, we can switch δ to ν and vice versa without changing the integration. Then we have

$$A_{\mathbf{ij}}(\frac{1}{\alpha}) = -\frac{1}{2N} \sum_{\mathbf{q}} \frac{\alpha[1-\cos(\mathbf{q}\cdot\delta)]e^{i\mathbf{q}\cdot\mathbf{r}_{\mathbf{ij}}}}{[1-\cos(\mathbf{q}\cdot\nu)] + \alpha[1-\cos(\mathbf{q}\cdot\delta)]} \tag{C.3}$$

From above two equations and Eqs. (3.24) and (3.61) we have

$$W(\alpha) + W(\frac{1}{\alpha}) = 1 \tag{C.4}$$

Now making use of the fact that

$$\delta(\mathbf{q}) = \frac{1}{N} \sum_{\mathbf{i}} e^{i\mathbf{q}\cdot\mathbf{r}_{\mathbf{i}}} \tag{C.5}$$

and using Eq. (C.2) , we obtain the following expression for $n > 2$:

$$\sum_{\mathbf{j}} A^n_{\mathbf{ij}}(\alpha) = (-\frac{1}{2})^n \frac{1}{N^{n-1}} \sum_{\mathbf{q}'\mathbf{q}''\cdots\mathbf{q}^{(n)}} \frac{[1-\cos(\mathbf{q}'\cdot\nu)]}{[1-\cos(\mathbf{q}'\cdot\nu)]+\alpha[1-\cos(\mathbf{q}'\cdot\delta)]}\cdots$$

$$\frac{[1-\cos(\mathbf{q}''\cdot\nu)]}{[1-\cos(\mathbf{q}''\cdot\nu)]+\alpha[1-\cos(\mathbf{q}''\cdot\delta)]}\cdots$$

$$\frac{[1-\cos(\mathbf{q}^{(n)}\cdot\nu)]}{[1-\cos(\mathbf{q}^{(n)}\cdot\nu)]+\alpha[1-\cos(\mathbf{q}^{(n)}\cdot\delta)]}$$

$$\delta(\mathbf{q}'+\mathbf{q}''+\cdots+\mathbf{q}^{(\mathbf{n})})\,. \tag{C.6}$$

We make the replacement:

$$\frac{[1-\cos(\mathbf{q}^{(l)}\cdot\nu)]}{[1-\cos(\mathbf{q}^{(l)}\cdot\nu)]+\alpha[1-\cos(\mathbf{q}^{(l)}\cdot\delta)]} = 1 - \frac{\alpha[1-\cos(\mathbf{q}^{(l)}\cdot\delta)]}{[1-\cos(\mathbf{q}^{(l)}\cdot\nu)]+\alpha[1-\cos(\mathbf{q}^{(l)}\cdot\delta)]}\,, \tag{C.7}$$

in Eq. (C.6) and use the relation between $A_{\mathbf{ii}}$ and W, to get the following result.

$$\sum_{\mathbf{J}} A^n_{\mathbf{ij}}(\alpha) = (-1)^n \sum_{\mathbf{J}} A^n_{\mathbf{ij}}(\frac{1}{\alpha}) + (-\frac{1}{2})^n[(1-W(\frac{1}{\alpha}))^n - (-1)^n W(\frac{1}{\alpha})^n]\,. \tag{C.8}$$

From Eq. (C.4) and using $A_{\mathbf{ii}} = -\,W/2$, we have,

$$\begin{aligned}\sum_{\mathbf{J}} A^n_{\mathbf{ij}}(\alpha) \quad &= (-1)^n \sum_{\mathbf{J}} A^n_{\mathbf{ij}}(\frac{1}{\alpha}) + (-\frac{1}{2})^n[W(\alpha)^n - (-1)^n W(\frac{1}{\alpha})^n] \\ &= (-1)^n \sum_{\mathbf{J}} A^n_{\mathbf{ij}}(\frac{1}{\alpha}) + [A^n_{\mathbf{ii}}(\alpha) - (-1)^n A^n_{\mathbf{ii}}(\frac{1}{\alpha})]\,. \end{aligned} \tag{C.9}$$

When $k = k_T$, which means $\alpha = 1$, we have

$$\sum_{\mathbf{J}} A^n_{\mathbf{ij}}(1) - (-1)^n \sum_{\mathbf{J}} A^n_{\mathbf{ij}}(1) = A^n_{\mathbf{ii}}(1) - (-1)^n A^n_{\mathbf{ii}}(1)\,, \tag{C.10}$$

which leads to the conclusion that when n is odd, $\sum_{\mathbf{j}} A^n_{\mathbf{ij}} = A^n_{\mathbf{ii}}$ or $\sum_{\mathbf{j}\neq\mathbf{i}} A^n_{\mathbf{ij}}$ is identically zero. So the right hand side of Eq. (C.1) is zero when $k = k_T$, and all the odd moments of the distribution vanish for the $2d$ square net. For other lattices, this symmetry is not present.

Appendix D

Average NN-distance in Semiconductor Alloys

In this appendix we will derive $\langle d_{AC} \rangle$ as an example. The idea is the same as that in the multilayer system,(see **Chapter 3**)but the method is modified because it is site problem here instead of bond problem.

We can neglect notation C in $A-C$ and $B-C$ bonds. Because C forms a sublattice which bridges the A and B, every A and B should be connected to four C while they never connect to each other. We thus can make C as dummy variable in summations. In many cases we only write those site variables that are A or B.

Define projecting operator P_A^{iC} which is 1 if site i is A and 0 if i is B. The other projector for BC bond is P_B^{iC} and is complement of A projector. It is obvious that $\langle P_A^{iC} \rangle = 1 - x$ and $\langle P_B^{iC} \rangle = x$.

Minimization of energy in Eq.(4.10) with respect to the displacement vector $\mathbf{U}$ gives the solution.

$$\begin{aligned} \mathbf{U} &= (\mathbf{M})^{-1}\phi \\ &\equiv \mathbf{G}\phi \end{aligned} \tag{D.1}$$

Bring Eq.(D.1) into Eq.(4.2) and perform the ensemble average for AC type bonds, we have,

$$\langle h_{AC}\rangle = h_e + \frac{1}{1-x}\sum_{\langle mC'\rangle}\langle P_A^{iC}\phi_{mC'}\rangle \mathbf{G}_{i\vec{C},m\vec{C}'} \tag{D.2}$$

"$\langle\rangle$" after the summation is the ensemble average. "$\langle\rangle$" under the summation is understood to exclude double counting.

The Green's function $\mathbf{G}_{i\vec{C},m\vec{C}'}$ is a short hand for $< i\vec{C}|\mathbf{G}|m\vec{C}' >$ Note that summation over sub-indices of $\mathbf{G}_{i\vec{C},m\vec{C}'}$ is zero because of symmetry. So any constant term from the ensemble average is effectively zero in the average length expression.

Bring Eq.(4.12) into Eq.(D.2) and simplify it,

$$\langle h_{AC}\rangle = h_e + \frac{\alpha}{1-x}\sum_{mC'}\langle P_A^{iC} h^0_{mC'}\rangle \mathbf{G}_{i\vec{C},m\vec{C}'} \tag{D.3}$$

The natural length can be expressed in the projectors as:

$$h^0_{mC'} = h^0_A P_A^{mC'} + h^0_B P_B^{mC'} \tag{D.4}$$

We need to work out ensemble averages $\langle P_A^{iC} P_A^{mC'}\rangle$ and $\langle P_A^{iC} P_B^{mC'}\rangle$.

Note that C and C' all belong to C type.

$$\begin{aligned}\langle P_A^{iC} P_A^{mC'}\rangle &= (1-x)^2(1-\delta_{im}) + (1-x)\delta_{im} \\ &= (1-x)^2 + x(1-x)\delta_{im}\end{aligned} \tag{D.5}$$

The first term is effectively zero because it does not contribute to the final result of $\langle h_{AC}\rangle$ after the summation. We use a notation $\overset{eff}{=}$ to replace $=$ and discard these terms on the right side of the equations,

$$\langle P_A^{iC} P_A^{mC'}\rangle \overset{eff}{=} x(1-x)\delta_{im} \tag{D.6}$$

The same for $\langle P_A^{iC} P_B^{mC'}\rangle$,

$$\langle P_A^{iC} P_B^{mC'}\rangle \overset{eff}{=} -x(1-x)\delta_{im} \tag{D.7}$$

Bring Eq.(D.6) and (D.7) into Eq.(D.3),

$$\begin{aligned} \langle h_{AC} \rangle &= h_e + x(h_A^0 - h_B^0) \sum_{mC'} \alpha \delta_{im} \mathbf{G}_{i\vec{C},m\vec{C}'} \\ &\equiv h_e + x(h_A^0 - h_B^0) a^{**} \end{aligned} \tag{D.8}$$

Note that $h_e = \langle h_{ij} \rangle = (1-x)h_A^0 + xh_B^0$, Eq.(D.8) gives $\langle d_{AC} \rangle$ in Eq.(4.15).And the Waston integral is related to Green's function in following way,

$$a^{**} = \sum_{C'} \alpha \mathbf{G}_{i\vec{C},i\vec{C}'} \tag{D.9}$$

When apply this method to quaternary system or pure bond mismatch system, a^* shows up and has the expression:

$$a^* = \alpha \mathbf{G}_{i\vec{C},i\vec{C}} \tag{D.10}$$

Same method applies for energy calculation and the introduction of projectors simplify the mathematics.

MICHIGAN STATE UNIV. LIBRARIES
31293009081914